Diplomarbeit

n-Type Rear Junction Solar Cells with Locally Contacted Al-Alloyed Emitter

verfasst von
Johannes Nils Raabe

Universität Konstanz

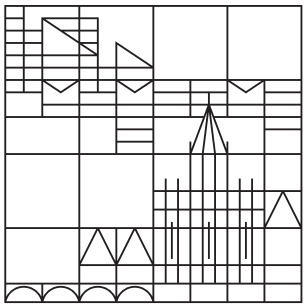

vorgelegt an der
Universität Konstanz
Mathematisch-Naturwissenschaftliche Sektion
Fachbereich Physik

Erstgutachter: Prof. Dr. Giso Hahn
Zweitgutachter: Prof. Dr. Thomas Dekorsy

Konstanz, Juli 2012

Contents

Zusammenfassung

Ziel dieser Diplomarbeit war die Verbesserung der Rückseite der PhosTop Solarzelle. Um dies zu erreichen, wurde die vollflächige Metallisierung durch eine Passivierungsschicht ersetzt, welche aus einer oder mehreren dielektrischen Schichten besteht. Eine dielektrische Schicht auf der Rückseite hat zweierlei Vorteile. Zum einen kann sie zu einer Erhöhung der offenen Klemmspannung, aber auch zu einer Verbesserung des Kurzschlussstroms (nicht bei Solarzellen mit Emittern auf der Rückseite) aufgrund verbesserter Passivierung der Siliziumoberfläche führen. Zum anderen ermöglicht das Aufbringen von dielektrischen Schichten auf der Rückseite die interne Reflexion zu verbessern, was wiederum zu einem Kurzschlussstromgewinn führen kann.

In dieser Arbeit sind zwei unterschiedliche Solarzellenkonzepte realisiert worden. Beide Konzepte sind mit der Vorderseite der PhosTop Solarzelle versehen, welche ein selektives Front Surface Field sowie eine dielektrische Passivierung bestehend aus einem Siliziumdioxid/Siliziumnitrid Stapel aufweist. Das Al-LARE Solarzellenkonzept hat auf der Rückseite einen lokal legierten Emitter, der sich nach vollflächiger Passivierung und lokaler Öffnung durch vollflächigen Druck einer Paste und nachfolgendem Feuern bildet. Zum anderen wurde das FALCON Solarzellenkonzept realisiert, welches aus einem vollflächigen, zurückgeätzten Emitter besteht, der passiviert und lokal kontaktiert wird.

Zunächst wurden die Passivierungseigenschaften unterschiedlicher Schichten und Stacksysteme auf negativ sowie stark positiv dotiertem Silizium untersucht. Dabei wurde im ersteren Fall festgestellt, dass die Passivierung mit Al_2O_3/SiNA-SiN_x, SiNA-SiN_x und CT-SiN_x die besten Resultate liefert. Es wurden zwei unterschiedliche Methoden zur Abscheidung einer Siliziumnitridschicht genutzt, deren Schichten in dieser Arbeit durch SiNA-SiN_x (remote PECVD) und CT-SiN_x (direct PECVD) bezeichnet werden. Im zweiten Fall, der Passivierung von hochdotierten Emittern, wurde keine Verbesserung gegenüber der Feldeffektpassivierung durch den Emitter selbst gefunden. Eine Erniedrigung der effektiven Oberflächen - Rekombinationsgeschwindigkeit und eine damit einhergehende verbesserte Passivierung wurde nur für einen sehr dünnen Emitter erreicht, bei dem der Feldeffekt schon sehr schwach war. Entscheidend aber ist, das die effektive Passivierung eines hochdotierten Emitters mittels dielektrischer Schichten im Vergleich zu einer unpassivierten, nicht zurückgeätzen Referenz nicht verbessert wurde.

Aufbauend auf den Resultaten aus diesen beiden vorbereitenden Experimenten wurden großflächige Al-LARE und FALCON Solarzellen hergestellt, welche jeweils mit parallel prozessierten PhosTop Solarzellen verglichen wurden.
Um die optimalen Abstände und Breiten für die Rückseitengeometrie von Al-LARE Solarzellen zu bestimmen, wurde zunächst eine Emitterbreiten- sowie Abstandsvariation auf kleinen 5×5 cm^2 Solarzellen durchgeführt. Diese zeigte für eine Emitterbreite von mindestens 100 µm und einen Emitterabstand von 300 µm die höchsten Kurzschlussströme. Das experimentelle Ergebnis konnte durch zwei-dimensionale Simulationen bestätigt werden. In beiden Fällen wurde durch die erhöhte interne Reflexion ein Kurzschlussstromgewinn von etwa 0.5 mA/cm^2 erreicht. Die beste 15.6×15.6 cm^2 Al-LARE Solarzelle erreichte einen maximalen Wirkungsgrad von 17 % mit einer Rückseitenpassivierung bestehend aus SiO_2/SiNA-SiN_x. Die Hauptgründe für eine Verschlechterung des Wirkungsgrades gegenüber der PhosTop Solarzelle waren zum einen

ein sehr großer Wert für j_{02}, zum anderen eine leicht verschlechterte effektive Oberflächenrekombinationsgeschwindigkeit. Zusammen mit einem leicht erhöhten Serienwiderstand kam es zu einer Verschlechterung des Wirkungsgrades aufgrund einer starken Reduktion des Füllfaktors und der offenen Klemmspannung.
Für das FALCON Solarzellenkonzept wurden bessere Ergebnisse erzielt. FALCON Solarzellen, welche auf der Rückseite mit SiO_2/SiNA-SiN_x passiviert waren, erreichten einen Wirkungsgrad von 18.9 %, wobei ein Kurzschlussstromgewinn im Vergleich zur sehr guten PhosTop Referenz von 0.5 mA/cm^2 erreicht wurde. Auch bei diesem Zellkonzept waren wesentliche Limitierungen des Wirkungsgrades durch einen erhöhten Wert für j_{02}, einen erhöhten Serienwiderstand und eine nicht verbesserte Rückseitenpassivierung (effektiv gegenüber vollflächiger Metallisierung) verursacht. Durch die ersten beiden Anteile wurde der FF um mindestens 2 % reduziert, wobei die gegenüber der PhosTop Solarzelle nicht verbesserte Rückseitenpassivierung für keine Steigerung der offenen Klemmspannung verantwortlich ist. Eine Steigerung der offenen Klemmspannung ist, wie eine durchgeführte Simulation zeigte, nur für niedrigere Oberflächenrekombinationsgeschwindigkeiten möglich.

1. Introduction

Climate change due to anthropogenic global warming causes increased changes in environment, biodiversity and foreign relations. Furthermore, tensions between cultures or countries may arise due to a shortage of everyday goods such as clean water and food supply e.g. as a result of extreme weather, which can strongly increase the conflict potential.
Anthropogenic global warming is mainly caused by the combustion of fossil fuels, which results in the release of greenhouse gases [1]. Besides harming the environment, these fossil fuels are limited, which can furthermore increase the conflict potential. Therefore, not only for environmental, but also for economical and social reasons, is the implementation of a free, non-toxic and unrestricted energy source into the daily energy consumption one approach to reduce the impact of climate change and is therefore a necessity. One option for providing this clean energy is the unconditionally supplied energy from the sun, which can be converted to electricity by using solar cells.

Today, silicon is the main semiconductor material, from which commercially available solar cells are fabricated. Crystalline silicon (c-Si) based solar cells have a market share of approx. 80 %, while the remaining part is taken by a large amount of different solar cell technologies (mainly thin films). In 2011, roughly 40 % of fabricated c-Si based solar cells were made out of mono-crystalline boron-doped silicon, while 60 % are consisting of a multi-crystalline p-type silicon base [2].
Approximately 29.7 GW of installed grid-connected capacity was added worldwide in 2011, which is equal to about 40 % of the world's total grid-connected photovoltaic installed capacity [3]. This indicates a strong increase in the last year, which was a result of reduced fabrication costs of solar cells, a strongly competitive market situation and improved government support.

Improving the efficiency is crucial for a further reduction in cost per watt peak and increase in installed capacity. While most commercially available solar cells still feature a boron doped silicon bulk, one approach to improve efficiency is to change the base to n-type silicon. Negatively doped silicon exhibits several advantages compared to boron doped silicon. The latter shows light-inducded degradation due to the formation of boron-oxygen complexes under illumination [4, 5, 6] and furthermore increased sensitivity to metal contaminations [7]. Both performance-limiting effects can be reduced by using n-type base material. Switching therefore, from the predominating p-type base material to n-type is one further step to higher efficiencies and thereby lower the cost per watt peak. In the upcoming years, the share of mono-crystalline silicon n-type based solar cells compared to p-type is expected to rise from today 10 % up to 65 % in 2020 [2].

The easiest approach to increase the n-type silicon share is to use the already well known industrial process for p-type silicon solar cells and adapt it to n-type solar cells. The starting structure and reference of this work, the improved PhosTop solar cells is one such example, which is fabricated in a similar way as the selective emitter solar cell based on p-type silicon [8]. The improved PhosTop solar cell features a n-type bulk, a selective front surface field and a SiO_2/SiN_x front side passivation. On the rear, the emitter is alloyed by full area screen-printing

and subsequent co-firing. The improved PhosTop solar cell has reached an efficiency of 19.4 % [9].

The main objective of this work is to reduce recombination losses due to the full area alloyed and unpassivated rear side of the improved PhosTop solar cell by means of a reduced emitter area and a dielectric passivation. This can reduce the rear side saturation current density and hence lead to an increased open-circuit voltage. Furthermore, since dielectric passivation of the rear can reduce parasitic absorption in the aluminium paste and eutectic of the solar cell, the passivation allows to effectively mirroring the internal light back into the cell. This increases the short-circuit current density, since more light can be absorbed within the silicon due to an extended light path.

Basically, this work can be divided into four parts. First, the basics and relevant background knowledge of solar cells is mediated, while a special focus is laid on the surface passivation.
This is followed by a short introduction into the most important characterization methods that are applied.
Three different solar cell concepts, the improved PhosTop solar cell as well as the Aluminium-Locally Alloyed Rear Emitter (Al-LARE) and Full Area Locally CONtacted (FALCON) solar cell are discussed in detail. Their limitations and capabilities are analysed by using two-dimensional simulations. The Al-LARE solar cell concept features a passivated n-type bulk, which has a locally alloyed emitter on the rear side. In contrast, the FALCON solar cell has a full area rear aluminium emitter, that is passivated and locally contacted.
Finally, realized experiments are presented and discussed. At the beginning, preparatory experiments are shown, in which the passivation quality of diverse passivation layers and stacks on differently doped silicon surfaces is analysed. Starting from these preparatory experiments, large area Al-LARE and FALCON solar cell results are presented that are analysed in detail and compared to the improved PhosTop solar cells as a reference.

2. The Silicon Solar Cell

Solar cells are large-area photo-diodes that generate electricity from solar radiation. As for all energy converting systems, the conversion efficiency η is the key parameter. Since the conversion efficiency depends indirectly on the effective lifetime of minority charge carriers, all limiting effects, such as recombination must be minimized.

First of all, the functional principle of a commercially available p-type silicon solar cells is explained. Besides functionality and key issues, such as the one-diode model and saturation current, essential parameters of a silicon solar cell are discussed. Furthermore, a more realistic model of a solar cell is presented in order to extract important characteristics such as series resistance, shunt resistance and the diode saturation current densities by means of fitting measured IV curves using the two-diode model.

An overview of recombination losses in the bulk, such as radiative recombination, Auger recombination and Shockley-Read-Hall recombination and the important surface recombination is given. This is followed by a discussion of the electrical and optical losses of a solar cell with an emphasis on topics relevant to this work.

The ideas behind surface passivation and specific methods used within this work are presented. Options for passivation, such as silicon nitride, silicon oxide, aluminium oxide and their combinations, referred to as stack systems, are explained in more detail.

Finally, the formation of the aluminium alloyed emitter in n-type solar cells is explained.

2.1. Functional Principle

Commercially available silicon solar cells, as shown in figure 2.1, usually consist of a p-type bulk doped by boron, and a front side n-type phosphorous emitter, which is formed by diffusion. A screen-printed silver grid on the front side provides contact to the emitter, whereas on the rear side, full area screen-printing and co-firing of an aluminium paste leads to a back-surface field (BSF) as well as a contact to the bulk.

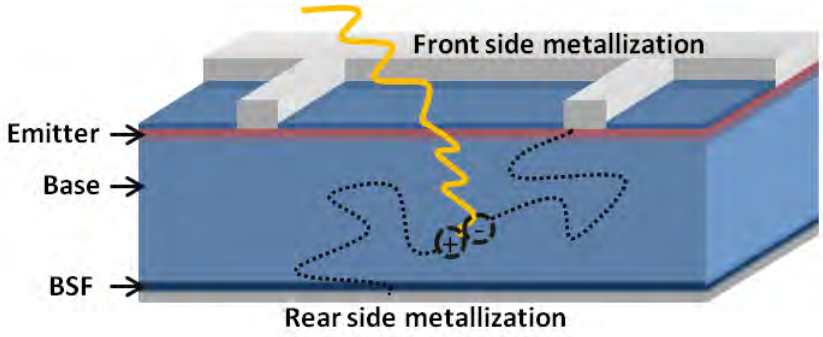

Figure 2.1.: Structure of a standard p-type solar cell

A solar cell generates power from photons with an energy above the band gap energy, therefore above $E_{gap} = 1.12\,\text{eV}$ in the case of silicon. Electrons get excited from the absorbed energy, jumping from the valence- to the conduction band while leaving a hole in the valence band. Both diffuse separately through the semiconductor and once the electron gets close to the pn-junction, forced by the built-in electric field, they become spatially separated. All energy above the gap energy E_{gap} will be lost in the form of heat energy due to collisions of the carriers with the lattice, creating phonons within less than a few picoseconds.

After the carriers are spatially separated by the built-in electric field, each of them is in the region, where they are majority carriers and have a much lower recombination probability. Thus, minority charge carrier diffusion length is one of the most important properties of a solar cell, since it determines whether the generated minority charge carriers can reach the junction and hence are contributing to the total power of the cell, or, if they recombine before. The minority charge carrier lifetime τ can be associated with a minority charge carrier diffusion length $l = \sqrt{D\tau}$, where D represents the diffusivity. For example, within the base of a p-type solar cell, the electrons are minority charge carriers, which need to diffuse through the base to the junction into the n-type doped emitter. If the diffusion length is too short, electrons recombine before they reach the pn-junction and are lost. While the minority charge carrier diffuses through the solar cell, different recombination mechanisms are reducing the effective lifetime of the carrier. These recombination mechanisms are presented in section 2.3.

The above mentioned back-surface field is a high-low junction, since it is higher positively doped than the base. It shields the minority carriers, in this case the electrons, from the rear surface by a built-in electric field. This reduces the effective rear surface recombination velocity, which is a measure for the recombination at the surface as a result of the discontinuity of the crystal lattice of the semiconductor. More details on the losses and properties of semiconductor surfaces are given in 2.3.2 and 2.5.

The absorption of light within silicon is crucial for the design of solar cells. A strong wavelength

dependence of the absorption coefficient α results in a spatially different photogeneration. The remaining intensity I of light follows $I(x) = I_T(0)\, e^{-\alpha x}$, where x is the penetration depth, and I_T the transmission intensity from the first in-coupled light. This results in a wavelength dependence of the remaining intensity. While high energy photons such as blue light (wavelengths of 400 nm to 500 nm) are mostly absorbed within the first microns of the solar cell, long wavelengths in the near infrared (wavelength of above 800 nm) are in need of a couple of hundred microns of semiconductor material to be totally absorbed. Absorption, or photogeneration of carriers therefore dominates at the front surface of the solar cell. That is the reason why most solar cells have their junction at the front side, because this allows enough carriers to be separated by the pn-junction, especially for low material quality.

The reason for such a low probability of near infrared light to be absorbed, is that silicon is an indirect semiconductor, which is in need of one or several phonons for giving an additional momentum to the excited electrons, while they are jumping from valence- to conduction band. Because the lowest possible energy transition between valence and conduction band is not in the same crystal direction, extra phonons are required to provide the necessary momentum.

2.2. Properties of Solar Cells

The most important property of a solar cell is its conversion efficiency, which is defined as the ratio of the output in terms of electrical power $P_{electrical,out}$, and the incident power $P_{light,in}$ as light power. The properties of the light source are important to mention, since it is crucial to determine the efficiency of the solar cell. The sun has almost a perfect black body spectrum, as it is shown in figure 2.2.

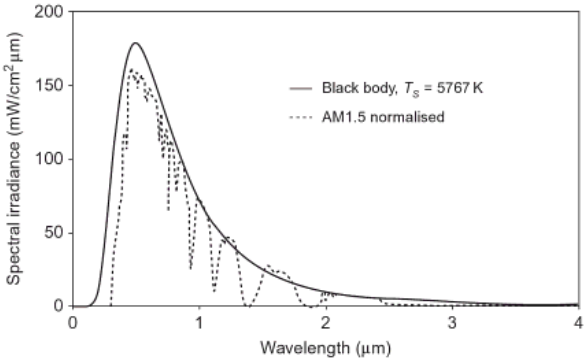

Figure 2.2.: Blackbody spectrum of the sun and the respective AM1.5 spectrum from [10]

Here on earth, absorption within the atmosphere needs to be taken into consideration. In figure 2.2 the so called AM 1.5G spectrum is shown. It considers this parasitic absorption in the air for sun light on sea level under an incident angle of 48.2 degrees. This is a typical value for Germany's latitude. The absorption leads to a reduced and interrupted spectrum. Moreover, the sun is indeed not a perfect black body at 5767 Kelvin.
Since only photons with energy higher than the bandgap energy can be absorbed, additional losses are present and are limiting the silicon solar cell's maximum possible conversion efficiency. Furthermore, excess energy of the incident photons is lost due to lattice collisions. Moreover, free carrier absorption (FCA) can lead to parasitic losses especially for long wavelengths. Summarizing, besides intrinsic losses such as e.g. the omnipresent Auger and radiative recombination, this leads to a theoretically maximum achievable conversion efficiency for single-junction silicon solar cells under isotropic response (under all incident angles) of 28.8 % according to Green [11].

The AM 1.5G spectrum is modelled in a sun simulator to characterize the solar cell, which results in an IV curve, similar to the one shown in figure 2.3. This characterization method is explained in detail in 3.1.

The conversion efficiency η is determined by the maximum power output. It can be identified by measuring the IV-curve, which represents the behaviour of the solar cell under applied voltage and leads to the maximum power point MPP. A standard solar cell IV-curve is shown in figure 2.3.

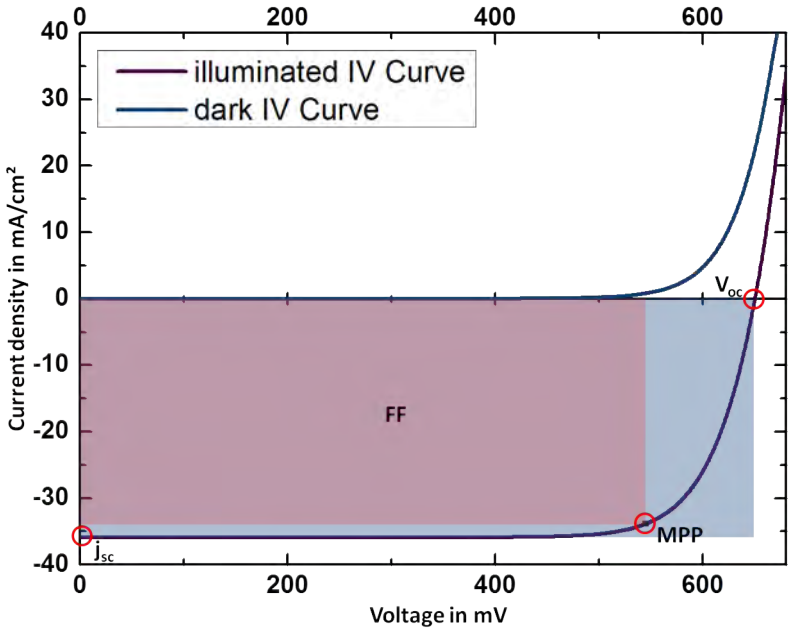

Figure 2.3.: Standard solar cell dark and illuminated IV-curve, fabricated within this work with highlighted points for the illuminated curve

Highlighted are the short-circuit current density j_{sc}, the previously mentioned MPP, the open-circuit voltage V_{oc} and the Fill Factor FF. The FF is given as the ratio of $j_{MPP} \cdot V_{MPP}$ to the the product of $j_{sc} \cdot V_{oc}$. Furthermore, the conversion efficiency η can be expressed using the mentioned characteristics of a typical diode:

$$\eta = \frac{P_{electrical,out}}{P_{light,in}} = \frac{FF\, j_{sc}\, V_{oc}}{P_{light,in}} \tag{2.1}$$

Further characteristics of the solar cell are given by the IV-curve.

Short-circuit current density The short-circuit current density $j_{sc} = \frac{I_{sc}}{A}$ with A the area of the solar cell, gives the maximum current output of the solar cell and equals ideally the illumination current j_L. It is measured without any applied voltage under illumination.

Open-circuit voltage The open-circuit voltage gives the maximum potential difference between both contacts. By reorganizing the one diode equation 2.7 and using $I(V_{oc}) = 0$ follows

$$V_{oc} = \frac{n_1 kT}{q}\, ln\left(\frac{I_L}{I_0} + 1\right) \tag{2.2}$$

where n_1 equals the first diode's ideality factor and kT/q the thermal voltage. It can be seen that it depends on the ratio of the light-generated current I_L and the saturation current I_0 and therefore is strongly influenced via I_0 and I_L by the passivation and junction quality. This will be discussed later in more detail.

Fill factor The fill factor describes the ratio of maximum power output to the product of j_{sc} and V_{oc}.

$$FF = \frac{j_{mpp} V_{mpp}}{j_{sc} V_{oc}} \tag{2.3}$$

A good cell has a fill factor of around 80 %, which is mainly due to the origin of the curve, the exponential term in the one-diode equation, limiting the FF depending on V_{oc} to a slightly higher value (around 83 % to 84 % maximum) of which the rest is lost due to parasitic resistances. In [12], a relationship for the maximal obtainable FF is given:

$$FF = \frac{\frac{qV_{oc}}{kT} - ln\left(1 + \frac{qV_{oc}}{kT}\right)}{1 + \frac{qV_{oc}}{kT}} \tag{2.4}$$

with q, the elementary charge, k the Boltzmann constant and T the absolute temperature. In reality, parasitic resistance losses reduce the FF even further, under optimum conditions to slightly higher than 80 %.

Since a solar cell in the dark acts similar to a typical diode, the IV-curve in the dark can be described by the one-diode equation:

$$I(V) = I_0 \left(e^{\frac{qV}{n_1 kT}} - 1\right) \tag{2.5}$$

where I_0 represents the diode saturation current, V the voltage, k the Boltzmann constant, T the temperature and finally n_1, the ideality factor, which is assumed to be 1. The current I equals the current density j via $I = j \cdot A$. The components of the saturation current I_0 can be calculated by starting from the formation of a pn-junction, where diffusion currents and field currents for holes and electrons level out each other, which leads to the one diode equation with the components of I_0. This is well explained in [13], and leads to

$$I_0 = A \left(\frac{q\, D_e\, n_i^2}{L_e\, N_A} + \frac{q\, D_h\, n_i^2}{L_h\, N_D}\right) \tag{2.6}$$

where D_e and D_h represent the diffusivity of electrons or holes, respectively, n_i is the intrinsic carrier concentration in silicon at room temperature, N_A the acceptor doping concentration, L_e and L_h the respective diffusion lengths and q the elementary charge. Since the saturation current is a measure for the quality of the pn-junction and can be referred to as a recombination current, it is necessary for the performance of the solar cell to keep it small, typically in the range of a couple of hundred femto Amperes.

Under illumination, the IV-curve changes by a constant factor of the light-generated current I_L.

$$I(V) = I_0 \left(e^{\frac{qV}{n_1 kT}} - 1\right) - I_L \tag{2.7}$$

This ideal model has its limitations for explaining real solar cell behaviour. A two-diode model is a better approximation and hence is explained in more detail in the following section 2.2.

Two-Diode Model

A more realistic model than the one-diode model for describing real solar cells is presented, which furthermore can be used to extract information out of the measured IV curve. An enhanced model including series and parallel (shunt) resistance as well as a second, in parallel connected diode accounting for recombination processes within the depletion region as well as edge recombination is presented. The two-diode model is schematically shown in figure 2.4.

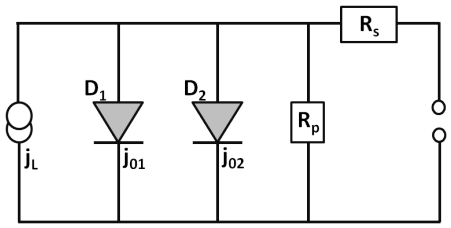

Figure 2.4.: Equivalent circuit diagram of a solar cell with the light-generated current density j_L, both diodes $D_1(D_2)$, their respective saturation currents $j_{01}(j_{02})$ as well as the parallel and series resistance, R_s and R_p

Schematically represented in the equivalent circuit diagram, the respective IV-curve is described by

$$j = j_{01}\left(e^{\frac{V-jR_s}{n_1 V_T}} - 1\right) + j_{02}\left(e^{\frac{V-jR_s}{n_2 V_T}} - 1\right) + \frac{V - jR_s}{R_p} - j_L \tag{2.8}$$

Different regions contribute in different manners to the saturation current density j_{01} of the first diode. Basically, the emitter, the base and the BSF separately consist of a saturation current density, which is added up to the total $j_{01} = j_{0e} + j_{0,b} + j_{0,BSF}$. The biggest contributor to the first diode's saturation current is normally the BSF for mono-crystalline silicon solar cells. The second diode saturation current density j_{02} gives the recombination in the depletion region as well as edge recombination, whereas the latter describes the recombination due to a depletion region in direct contact with a surface. A high j_{02}, typically above 2×10^{-8} A shows an influence on the IV-curve and hence the performance of the solar cell.
The two-diode model is mainly applied to fit illuminated and dark logarithmic IV-curves in order to extract parameters such as series resistance R_s, parallel resistance R_p and values for j_{01} and j_{02}.

2.3. Loss Mechanisms

Basically, it is possible to divide losses into two main groups as it is shown in figure 2.5, one being electrical, the other of optical nature. The first is further sectioned into ohmical losses such as parasitic resistances and recombination losses. Typically, four types of recombination losses in a solar cell occur. Besides three bulk recombination mechanisms, surfaces as an abrupt discontinuity of the lattice is strongly influencing the minority charge carrier lifetime. In fabricated solar

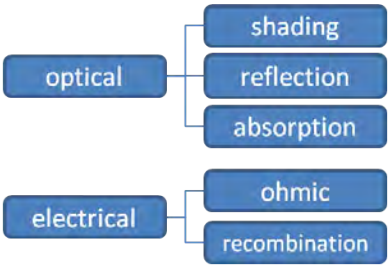

Figure 2.5.: Loss overview

cells, optical losses are crucial as well. Shading, reflection and parasitic absorption are the main sources of optical losses.

2.3.1. Bulk Recombination

In general, charge carriers are characterized by their lifetime τ, which is representing the time before they 'fall' back into the valence band and recombine. In the case of solar cells, the minority charge carrier lifetime is important, since the minority charge carrier needs to reach the pn-junction in order to contribute to the overall current. The distance, a minority charge carrier can diffuse within silicon is referred to as diffusion length $l = \sqrt{D\tau}$ and hence, besides strongly depending on the lifetime, the diffusivity D is important. Since recombination processes are affecting the minority charge carriers lifetime, it is important to discuss, which recombination processes are present in silicon. Basically, these recombination processes can be classified as intrinsic or extrinsic. While the omnipresent radiative and Auger recombination are of intrinsic nature, Shockley-Read-Hall and the latter discussed surface recombination are extrinsic recombination mechanisms. The dominating recombination process is limiting the lifetime via

$$\frac{1}{\tau_b} = \frac{1}{\tau_{radiative}} + \frac{1}{\tau_{Auger}} + \frac{1}{\tau_{SRH}} \tag{2.9}$$

where τ_{b} represents the bulk lifetime, $\tau_{\mathrm{radiative}}$ the lifetime resulting from radiative recombination and τ_{Auger} as well as τ_{SRH} lifetimes resulting from Auger and Shockley-Read-Hall recombination, respectively.
The dominating recombination process is the one with the shortest lifetime. The recombination rate $U = \frac{\Delta n}{\tau}$ demonstrates, that recombination within a semiconductor is a natural process, while the excited excess carriers Δn losing their excess energy mainly by three different ways, letting the semiconductor fall back into its thermal equilibrium.

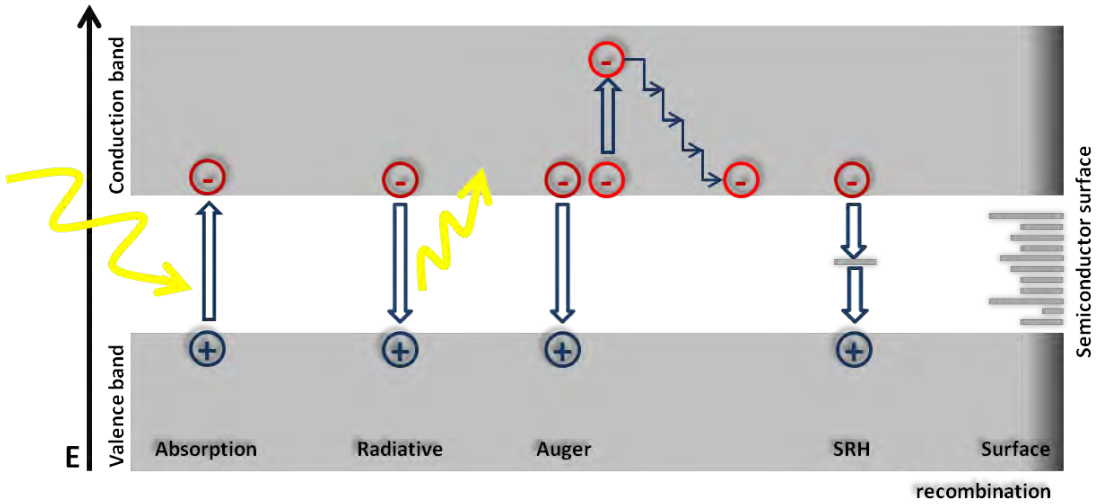

Figure 2.6.: Schematic display of absorption and three different bulk recombination losses as well as recombination at the semiconductor surface

Radiative band-to-band recombination As the inverse process of the photovoltaic effect, radiative recombination describes an electron, which is 'falling back' into the valence band and releasing its energy by emitting a photon with an energy equivalent to the band gap. More important for direct semiconductors such as GaAs (three-particle process), this recombination process is much unlikelier for indirect semiconductors like silicon due to the needed involvement of a phonon (four-particle process). The radiative recombination process gives a lifetime for a carrier corresponding to the following formula and is therefore strongly dependent on a material constant B (approx. $0.95\times10^{14}\mathrm{cm}^3/\mathrm{s}$ for silicon at 300 K [14]), excess carrier concentration Δn as well as bulk doping ($\mathrm{n_0}$ and $\mathrm{p_0}$):

$$\tau_{radiative} = \frac{1}{B(n_0 + p_0 + \Delta n)} \tag{2.10}$$

Auger recombination Auger recombination dominates for highly doped semiconductors or high injection conditions (more injected carriers than doping density), as it depends on the concentration of carriers. In n-type silicon, a recombining electron gives its energy to another electron, exciting it to a higher energy state, while itself falls into the valence band. Finally, the second electron relaxes back to the lowest available energy state within the conduction band by emitting phonons. Similarly in p-type silicon, an excited hole transfers its recombination energy to another hole, which than relaxes back by releasing phonons. The minority charge carrier lifetime from Auger recombination is determined by the following formula for n-type silicon [15]:

$$\tau_{Auger} = \frac{1}{C_n n_i^2 + C_p n \Delta n} \tag{2.11}$$

where $\mathrm{C_n}$ and $\mathrm{C_p}$ represent the Auger coefficients for n- and p-type material, respectively. Furthermore, $\mathrm{n_i}$ and Δn give the intrinsic electron concentration and the excess electron concentration. Therefore, Auger lifetime depends on base doping level and the injected excess charge carriers.

SRH (Shockley-Read-Hall) recombination Recombination via defect levels within the forbidden band (band gap) is described by the Shockley-Read-Hall theory. Several assumptions (see [15]) are made in order to conclude, that defect levels close to the middle of the forbidden band are the most effective recombination centres. Defect levels within the forbidden band are a result of impurity atoms within the silicon lattice or different kinds of defects. Basically, the SRH theory leads to a recombination rate $\mathrm{U_t}$ for a single-level defect located at $\mathrm{E_t}$ within the forbidden gap:

$$U_t = \frac{\nu_{th} N_t (np - n_i^2)}{\frac{n+n_1}{\sigma_p} + \frac{p+p_1}{\sigma_n}} = \frac{np - n_i^2}{\tau_{p0}(n + n_1) + \tau_{n0}(p + p_1)} \tag{2.12}$$

with n and p the respective charge carrier densities of electrons and holes, $\mathrm{n_i}$ the intrinsic carrier concentration and $\tau_{n0} = (\sigma_n \nu_{th} N_t)^{-1}$ the capture time constant for electrons and respectively for holes τ_{p0}, which comprises the thermal velocity ν_{th}, capture cross section σ and the recombination centre density $\mathrm{N_t}$.

As the recombination rate shows, it is proportional to (np - n_i^2). Using $U = \Delta n/\tau_{SRH}$, which assumes a simple exponential decay with the excess carrier density Δn and equalized excess carrier concentrations $\Delta n = \Delta p$, the SRH lifetime follows:

$$\tau_{SRH} = \frac{\tau_{p0}(n_0 + n_1 + \Delta n) + \tau_{n0}(p_0 + p_1 + \Delta p)}{p_0 + n_0 + \Delta n} \tag{2.13}$$

Figure 2.7 gives a general overview under which condition which recombination process dominates as a function of doping level. With increasing doping level, the Auger-recombination starts to dominate above SRH- and radiative recombination.

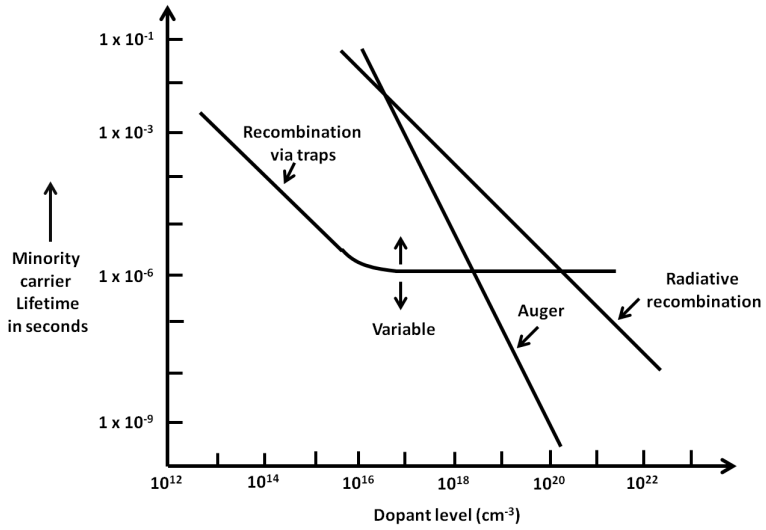

Figure 2.7.: Contribution (relative magnitude scale) of the three bulk recombination mechanisms to the minority carrier lifetime in order to allow an estimation of the dominating recombination mechanism as a function of the doping level; after [13]

Furthermore, the effective minority charge carrier lifetime is in general strongly injection-level dependent. This relationship is e.g. discussed by Kerr and Cuevas for differently doped n-type silicon samples passivated by silicon dioxide in [16], showing higher lifetimes for injection levels below 10^{16} cm^{-3} with reduced bulk doping level. Above an injection level of 10^{16} cm^{-3}, a strongly reduced effective lifetime is measured, which then gets independent of bulk doping level, the higher the injection level is.

2.3.2. Surface Recombination

For high-quality silicon, especially n-type, the minority charge carrier lifetime τ_b (further referred to as lifetime) in the bulk is high, up to several milliseconds. As a result of this high lifetime a long diffusion length $l = \sqrt{D\,\tau_{bulk}}$ of several times the wafer thickness follows. Therefore, the surface is very important for the lifetime and the performance of the solar cell. The front side is especially important for rear junction solar cells like the ones fabricated in this thesis. This is due to the fact that most of the light is absorbed within the first few micrometers of the silicon and carriers therefore need to diffuse through the bulk to the rear.

Surface recombination is described using the SRH theory. In general, the abrupt discontinuity of the lattice leads to the so called 'dangling bonds', referring to unbounded electrons of the silicon atoms at the surface. This results in a large density or even a continuum of defect levels (interface states) within the forbidden gap leading to a high recombination rate at the surface. The surface recombination velocity (SRV) describes the recombination as a velocity.
From the SRH-theory, equation 2.12 shows three basic dependences for the recombination rate of a single defect level within the forbidden gap. Besides intrinsic properties of the defect level such as the capture cross sections for the charge carriers or the energy level of the defect within the forbidden gap, the product of the surface concentration of electrons and holes is crucial. Furthermore, the density of defect levels at the surface, acting as recombination centres, severely affects the surface recombination rate. The latter two basic dependencies can be manipulated and hence allow to reduce the effect of the surface on the effective lifetime.
A classical approach to express the surface recombination rate U_s is given:

$$U_s = S(\Delta n_s) \cdot \Delta n_s \tag{2.14}$$

where U_s depends on the excess carrier concentration at the surface Δn_s as well as on the surface recombination velocity S for the specific surface excess carrier concentration Δn_s.
Removing residuals and contamination from the surface can be done by either an easier or enhanced approach, such as HCl/HF cleaning or RCA cleaning (described later), respectively. Furthermore, phosphorous gettering during a phosphorous diffusion can reduce the contamination in the bulk as well, leading to a minimum of impurity atoms in the bulk. These impurities could function as recombination centres at, and close to the surface or diffuse into the silicon during high temperature processing steps and limit the effective bulk lifetime.

Since the surface recombination rate depends on the concentration of minority and majority charge carriers at the surface, the injection level has a significant effect. In this work, evaluation is usually carried out at working conditions, hence at approximately 10^{15} cm^{-3} excess charge carrier concentration.

In principle, unpassivated silicon surfaces feature an infinite recombination velocity, although there is an upper limit to the recombination rate since the thermal velocity of the free minority charge carriers $v_{th} \approx 10^7$ cm/s is limiting the diffusion of carriers to the surface. Passivation of the solar cell surface therefore is an important step to reach higher efficiencies for high bulk lifetime material. For extremely well passivated and lowly doped surfaces, the surface recombination velocity can be lowered to less than 1 cm/s. In the case of standard commercially available solar cells featuring a BSF the effective SRV has typical values from 1000 cm/s down to 200 cm/s [17]. Nowadays, the effective SRV is reduced even further. The effective SRV has been introduced to account for the case of band bending conditions as a result of high doping

concentrations close to the surface. This is explained in detail after an analysis of the flat band case close to the surface.

A detailed study of dependences is presented for the results of the SRH theory in p-type silicon (similar for negatively doped silicon). Close to the surface of the silicon, band bending needs to be taken into consideration. First, SRH theory is approached with flat band conditions, since these are still analytically solvable. This means, that no electric field from fixed charges or a high-low junction are present. Furthermore, to have a look at the real surface situation, the surface recombination is analysed under band bending conditions. This includes inversion, accumulation and depletion conditions. The band bended situations are discussed in section 2.5, since they apply mostly for cases in which actions against high surface recombination velocities are taken. The following result from Aberle [15] is calculated under flatband conditions, meaning that no change in the doping as well as no field-effect is present. Equal excess carrier concentrations $\Delta n_s = \Delta p_s$ are assumed at the surface.

$$S(\Delta n_s) = \frac{n_0 + p_0 + \Delta n_s}{\frac{n_0+n_1+\Delta n_s}{S_{p0}} + \frac{p_0+p_1+\Delta n_s}{S_{n0}}} \tag{2.15}$$

with

$$S_{n0} = \sigma_n \nu_{th} N_{st} \qquad S_{p0} = \sigma_p \nu_{th} N_{st} \qquad n_1 p_1 = n_i^2 \tag{2.16}$$

$$n_1 = n_i exp\left(\frac{E_{st} - E_i}{kT}\right) \qquad p_1 = n_i exp\left(\frac{E_i - E_{st}}{kT}\right) \tag{2.17}$$

with $\sigma_{\mathrm{n(p)}}$ representing the capture cross sections of electrons (holes), respectively. Thermal velocity ($\approx 10^7$ cm/s in silicon at 300 K) is abbreviated by ν_{th}, $\mathrm{n_i}$ the intrinsic carrier density at 300 K in silicon, $\mathrm{E_i}$ the middle of the forbidden gap, $\mathrm{N_{st}}$ the density of surface states in $\mathrm{cm^{-2}}$, $\mathrm{E_{st}}$ the energy level of the defect and $\mathrm{n_s(p_s)}$ the respective carrier density at the surface.

It can be seen in equation 2.15, that the surface recombination velocity depends on the injection level Δn_s as well as on the base doping (p_0 and n_0). It can be shown, that for very low and very high injection conditions no dependence on the injection level exists and that therefore the majority and minority charge carrier capture cross sections of the defect level and the doping levels are mainly affecting the SRV. Especially the ratio of the capture cross sections of electrons and holes of the defect level has a huge effect on the SRV. A more detailed study on surface recombination can be found in [15, 18].

The condition of equal carrier concentration at the surface does not apply for band bending conditions, which are a result of electric fields at the surface. Therefore, the hole and electron concentration needs to be calculated as a function of the distance from the surface in order to calculate the surface recombination rate from equation 2.12. This leads to the introduction of the effective surface recombination velocity $\mathrm{S_{eff}}$, which depends on the excess minority carrier concentration at a *virtual* surface at position d from the surface, right where the surface space charge region ends and the neutral bulk starts.

$$S_{eff} = \frac{U_s}{\Delta n(x = d)} \tag{2.18}$$

This situation is explained in more detail in section 2.5 and shown in figure 2.11 with the help of PC1D simulations.

2.3.3. Ohmic Losses

There are two kinds of parasitic ohmic losses in solar cells. Series resistance and shunt resistance both affect the IV-curve characteristics in different ways, thereby reducing the FF. The effect of parasitic resistances on the IV-curve is shown in figure 2.9.

Series resistance Series resistance consists of different contributors as it is shown in figure 2.8. It mainly affects the IV-curve by reducing the current output for the high voltage range close to V_{oc}, leading to a reduction of the FF. For extremely high series resistances, j_{sc} is reduced as well. The biggest contributors to the total series resistance within this work are the fingers R_F and the emitter $R_{lat,emitter}$ as well as the contact resistances R_{C1} and R_{C2}. Well performing solar cells usually have a combined series resistance of $R_{Total} \approx$ 0.5-0.6 Ωcm^2 [19], of which the line resistance in the fingers, the emitter sheet resistance and the contact resistance are typically the biggest contributors.

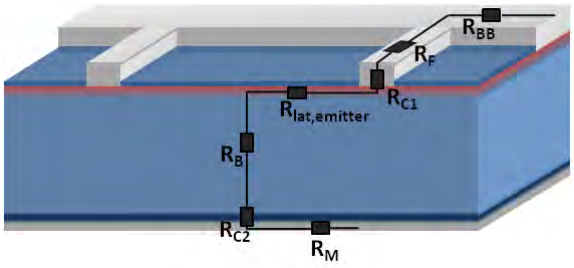

Figure 2.8.: Sources of series resistance starting from the front metallization, the busbar and fingers R_{BB} and R_F, the contact resistance R_{C1}, the lateral series resistance $R_{lat,\ emitter}$, the bulk resistance R_B, the contact resistance to the rear metallization R_{C2} and finally, the lateral series resistance in the rear side metallization R_M

For this thesis, the lateral emitter series resistance and the contact resistance are the two most interesting. The contact resistance R_C contribution can be calculated using [19]

$$R_C = \rho_c \frac{A_{unit}}{A_{contact}} \tag{2.19}$$

where ρ_c equals the contact resistivity, A_{unit} the smallest symmetric element of the front geometry and $A_{contact}$ the contact width. The lateral emitter series resistance $R_{lat,emitter}$ is calculated using

$$R_{lat,emitter} = \frac{1}{12} R_{sheet} (d_F - \frac{w_F}{2})^2 \tag{2.20}$$

with R_{sheet} the emitter sheet resistance, d_F the finger distance and w_F the finger width.

Shunt resistance Short circuits, resulting in currents that are able to bypass the junction, for example current flow at the solar cell's edge, result in a low shunt resistance. Furthermore, emitter damage can result in a low shunt resistance since the effectiveness of the junction to spatially separate electron-hole pairs is reduced. Therefore, shunts, such as conducting needles through the pn-junction lead to a low shunt resistance. This reduces the current output over nearly the whole voltage range, leading to a reduction in the FF and for extremely low values to an reduction of the V_{oc}. Shunt resistance values of roughly below 5000 Ωcm^2 negatively affect the IV-curve.

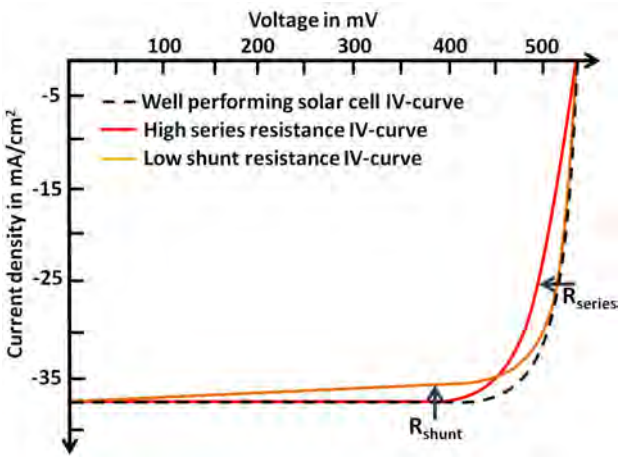

Figure 2.9.: Schematically presented effect of high series resistance (approx. 1 Ωcm^2) and low shunt resistance (500 Ωcm^2) on the IV-curve

2.3.4. Optical Losses

Optical losses occur mainly before the incident light even enters the solar cell. Three main mechanisms reduce the optical performance of a solar cell.

Shading Shading of the front side metallization reduces the light-coupling area by about 5 - 8 %. However, busbars and fingers are needed in order to use the voltage difference between front and rear side and collect the current. Width, height and pitch of the fingers affect the series resistance, while the lateral resistance in the emitter needs to be taken into consideration for the pitch between the fingers. Therefore, a compromise between low series resistances and low shading must be found.

Front reflection Due to silicon's high refractive index of n = 3.88 at 633 nm, the reflectivity from air to silicon is quite high. From Fresnel's law (for perpendicular incidence)

$$R = \left(\frac{n_{air} - n_{Si}}{n_{air} + n_{Si}} \right)^2 \tag{2.21}$$

it follows, that around 30 % of the incident light on a plain silicon wafer is reflected. Since this would reduce the solar cell performance enormously, the idea of texturing and coating the surface was implemented. The possibilities to reduce front side reflection will be discussed in the optimization section 2.4. For the second passage through the wafer, the front side's internal reflection also needs to be enhanced, reducing transmission losses at the front, which contribute to the totally measured reflection.

Internal reflection Once the light is coupled into the semiconductor, it still can leave the solar cell or be absorbed at the rear side. This is especially the case for light in the long-wavelength regime, because it is hardly absorbed within the first passage through the wafer, leading to further losses. For metallized rear sides, values of the internal reflection given in the literature range from 65 % up to 78 % [20, 21, 24], while the rest is absorbed by the metallization (eutectic and aluminium paste). This value can be enhanced by using a dielectric passivation on the rear side, which effectively mirrors most of the light back into the cell (about 95 %) [24].

2.4. Optical Loss Reduction

Optimization of optical performance is crucial for using most of the incident light from the solar spectrum. Theoretically, a maximum short-circuit current density of approximately 46.4 mA/cm^2 is possible (calculated from the ASTM G163 reference spectrum in the wavelength range 300 - 1200 nm). Under ideal circumstances this equals the light-generated current density. Pure polished silicon surfaces have a reflection ranging from 30% for low photon energies up to over 50 % for high energy photons [11], leading to low short-circuit currents and overall low conversion efficiencies. In order to reduce losses, several attempts can be made. One approach is to increase the average contact points of an incident light ray with the surface and by the angle of refraction, the length of the light path in the cell. Another approach is to use thin anti-reflection coatings made of dielectric materials. Further, light losses can be reduced by enhancing the internal reflection, which is possible by partly coating the rear with a dielectric. This is called light trapping.

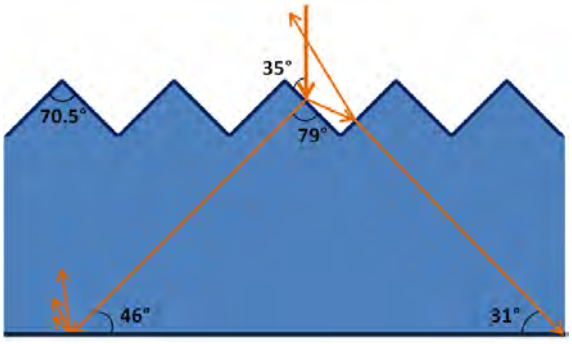

Figure 2.10.: Schematic of a solar cell with a texture on the front side, which leads to several contacts of an incident ray with the surface. Important angles are given. Furthermore, a dielectric rear side passivation enhancing the internal rear reflection is shown on the rear.

Texture Increasing the average contact points of an incident ray with the silicon surface is done by texuring. Texturing is performed by an alkaline, anisotropic etch for monocrystalline silicon wafers, resulting in a randomized pyramidal structure on the surface. Typical etch solutions are a mixture of KOH and an alcohol. Within this work mostly Cz material with (100) crystal orientation was used, which leads to a preferred etching crystal orientation with pyramidal surfaces representing the (111) crystal direction (indexing is done using the Miller indices). Randomized pyramids with heights of up to 7 µm are typical. Besides enhancing the probability of coupling the light into the semiconductor, the angle of transmitted light differs from perpendicular incident light, leading to enhanced path length in the bulk. This in turn results in an higher absorption of the light due to the dependence to the light path length.

Anti-reflection coating Thin transparent layers, so called anti-reflection coatings (ARC) are used to reduce reflectance even further. The principle is based on destructive interference, where the thickness d of the coating is chosen to be $d = \lambda/(4\,n_0)$, with λ being the incident wavelength and n_0 the refractive index of the ARC with $n_0 = \sqrt{n_{air}\,n_{si}}$. For standard solar cells, this leads to a thickness of the most used anti-reflection coating

silicon nitride with n = 2.05 of 75 nm with a minimum of reflectance at 600 nm wavelength, which is optimized for the peak of solar irradiation. For completeness, there is also parasitic absorption in silicon nitride, especially for wavelength between 300 nm to 400 nm. Conveniently, the anti-reflection coatings such as silicon nitride or silicon dioxide have also usable properties concerning surface passivation and hence are typically used as anti-reflection and passivation coatings.

Internal reflection Although most of the light is absorbed within the first pass through the cell, a further gain in light-generated current density j_L and hence in j_{sc} can be obtained by enhancing the rear side's internal reflectance. This can be done by passivating the rear side partly with a dielectric, raising the rear internal reflectance from 65-77 % [24, 25] for full aluminium paste covering of up to 95 % for full rear passivation [24, 26]. Moreover, evaporation of aluminium has shown an increase in rear internal reflection compared to an aluminium alloyed rear, since absorption is mainly occurring in the eutectic and the aluminium paste.

2.5. Surface Passivation

In section 2.3.2 the properties of surface recombination are presented. Two options to reduce the effect of the surface on the minority charge carrier lifetime can be identified.

Chemical passivation The reduction of the density of surface states can be realized by chemical passivation. Passivation layers such as silicon dioxide, silicon nitride and aluminium oxide are able to saturate the 'dangling bonds'. This is carried out by either moving the effective surface of the silicon or saturating as many as possible dangling bonds, by introducing e.g. hydrogen.

Field-effect passivation A second option is provided by the dependence of the surface recombination velocity (SRV) on the excess carrier concentration at the surface, which is highest if the total concentrations of minority and majority carriers are equal ($n_s = p_s$), assuming the same capture cross sections for both. A built-in high-low junction can lead to a reduction of the minority carriers at the surface, which on the other hand leads to a decrease of the recombination rate. This is the back surface field (BSF) or front surface field (FSF). Similarly, the ratio of majority to minority carriers is enlarged by an emitter as well. A built-in high-low junction or an emitter can be created by performing a diffusion step. In commercially available p-type silicon solar cells, the use of the already mentioned BSF reduces the minority charge carrier concentration at the surface as well and is conveniently created during contact formation on the rear applying a co-firing step.

Furthermore, dielectric passivation layers featuring fixed charges can be used in order to effectively shield the surface from minority carriers and hence reduce the recombination rate, as well. Field-effect passivation leads to a bending of the band structure at the surface, which in the first case is a result of electrical charges within the dielectric passivation layer, close to the surface of the semiconductor. For high amounts of fixed charges at the surface this leads to the formation of a surface space charge region, in which free carriers are repelled and ionized atoms stay behind, similar to the situation in the pn-junction. Band bending can result in three different cases: inversion, accumulation and depletion. Girisch et al [27] and Aberle [15] used the extended SRH formalism proposed by Grove and Fritzgerald [28, 29] to show, that depletion conditions are leading to a high SRV,

whereas inversion and accumulation conditions can reduce the SRV significantly. The band diagrams were simulated using PC1D [61] with fixed charges on a thin wafer of silicon (800 nm - for higher resolution) and can be seen in section 2.11.

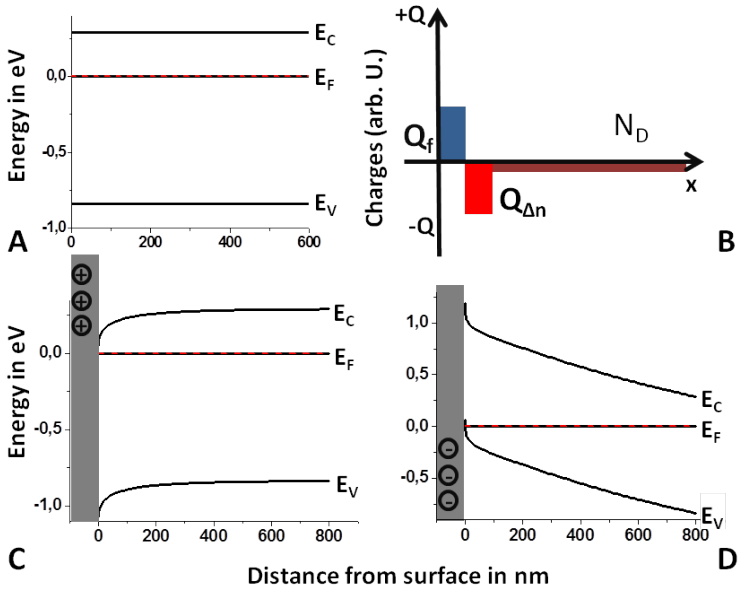

Figure 2.11.: Simulated schematic representation of the band conditions for a moderately n-type doped silicon wafer ($N_D \approx 4.1 \cdot 10^{14}$ cm^{-3}): **A**: flat-band conditions, **B**: charge distribution (not simulated), **C**: Accumulation of electrons close to the surface, **D** inversion

2.6. Passivation Layers

This section focuses on the fabrication and properties of selected passivation layers. Silicon dioxide, silicon nitride and aluminium oxide are discussed. Whereas the first and second are very common, aluminium oxide becomes increasingly important for the passivation of p-type silicon, both moderate to highly doped surfaces. In general, stacks are applied in order to protect passivation layers against influences from further processing steps. In this thesis, stacks with either silicon dioxide or aluminium oxide as passivation layer are covered with a silicon nitride capping layer.
In the following sections, the fabrication and properties of silicon dioxide, silicon nitride and aluminium oxide are described.

2.6.1. Silicon Dioxide

Thermal oxidation of silicon surfaces is well known from the research in the semiconductor industry and is usually carried out in a quartz tube at temperatures ranging from 800 °C up to 1200 °C degrees. The oxidation can take place using two different oxygen sources. Wet oxidation, which uses ultra pure water vapour for the growth of an oxide layer into the wafer,

is faster than dry oxidation. The latter uses an oxygen flow. The oxide is growing amorphously from the outside in the silicon surface and therefore is bringing the effective surface of the silicon wafer into the bulk. This improves the quality and purity of the surface. An oxide layer of thickness d_{ox} consumes only around 0.445 d_{ox} of silicon [30]. Since the effective SiO_x/Si interface is moving into the wafer, the direction of growth leads to a thickness dependent growth rate. Starting with a growth rate which is proportional to the time t, it slowly reduces to its root $\sqrt{t}$. Moreover, crystal orientation plays an important role, since in the crystal direction (111) the effective growth rate is three to four times faster than on (100) surfaces [15] and is increased for heavily doped surfaces [30], as well. Within this work, only dry oxidation was used for the front and partly for rear side passivation, because the best chemical passivation layers have been obtained with this method.

Silicon dioxide can be used as an anti-reflection coating, for chemical passivation as well as for field-effect passivation. While the first is not very effective, since the refractive index of silicon dioxide is $n = 1.46$, leading to high reflectivity in the important part of the solar spectrum (wavelengths below 1200 nm), the latter two are discussed in more detail.

Chemical passivation is obtained by reducing the surface state density or interface state density N_{it} within the band gap of silicon. This is achieved by bringing the effective surface of silicon into the wafer, forming a Si/SiO_2 interface. This oxide layer induces four different kinds of interface states in the forbidden gap of silicon. One effect is the reduced forbidden gap energy E_{gap} due to stretched Si-Si bonds, leading to a softening of the band edges close to the surface. The three remaining sources of interface state densities depend on how the 'dangling bonds' are partly saturated. Although several surface states exist, depending on the type of oxidation and the crystal orientation, values as low as $N_{it} = 10^9$ cm^{-2} can be achieved. For example, the oxidation in the (100) direction features a much lower interface states density than in the (111) crystal direction. In comparison, typical non-passivated silicon surfaces have defect level state densities of $N_{it} = 10^{13}$ cm^{-2} [15].

Field-effect passivation by silicon dioxide layers is mainly contributed to positive fixed charges within the first nanometres of the silicon dioxide, close to the Si/SiO_2 interface. These positive fixed charges are a result of the interaction of dangling silicon bonds with three oxide bonds. Fixed charge values for thermally grown silicon dioxide layers of up to $Q_f = 3{\times}10^{11}$ cm^{-2} have been found [22]. Besides fixed charges, mobile charges such as alkali ions have been a problem, but nowadays, the purity of wafer processing has been improved, making these kinds of charges nearly unimportant. Moreover, charges induced by the interface states exist as well. But compared to the density of fixed charges Q_f, their contribution is negligible. The number of fixed charges is at least one order of magnitude smaller than the ones obtained by using silicon nitride or aluminium oxide (other polarity). Therefore, field-effect passivation by silicon oxide is of minor importance.

Different doping levels lead to varying results in the effectiveness of the silicon dioxide layer for passivating silicon surfaces. Especially, high-resistivity n- and p-type silicon can be well passivated using silicon dioxide, achieving S_{eff} values of below 10 cm s^{-1} [17]. While low-resistivity n-type material can still be suitably passivated with silicon dioxide, highly doped p-type material has its problems since the positive fixed charges in the oxide layer are reducing the surface concentration of the majority carriers. In principle, this results in electron and hole concentrations that are getting closer to each other and in turn, this leads to an increased surface recombination velocity.

2.6.2. Silicon Nitride

Silicon nitride can be used for different purposes. From front side anti-reflection coating to rear side passivation and capping layer, the applications are wide. The refractive index of silicon nitride can be tuned in the range n = 2.0-2.4 by changing the stoichiometric composition, hence increasing the silicon concentration. That makes it suitable for the use as an anti-reflection coating. It is important to notice that with increasing refractive index the extinction coefficient and hence the absorption for wavelengths below 500 nm is strongly increased and therefore, high refractive indices result in parasitic absorption, which affects solar cell performance [31].

Amorphous silicon nitride can be deposited by chemical vapour deposition (CVD), which is commonly done by means of plasma-enhanced CVD (PECVD). Two different methods are commonly applied in the photovoltaic industry, direct PECVD and remote PECVD, whereas the deposited layers in this work are referred to as CT-SiN_x and SiNA-SiN_x, respectively. On the right side in figure 2.12, a schematic of a direct PECVD is shown. The direct PECVD generally uses an electromagnetic field with a frequency of typical 13.56 MHz (high-frequency method) to excite the processing gas, Ammonia NH_3. Within this work, direct PECVD was used by applying the low-frequency method at frequencies of approx. .The deposition is usually carried out at temperatures between 300 °C to 500 °C degrees in a silane SiH_4 atmosphere, which allows the incorporation of hydrogen in the silicon nitride layer. This has the advantage of strongly increasing the minority charge carrier lifetime, especially in multi-crystalline material. Then, the deposited layer can be referred to as a-SiN_x:H, containing up to 40 atomic-% of hydrogen, which is freed during further high temperature processing and is saturating recombination centers and 'dangling bonds' in the bulk and at the surface. The same incorporation of hydrogen into the silicon nitride layer is found for remote PECVD, which is shown on the left in figure 2.12. The main difference to direct PECVD is the location, where the plasma is ignited. For silicon nitride, which is deposited by means of remote PECVD, the coated wafers are not directly in contact with plasma or close to it. More details about PECVD of silicon nitride can be found in [15, 32].

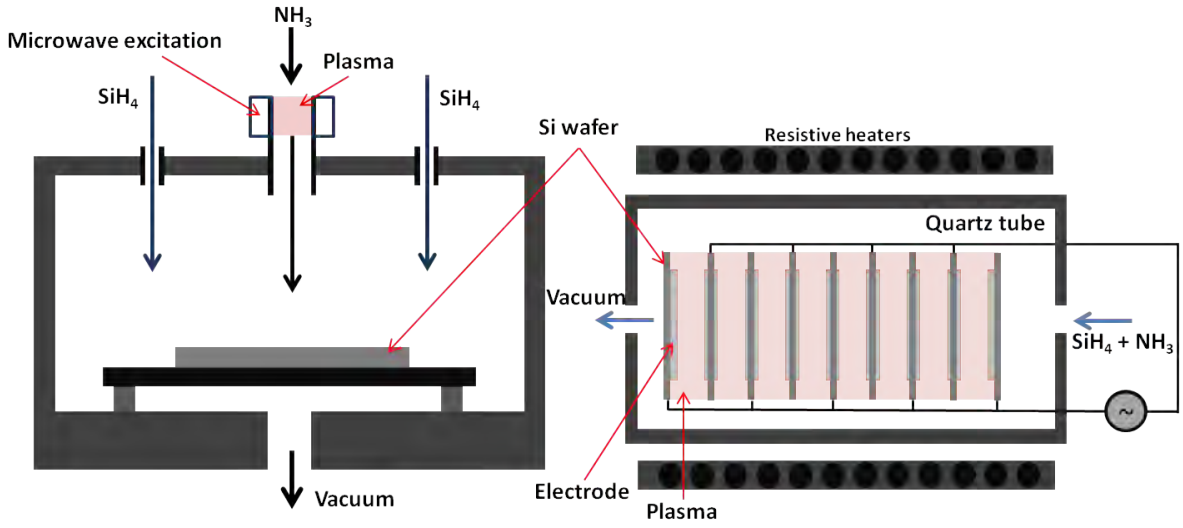

Figure 2.12.: Left: Remote PECVD; Right: Direct PECVD - after [15]

The properties of silicon/silicon nitride interfaces are a relatively low density of surface states, although chemical passivation is not as effective as it is for SiO_2. Interface densities of $D_{it} = 10^{11}$ - 5×10^{12} cm^{-2} eV^{-1} at midgap ($N_{it} = \int D_{it}\, dE$) have been obtained. A large density of positive fixed charges ranging from $Q_f = 10^{11}$ to 5×10^{12} cm^{-2} [15], allows strong field-effect passivation (depending on the deposition technique and processing parameters).

2.6.3. Aluminium Oxide

Aluminium oxide provides excellent surface passivation properties, which have become increasingly interesting for the use on silicon surfaces. One main advantage, compared to silicon dioxide or nitride is the polarity of the fixed charges. While silicon dioxide and nitride both exhibit positive fixed charges, aluminium oxide contains a high amount of negative fixed charges that makes it suitable for passivating highly doped p-type surfaces. A large amount of fixed charges ranging from $|Q_f| = 10^{12}$ - 1.3×10^{13} cm^{-2} lead to a strong field-effect passivation. Furthermore, chemical passivation of the silicon surface reduces the interface density states to around $D_{it}= 2\times10^{12}$ $eV^{-1}cm^{-2}$ or even lower, depending on the deposition method [33]. The qualtiy of chemical passivation by Al_2O_3 has been shown by means of an corona charging experiment, in which the field-effect has been zeroed by the deposition of positive charges on top of the passivation layer and is shown in figure 2.13 **A**. This results in a surface passivation only by means of chemical passivation and leads to lifetimes of around 100 µs [33].

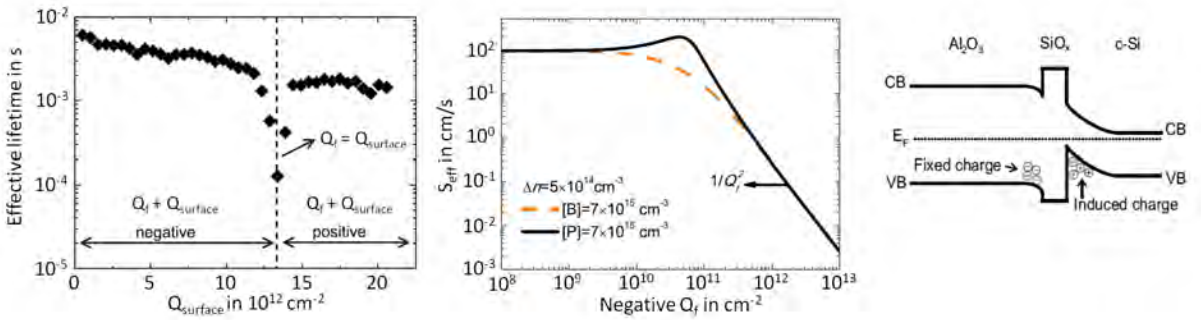

Figure 2.13.: **A** Effective lifetime as a function of total charges on the surface for a 26 nm thick Al_2O_3 layer; for fixed charges in the layer Q_f and deposited $Q_{surface}$ onto it. **B** Simulation of the effective SRV at an injection level Δn for moderately doped p- and n-type silicon for increasing Q_f. **C** Schematic band diagram of n-type silicon surface, passivated with an aluminium oxide layer, where CB represents the conduction band edge and VB the valence band edge. After and from [33].

Many different deposition techniques exist, which results in a wide range of values for fixed charges and interface density states. Within this work, Atomic Layer Deposition (ALD) has been used, whereby a precursor called Trimethylaluminium [$Al(CH_3)_3$] reacts with oxygen gas, which acts as an oxidizing agent. In general, a growth rate of 1 Å per cycle is achieved for a temperature of 300 °C [34]. Within this work, aluminium oxide is deposited using a FlexAL-reactor from Oxford Instruments (rpa-ALD), in which the plasma is lid by an alternating magnetic field (remote plasma-assisted ALD).
An interfacial silicon dioxide layer SiO_x formed during annealing [35], between the silicon and aluminium oxide, has been suspected to play a major role for the formation of the negative

fixed charge [33]. The negative fixed charges seem to be originating from Al vacancies, which are a result of a preferred orientation of Al bondings close to the interfacial layer [33]. In figure 2.13 **C**, the band diagram including a thin interfacial oxide layer is shown. Due to the repelling of majority carriers at the surface, a depletion region is formed close to the interfacial SiO_x layer. This results in band bending. Furthermore, the fixed charges are shielded by the accumulation of the minority carriers, which leads to inversion.

The effect of field-effect passivation on the underlying substrate depends strongly on the doping type and level. For n-type surfaces, field-effect passivation repels the majority carriers (electrons) from the surface, which leads for large densities of negative fixed charges to inversion, since more holes exist close to the surface than electrons. At p-type surfaces, high-quality aluminium oxide passivation leads to an accumulation of the majority carriers, resulting in a strong increase of the ratio of majority to minority charge carrier concentrations. The amount of fixed charges is crucial for field-effect passivation, since Hoex et al. [33] showed, that S_{eff} scales with $\frac{1}{Q_f^2}$ starting at a fixed charge of $|Q_f| = 3{\times}10^{11}$ cm^{-2}. In Figure 2.13 **B** an important effect is shown on moderately doped n-type silicon. While p-type silicon exhibits no increase of the effective SRV (S_{eff}) at around 10^{11} cm^2 negative fixed charges in the aluminium oxide layer, negatively doped silicon shows an increase in SRV. This is due to the fact, that electrons on the surface of n-type silicon are pushed away and hence the ratio of minority to majority carrier gets equalized, when the effective SRV is peaking. For higher negative fixed charges of the aluminium oxide, the electrons, therefore the majority carrier concentration gets even smaller at the surface than the minority charge carrier concentration, leading to the in figure 2.13 **C** visible effect of a band inversion. Then, the S_{eff} decreases with $Q_f{}^2$.

2.7. Alloying of Aluminium in Silicon

Within this work, aluminium is alloyed with n-type silicon at the rear of the wafer to form the emitter. This takes place while the Al-Si interface gets molten, which starts at the melting point of Al at 660 ℃, when the co-firing process takes place. Huster [25] describes the formation of the back surface field (BSF) within a p-type doped silicon wafer. Since the background doping has no influence on the alloying process, the emitter formation is explained using the model proposed by Huster. In figure 2.14, the binary phase diagram of aluminium and silicon is given. The phase diagram shows the thermodynamic behaviour for different concentrations of aluminium-silicon alloys and therefore is key for understanding the formation of the emitter.
The first step starts with bringing the aluminium accurately defined on the wafer, which is done by screen-printing an aluminium containing paste on the rear surface of the wafer. Besides aluminium in particles in sizes from 1-10 µm, which are encapsulated with a thin aluminium oxide layer, the paste also contains glass frites for improved sintering, organic binders and solvents for improved printing properties such as viscosity and stability on fresh air.
In order to have defined edges and structures, which are covered with aluminium paste, a screen is used as a mask, which is made out of small braided stainless steel wires, that are covered with a resist. Typically, about 5 to 7 mg/cm^2 is screen-printed on the rear, leading to a thickness of approx. 30-40 µm [25].
The alloying process takes place within an infra-red belt firing furnace, in which the wafer is placed on a chain and is transported through different temperature zones. The zone's temperature and the chain speed can be varied, which was done within this work.
While the screen-printed wafer passes through several temperature zones within the furnace, temperature changes lead to different conditions of the Al-Si interface, moving the alloy along

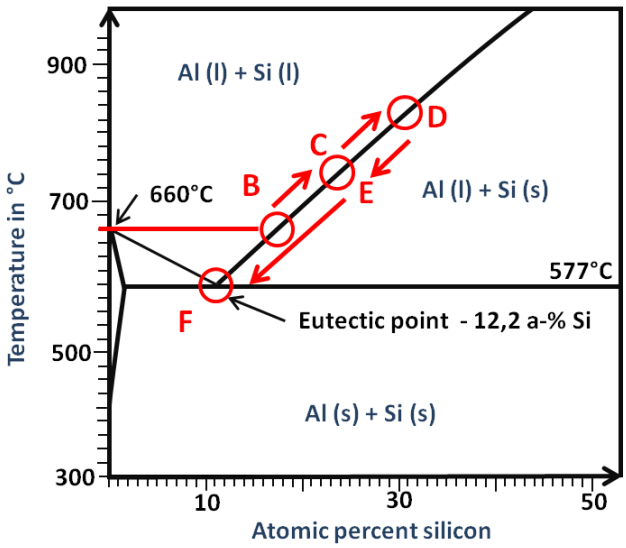

Figure 2.14.: Part of the Al-Si binary phase diagram after Murray [36] with different interesting points highlighted

the liquidus curve, which is explained below and schematically shown in figure 2.15

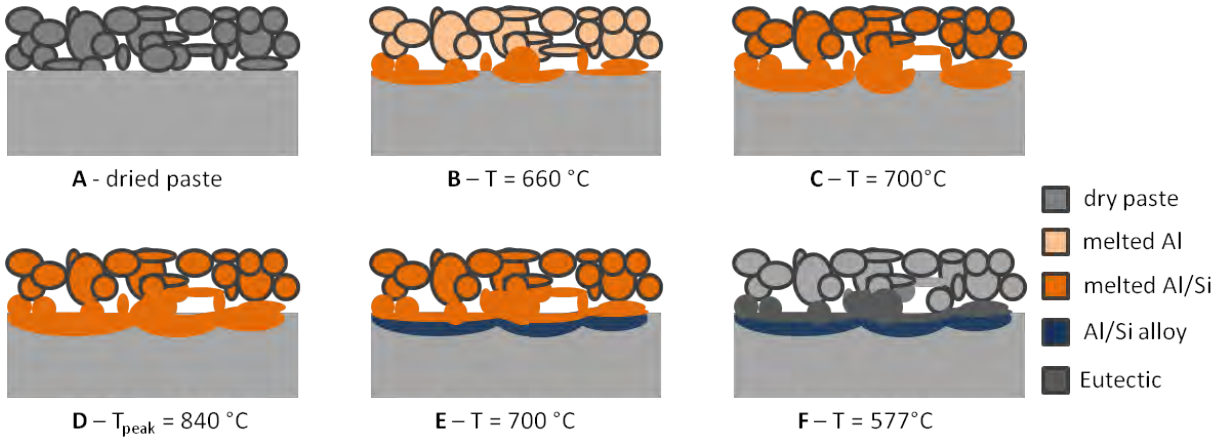

Figure 2.15.: Schematic representation of the aluminium alloying in silicon with **A** the drying of the paste, **B** heating up, **C** the melting, **D** the reached peak temperature, **E** the actual alloying process and **F** the solidification

A - Paste drying A short anneal for about one minute leads to the evaporation of incorporated solvents, creating a porous matrix of aluminium filled oxide shells, with total residual paste contents of 50-70 % aluminium [25].

B - Heating up After drying of the paste, increasing temperature in a bigger, second chain firing furnace leads to a burning out of the remaining organic binders, while the wafer is

heated up to a few hundred degrees. When a temperature of 660 °C degrees is reached, the aluminium in the oxide shells begins to melt. The oxide layers locally break, leading to direct contact between the aluminium and silicon. The melting can be seen in the measured temperature profile of the wafer, as a small plateau occurs as a result of the latent heat. Silicon dissolves in the aluminium melt, following the liquidus curve of the silicon and aluminium alloy. The oxide shells, which are natively about 1 nm thick [25], get thicker and stabilize the residual paste matrix.

C - Melting With increasing temperature, more and more silicon dissolves in the increasing amount of molten aluminium. The locally broken oxide shells keep on growing in thickness and stabilize the porous matrix even further. Aluminium and silicon both experience strong diffusion in opposite directions. While the silicon dissolves in the molten inner part of the shells travelling through the openings of the oxide shells caused by sintering of the glass frittes, the aluminium needs to flow in direction of the wafer surface.

D - Peak At the maximum temperature of the co-firing process, about 30 atomic-% silicon has dissolved in the liquid aluminium. A liquid Al-Si lake should, under ideal situations, cover the whole rear of the solar cell.

E - Alloying During cooling down, the silicon transport is reversed, as the system moves back along the liquidus curve in the binary phase diagram to lower solubility for lower temperatures. While more and more silicon is rejected from the melt, it recrystallizes epitaxially at the rear surface of the wafer, incorporating aluminium atoms according to their solid solubility at a given temperature. This leads to the formation of a positively doped region with a surface concentration of up to $3 \cdot 10^{19}$ atoms per cm^2 (see figure 2.16).

F - Solidification Reaching 577 °C, the remaining aluminium lake solidifies, leading to the formation of the eutectic layer with 12.2 atomic-percent of silicon remaining.

Typical aluminium-alloyed emitter have a profile similar to the one shown in figure 2.16. In general, alloying depth, surface concentration and trend of the curve are depending on the used aluminium paste. Ordinarily, the exact composition is unknown. The used pastes are described by acronyms, that are used here at the University of Konstanz. A typical value within this work for the surface concentration of positively doped surfaces was around 2-3 $\cdot 10^{19}$ atoms cm^{-3}, which leads to an overall sheet resistance of roughly 10 Ω/sq for an emitter depth of 5 µm. This high surface concentration is mainly attributed to boron that is added to the aluminium paste.

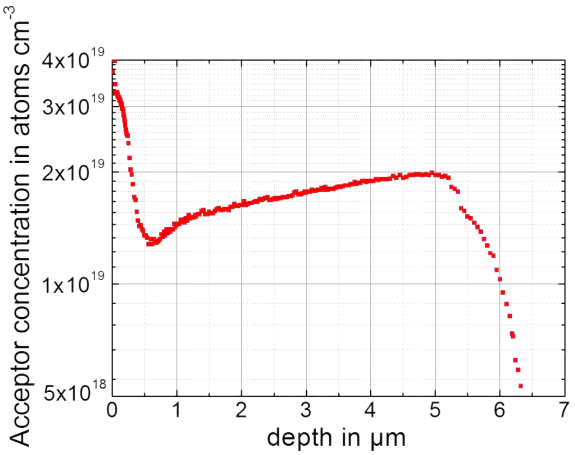

Figure 2.16.: Typical emitter profile measured by ECV within this work

3. Characterization Methods

In this part, the most important characterization methods are briefly described. At the beginning, the sun simulator that gives the IV-characteristics of the solar cells is shortly presented. This is followed by a description of the spectral response measurement tool, the photoconductance decay setup and its different measurement methods as well as an introduction in the electroluminescence and photoluminescence measurement technique. Finally, the LBIC technique, which allows to locally resolve the EQE is briefly explained.

3.1. Sun Simulator

Solar cell IV-characteristics under illumination are measured using a sun simulator. Normalized conditions, the so called standard testing conditions (STC) are generated. Standard testing conditions involve a solar cell temperature of 25 °C and an illumination with an intensity of 1000 W/m^2 using the AM 1.5G spectrum.

A previously characterised solar cell with a known short-circuit current density $j_{sc,cal}$ is used as a calibration cell in order to adjust the intensity of the lamp to an intensity of one sun. The calibration is repeatedly done, normally after every third measurement, in order to account for variations of the intensity. The solar cell is contacted on the front side with several probes (number depends on size of the cell), through which a current can be taken off the cell. Another probe is able to measure the output voltage.

For measuring the solar cell, a voltage ranging from -0.2 up to +0.7 Volt is applied on the cell, leading to a current flow under illumination. The current and the voltage together, taken as a series of measurements, lead to a current-voltage (IV) curve, as the one shown in figure 2.3. After the measurement is finished, the computer displays the FF, j_{sc}, V_{oc} and efficiency η as well as the whole IV-curve. Since the temperature is affecting V_{oc} by approximately 1.88 mV per Kelvin, accurate measurement of the temperature is needed and a proper adaption is done later on using $\Delta V_{oc} = \Delta T \cdot 1.88$ mV/K where ΔT represents the temperature difference to the STC and ΔV_{oc} the needed offset to the measured value of V_{oc}. Furthermore, the short-circuit current density is adapted to the change in illumination via a linear fit between two calibration measurements and the measured change in their calibration short-circuit current density $j_{sc,cal}$. With the help of the software, it is possible to fit the measured logarithmic or linear IV-curve in order to extract parameters such as R_{series}, R_{shunt}, j_{01} and j_{02} using the two-diode model presented in 2.2.

The so called Multi-light method (MLM) proposed by Fong et al [37] is also using the sun simulator setup in combination with rough filters in order to measure several IV-curves and parameters in dependence of the light intensity. The Multi-light method, as an improvement of the Double-light method proposed by Wolf and Rauschenbach [38], allows to accurately determine the total value of series resistance R_{series} as a function of the voltage with only a small margin of error by varying the illumination intensity in between a range of ± 10 %. For small variations of light intensities, most other characteristics such as the saturation current density j_0 or the diode's ideality factor n can be assumed nearly constant.

Analysing the series resistance for the key voltage points such as MPP and open-circuit voltage can lead to a deeper understanding of the solar cell behaviour and limits. It has been observed, that the measured series resistance is higher for low voltages and decreases from the maximum power point MPP up to V_{oc}.

3.2. Spectral Response

Measuring the spectral response of solar cells gives important insights into solar cell characteristics. The external quantum efficiency EQE, which is in fact the spectral response, gives the ratio of the light-generated charge carriers that are also collected by the junction, as a function of the incident number of photons Φ. Monochromatic light, ranging from 300 nm to 1200 nm is used, since this range represents the utilized part of the sun's spectrum.

$$EQE = \frac{number\,of\,collected\,charge\,carriers}{number\,of\,incident\,photons} = \frac{j_{sc}/q}{\Phi} \tag{3.1}$$

The EQE also contains parasitic absorption e.g. in the anti-reflective coating (ARC). Moreover, it ignores light reflected at the front and rear side. The latter is taken into account by calculating the internal quantum efficiency IQE using the measured reflectance of the solar cell:

$$IQE = \frac{EQE}{(1-R)} \tag{3.2}$$

with R, the total reflectance, composed out of first reflectance and subsequent passing transmittance at the front side (further referred to as front escape), while absorption is not accounted for. The absorption in the case of silicon nitride is considerable for light in the measured wavelength range from 300 nm to 500 nm, but strongly depends on the stoichiometric composition of the silicon nitride layer and therefore its silicon contents [39].
The generation rate, hence absorption of light, is strongly wavelength dependent. Therefore, results of the measured EQE, reflectance and the calculated IQE give information about the spatial quality of the solar cell. While near infrared light penetrates deeper into the cell, which leads to photogeneration closer to the rear side, short wavelengths are mainly absorbed within the first few micrometers. Figure 3.1 shows a typical result of a measured EQE and reflectance curve as well as a calculated IQE.
The used experimental assembly is shown in fiqure 3.2 and is explained in detail and further discussed in [40]. Basically, a tungsten filament lamp generates light, which then passes through a rotating chopper. The chopper modulates the intensity in the shape of a rectangle profile. Thereupon, the light is brought into a grating monochromator, which is selecting a small wavelength interval $\lambda \pm \Delta\lambda$. Furthermore, the ray is then passing through a filter, which avoids the appearance of higher harmonics. A quartz-plate is reflecting a few percentages of light intensity on a reference cell, while the rest is illuminating the solar cell to be measured. Besides the monochromatic illumination, the solar cell is also illuminated with a tungsten halogen lamp (also called bias light) in order to measure the solar cell under illuminated, therefore working conditions. A Lock-in amplifier is able to isolate the signals, since the intensity modulation allows to separate the steady from the varying signal.

In order to determine the IQE, a reflection measurement as a function of the monochromatic light is also needed. This is realized by using an Ulbricht-sphere, which can be brought in the optical path of the bias and monochromatic light. The sphere has small openings on either side

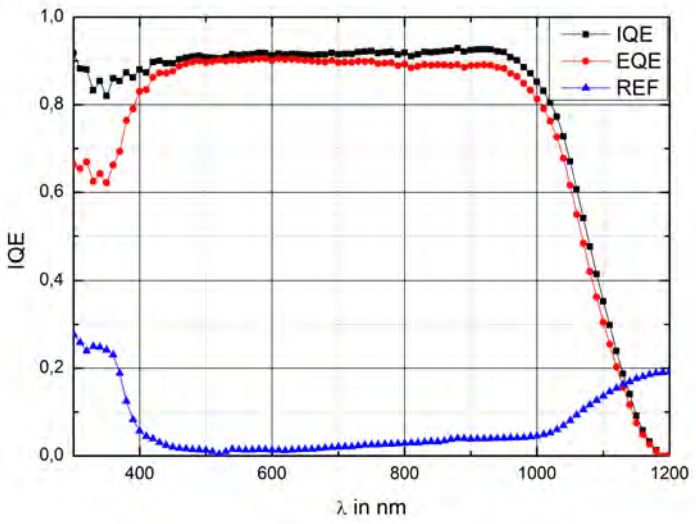

Figure 3.1.: Typical result of an EQE and reflection measurement, extended with a calculated IQE, for a rear junction n-type solar cell; The reflection is measured without the influence of the front side metallization

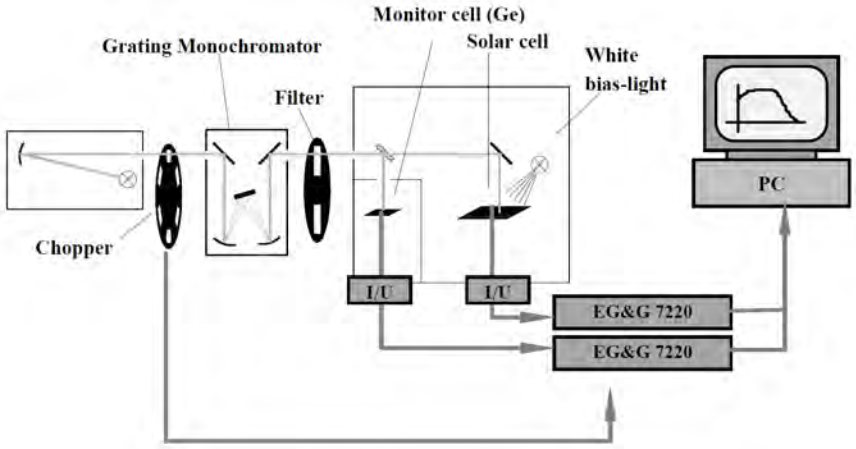

Figure 3.2.: The schematic representation of the Spectral Response setup from [40]

to allow the light to pass through. Inside the sphere, the reflected light from the solar cell is creating a radiation equilibrium, which is then measured by a silicon-germanium detector on one side of the sphere. Usually, the measured area involves a busbar and a cell area which has the same proportion of metallized to non-metallized regions, allowing to assume the same reflectivity for the whole solar cell. Moreover, the IQE of all measured solar cells has been scaled to the short-circuit current density, which was measured using the sun simulator.

While the solar cells within this thesis were measured, the spectral response measurements showed strong problems during calibration of the EQE, especially below 400 nm and above 1150 nm, which are definitely not representing physical behaviour. In some cases, these measured, non-physical data points were therefore removed.

3.3. Photoconductance Decay

Determining the lifetime of test samples in order to identify effective bulk lifetime τ_{eff} and analyse surface passivation quality or implied-V_{oc} is crucial for solar cell improvements.
Measuring the effective lifetime is possible with the transient photo-conductance decay (PCD) as well as the quasi-steady state (QSS) method. Both are different measurement methods of the used experimental assembly. Within this work, a Sinton Lifetime tester WCT-120 as shown in fiqure 3.3 was used. It consists of a flasher **(G)**, which illuminates a sample **(E)** underneath with up to a couple hundred suns intensity, a chuck **(B)** in which a radio frequency bridge **(A)** is inductively coupled to the sample via a coil **(C)**. The coil allows to determine the sheet conductivity of the sample and therefore enables to calculate the excess minority charge carrier concentration. The light intensity can be varied by using filters, of which one is a standard UV-Filter **(F)** and at least one for intensity reduction. It is also necessary to determine the light intensity as a function of time, which is done by a light sensor **(D)**. The experimental assembly is shown in figure 3.3.

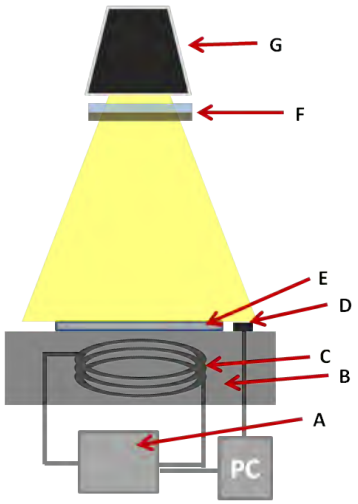

Figure 3.3.: Schematic of the Sinton Lifetime tester with the chuck **(B)**, the high-frequency bridge **(A)**, the coil **(C)**, a light sensor **(D)**, the sample **(E)**, filters **(F)** and the silicon-CCD-camera **(G)**

In order to accurately estimate the lifetime of a sample, the expected lifetime needs to be taken into consideration. While samples with lifetime lower than 200 µs are more accurately measured with the QSS method, whereas samples with higher lifetimes are measured with better accuracies in transient PCD mode.

Quasi-steady state method (QSS) The QSS method, first proposed by Sinton and Cuevas [41], uses a slowly decaying flash of light, allowing to measure the conductivity, from which the excess carrier concentration Δn is then calculated. Recombination and generation rate G are assumed to be in balance, since the light flash source is decaying slowly. Therefore, it is assumed, that the measurement takes place in steady state conditions. As a function of time this allows to analyse several quasi-steady state data points in order to calculate the effective minority charge carrier lifetime τ for many different steady-state conditions via

$$\tau = \frac{\Delta n}{G} \tag{3.3}$$

The generation rate is calculated from the intensity, which enters the cell. Due to this, the reflectivity is important. The reflectivity of the sample is taken into consideration via an optical constant, while the intensity of the flash is determined by a light sensor. The flash needs to decay at least 10 times slower than the recombination of the charge carriers. This limits the QSS method for the used experimental assembly with a decay constant of 2 ms of the light flash to lifetimes lower than 100 µs to 200 µs.

Transient - PCD Higher lifetimes of several miliseconds can be appropriately and accurately measured by using the transient method. A fast decaying light flash (10 - 20 µs is common)

in combination with a slowly decreasing excess carrier concentration Δn in the sample makes it possible to measure the sheet conductivity and hence calculate the average excess carrier density. Then, the minority charge carrier lifetime can be calculated using the derivation of the excess carrier concentration:

$$\tau = -\frac{\Delta n}{\frac{d\Delta n}{dt}} \tag{3.4}$$

Since the light intensity is not taken into consideration, the generation rate is not important for the determination of the lifetime and therefore the error-proneness due to the optical constant is reduced. On the other hand, since the derivative of the excess carrier density is taken, this can sometimes lead to noisy data. The light sensor is only used to identify the end of the flash, when the measurement of the conductivity is triggered.

Generalized method Nagel et al. [42] presented a method, in which both, QSS and PCD can be used simultaneously with the same flashing settings. Starting from the continuity equation 3.5, it can be shown, that both earlier mentioned methods are only limiting cases of the generalized method.

$$\frac{\partial \Delta n}{\partial t} = G - U + \frac{1}{q}\nabla J \tag{3.5}$$

where $U = \frac{\Delta n}{\tau}$ is the recombination rate, q the elementary charge and J the electron current density. Assuming spatial uniform photogeneration and zero surface recombination, no electric field and hence no gradient in current is present. Therefore, the last term of the continuity equation can be assumed to be zero. The lifetime τ is set to be the effective lifetime τ_{eff} and rearranging and using the classical recombination rate shown above, leads to

$$\tau_{eff}(\Delta n) = \frac{\Delta n(t)}{G(t) - \frac{d\Delta n(t)}{dt}} \tag{3.6}$$

This relationship for the effective lifetime shows, that for quasi-steady state conditions (assuming $\frac{d\Delta n}{dt} \approx 0$), equation 3.6 leads to 3.3, whereas for PCD conditions ($G(t) \approx 0$), equation 3.4 follows.

In all measurements involving an intrinsic carrier density, the density is given to 8.6×10^9 cm^{-3} by the analysis program.

3.3.1. Determination of the Saturation Current Density

High-low junctions and highly-doped emitters can be characterized by means of their saturation current density j_0.
For samples with a highly doped surface leading to a high-low or pn-junction as shown in figure 3.4 **(A)** and **(B)**, a relationship for connecting the saturation current density j_0 for both sides with the effective lifetime from [43] is given.

$$\frac{1}{\tau_{eff}} = \frac{1}{\tau_{bulk}} + \frac{j_{0,front}(N_{dop} + \Delta n)}{q n_i^2 W} + \frac{j_{0,rear}(N_{dop} + \Delta n)}{q n_i^2 W} \tag{3.7}$$

where τ_{eff} is the measured effective minority carrier lifetime, N_{dop} the doping concentration, q the elementary charge, n_i the intrinsic carrier concentration at 300 K, τ_{bulk} the lifetime in the bulk (assumed to be very large) and W the thickness of the sample.

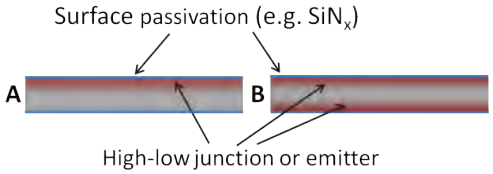

Figure 3.4.: Schematic representation of the sample structure for analysing the saturation current density j_0 with an antisymmetric **(A)** or symmetric high-low junction (emitter) structure **(B)**

3.3.2. Relating the Effective SRV to the Saturation Current Density

From the effective measured lifetime, it is possible to get an estimation of the effective surface recombination velocity. The surface recombination on both, the rear and front side is related to the effective lifetime via (for low S_{eff})

$$\frac{1}{\tau_{eff}} = \frac{1}{\tau_{bulk}} + \frac{S_{front}}{W} + \frac{S_{back}}{W} = \frac{1}{\tau_{bulk}} + \frac{2S_{eff}}{W} \tag{3.8}$$

where W equals the thickness of the sample. This is shortly derivated in [44].
For characterization of samples featuring emitters or high-low junctions, the effective SRV can be related to the saturation current density j_0. Since the emitter is highly doped, minority charge carrier concentration is low, leading to a relatively independent lifetime from the injection level. Moreover, it is assumed that the recombination rate is dominated by Auger recombination which is a good approximation for highly doped regions. This allows to express an emitter recombination current density $j_{e,rec}$ into the emitter [45]

$$j_{e,rec} = j_{oe}\frac{np}{n_i^2} \tag{3.9}$$

where j_{0e} defines the emitter saturation current density and n or p the respective electron or hole concentrations at the base side edge of the space charge region. From here, an effective recombination rate $U_{emitter} = j_{e,rec}/(qW)$ can be given

$$U_{emitter} = j_{0e}\,\frac{np}{qWn_i^2} \tag{3.10}$$

where W is the width of the base region. Using the classical approach for the surface recombination rate presented in equation 2.14 with $S(\Delta n) = S_{eff}$, it follows

$$U_s = S_{eff}\,\Delta n = \frac{j_{e,rec}}{q} = j_{0e}\frac{np}{qn_i^2} \tag{3.11}$$

which then can be rearranged and approximated for n-type silicon to

$$S_{eff} = j_{0e}\frac{N_D + \Delta n}{qn_i^2} \tag{3.12}$$

This is the so called quasi-static emitter approximation. The S_{eff} is the recombination velocity at a virtual surface, where the emitter doping concentration strongly increases.

3.3.3. Implied-V_{oc}

The implied-V_{oc} can be regarded as an upper limit for V_{oc}, if contacts were applied to the sample. The sample structure needs to be prepared like the ones shown in figure 3.4. Therefore, the sample features an emitter, which allows to spatially separate charge carriers. The implied-V_{oc} is calculated via equation

$$V_{oc,\ impl} = \frac{kT}{q}\ ln\left(\frac{\Delta p(N_D + \Delta n)}{n_i^2}\right) \tag{3.13}$$

with $\Delta n = \Delta p$ being the excess charge carrier concentrations of electrons (approximated in high-injection conditions) and holes at the base side edge of the depletion region, respectively. N_D is the base doping and $\frac{kT}{q}$ the thermal voltage [46].
The implied-V_{oc} is measured as a function of the light intensity in suns, while the value for one sun is used. This value is strongly influenced by temperature, the injection level (here one sun) and (entered) base doping (only in low injection conditions).
In general, the obtained implied-V_{oc} values are 10 mV to 20 mV larger than the actual measured V_{oc} for solar cells fabricated in a similar way on the same material and featuring the same passivation. This is due to the applied contacts on the front and rear, which increase the saturation current due to increased recombination at large areas of the surface.

3.4. Photoluminescence and Electroluminescence

Luminescence describes the process of a system losing energy by emission of photons, while going from an excited energy state into a state with lower energy. In this particular case, the electron is 'falling back' into the valence band from the conduction band, called inter-band radiative recombination, which is fairly unusual in silicon, since it is an indirect semiconductor.

Usually, the lifetime of minority charge carriers is limited by the SRH recombination or in highly doped regions by Auger recombination. Both recombination mechanisms are stronger in bad-performing regions. In well-performing regions therefore, the two recombination mechanisms are reduced, which leads to an increased excess charge carrier concentration under steady-state generation. This in turn increases the overall contribution of the radiative recombination to all recombination processes and hence intensifies the intensity emittance, resulting in bright well-performing areas.

Fuyuki et al. [47] showed, that luminescence intensity is linearly correlated to the minority charge carrier diffusion length and hence can be used as a tool to quantitatively and spatially resolve the solar cell's effective minority charge carrier diffusion length and map the lifetime. Therefore, the quality of the base material, hence local recombination centres such as precipitates or bad surface passivation influences can be identified as they limit the diffusion length.

The excess charge carriers can be either generated by means of light (photoluminescence) or by applying an electrical current (electroluminescence).
Photoluminescence (PL) enables to locally-resolve recombination centres and map lifetimes, since it shows increased luminescence in regions with higher excess carrier concentrations. This contactless method is used to determine e.g. bulk minority charge carrier diffusion lengths of passivated wafers within just seconds of exposure and calculation time.

Electroluminescence (EL) on the other hand uses an applied current and voltage at the busbars of the solar cell in order to generate excess minority charge carriers at the pn-junction. Low

excitation currents, which are smaller than the short-circuit current density of the solar cell, can be used to extract the minority charge carrier diffusion length. Moreover, for high excitation currents exceeding j_{sc}, locally varying series resistances lead to local voltage variations, which then in turn create a contrast in the electroluminescence image and can be assigned to a series resistance value by using two differently taken (varied applied current density) images.

3.4.1. Photoluminescence

Light from a light emitting diode (LED) is used to excite charge carriers within a silicon sample. These excited carriers recombine by the in section 2.3 explained recombination mechanisms. Emitted photons from radiative recombination are used to analyse the properties of samples via a capturing silicon-CCD-camera (*Charged-Coupled Device*).
The measured luminescence intensity of the sample I_{lum} is related to the excess carrier concentration Δn according to [48] via:

$$I_{lum}(\Delta n) = B\,\Delta n\,(N_A + \Delta n) \tag{3.14}$$

where B denotes the temperature dependent coefficient for radiative recombination and N_A the density of acceptors. For low-level injection conditions ($\Delta n << N_A$), this relation can be simplified to a linear relationship:

$$I_{lum}(\Delta n) = BN_A\Delta n \tag{3.15}$$

Illumination can be also applied by a Laser from the front side to excite carriers. Within this work, excitation was only done by using the mentioned LEDs, leading to the necessity of a non-metallized rear, since illumination is carried out from that side.
The setup is shown in figure 3.5. A chuck **(A)**, containing about 1800 LEDs **(B1)**, which have a peak wavelength of 633 nm, is covered by a short-pass filter **(C1)**, on which a glass plate is placed. The light is then absorbed in the sample **(E1)**, leading to the generation of excess carriers, which then recombine over the discussed mechanisms, in some cases emitting photons of wavelength corresponding to the gap energy, therefore in the range of 1100 nm. These photons are randomly exiting the wafer in any direction. Photons, which are travelling in the direction of the camera **(G)**, are passing through two filters, one high-pass filter before **(F)** and one after the lens, resulting in a transmittance of only long wavelengths. Therefore, the excitation light of 633 nm is blocked from the detector. The photons are captured by a silicon-CCD-camera **(G)** from the manufacturer Andor Technology with a resolution of 1024 × 1024 pixels. The silicon detector is working under 'deep depletion' conditions, which is sensitive to thermal noise. Therfore, in order to reduce thermal noise, the camera is cooled down to -60 ℃.

3.4.2. Electroluminescence

Electroluminescence is achieved by applying a current and a voltage on the contacts of a solar cell. Similar to the photoluminescence setup, the electroluminescence setup is shown in 3.5.
It consists of a metallic chuck **(A)**, which uses a vacuum to fix the wafer. Current and a voltage contact tip **(C2)** are brought on top of the metallized front side of the silicon wafer **(B2)**. While the current is passing through the sample, a voltage is building up as well. Then, carriers are recombining occasionally by radiative recombination, leading to emission of photons. These photons are passing through a long-wavelength pass filter **(F)** and are then detected in the silicon-CCD-camera **(G)**.

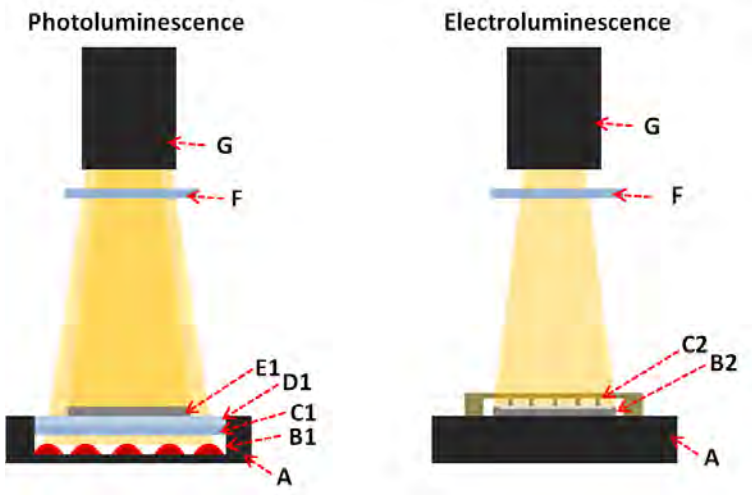

Figure 3.5.: Left: Schematic of the photoluminescence setup with the chuck **(A)**, the LEDs **(B1)**, a short-pass filter **(C1)** and long-wavelength filter **(F)**, the glass plate **(D1)** on which the sample **(E1)** is placed and the silicon-CCD-camera **(G)**; Right: Schematic of the electroluminescence setup with the chuck **(A)**, the current and voltage tips **C2**, the sample **(B2)** on a metallic rear contact, **(F)** the long-wavelength filter and the silicon-CCD-camera **(G)**

The measurement principle is based on the excitation of minority charge carriers by an electrical current, which results in a split-up of the quasi-fermi levels. These quasi-fermi levels are a result of different densities of electrons and holes, that are excited. The difference between both is called the quasi-fermi level split-up and depends on the local voltage over the pn-junction. Furtheremore, this quasi-fermi level split-up has an exponential effect on the spontaneous emission rate of photons from the sample.
Local variations in the voltage over the pn-junction lead to a contrast in the resulting image and since those variations occur from series resistances for high applied current densities, series resistance losses can be identified. High current densities refer to currents higher than short-circuit current density of the solar cell to be measured.
A detailed analysis of the properties of electroluminescence can be found in [49].

It is also possible to spatially resolve the series resistance and dark saturation current density by using the method proposed by Breitenstein [50]. This is done by iteratively calculating the local series resistance as well as saturation current densities from two differently taken electroluminescence images of which one needs to be taken with low excitation current densities, and hence has a marginal series resistance influence.

3.5. Light Beam Induced Current (LBIC)

The light beam induced current method (LBIC) allows to spatially resolve the local external quantum efficiency (EQE) of finished solar cells by illuminating the cell with a defined monochromatic laser beam from one or up to four different laser diodes. The laser beam is led through a glass fibre, which is followed by an optical setup, both together defining a laser spot of about 10 µm in diameter at full width half maximum (Gaussian beam profile). In this particular setup, wavelengths of 635 nm, 833 nm, 910 nm and 980 nm are available, resulting

in penetration depths of 3 µm, 10 µm, 30 µm, 100 µm, respectively. The penetration depth refers to the depth, where only 1/e of the incident intensity remains. The EQE is calculated from a measured j_{sc}, which is very small and hence needs to be separated from other influences. The signal is therefore passing through a Lock-in amplifier. During measurement, the solar cell to be measured is placed on an x-y stage, which allows mapping of whole cells. From the measured j_{sc}, it is possible to determine the EQE of a solar cell via equation 3.1. Therefore, compared to the spectral response measurement, this method allows to locally determine the EQE and hence can be used to identify well and bad performing regions, too. Furthermore, similar to the wavelength dependences used in spectral response measurements to determine lateral conditions (e.g. short wavelengths describe behaviour of the front side rather than the rear side), LBIC measurements allow to analyse these conditions locally either by means of a line scan or a mapped area.

4. n-Type Rear Al-Emitter Solar Cell Concepts

Most commercially available mono-crystalline silicon solar cells feature a boron doped base with common bulk resistances of 2 to 6 Ωcm. Within this work, mono-crystalline silicon solar cells were fabricated from n-type Czochralski (Cz) grown material. Phosphorus doped silicon features several advantages compared to boron doped p-type silicon. High oxygen contents within most Cz-grown boron-doped silicon materials result in light-induced degradation, reducing the effective lifetime due to the formation of recombination active B-O complexes [4, 5, 6] under illumination. Moreover, the effectiveness of most metal impurities to function as recombination centers within the n-type material is reduced, since the capture cross section for electrons is much larger than the one for holes. Therefore, minority charge carrier lifetime of holes is not as severely affected by metal impurities as it would be in p-type silicon for electrons [7]. This results in a high minority charge carrier lifetime in the bulk from which a high diffusion length follows.

Three different cell concepts are described. First, the reference and origin of all presented cell concepts, the improved PhosTop cell is discussed in detail with its processing sequence as it is processed at the University of Konstanz. Starting from the improved PhosTop cell's front side, the rear side is changed resulting in the Aluminium - locally alloyed rear emitter (Al-LARE) solar cell or the full area locally contacted rear emitter (FALCON) solar cell. Simulations are carried out in order to gain insights in their potential and limitations. The simulation programs are introduced in section 4.2.1.

4.1. The PhosTop Solar Cell

The PhosTop cell concept was first proposed by D. L. Meier et al. [54]. It represents the basic structure for this work, from which modifications have been made in order to improve the rear side performance. The originally proposed PhosTop cell features a homogeneous front surface field (approx. 40 Ω/sq) with a negatively doped bulk (20 Ωcm) as well as a fully aluminium alloyed rear emitter. The FSF is reducing the concentration of minority carriers close to the surface, thereby achieving a low effective SRV.

The PhosTop cell concept was improved by replacing the homogeneously diffused FSF by a selective FSF. This means, that the front phosphorous concentration is varied in order to be able to reduce minority charge carrier concentrations close to the surface and furthermore the contact resistance to the front metallization as well as recombination in the highly doped region. The solar cell concept is shown in figure 4.1. Within this work and earlier published by Book et al. [9] efficiencies of 19.4 % have been achieved, while only industrial screen-printing techniques were applied. In June 2012, Suntech published a similarly fabricated improved PhosTop cell that showed an efficiency of 19.8 % [55], while the front side contact was plated and not screen-printed. This is to the knowledge of the author the world record for this cell concept. The improved PhosTop solar cell presented by Book et al., which is referred to as the PhosTop cell or the improved PhosTop cell in this work, is used as the reference.

Since the junction is on the rear side and therefore the diffusion length needs to exceed several wafer thicknesses in order to allow a high quantum efficiency, a very well passivated surface and an optimized FSF is necessary. Therefore, the front surface recombination velocity (SRV) is an important factor, determining whether or not the solar cell is performing well. The front SRV can be reduced as described in section 2.5, either by means of chemical passivation, field-effect passivation or a high-low junction. The improved PhosTop cell concept features besides enhanced surface passivation, a s-FSF, which effectively shields holes from the front surface. Furthermore, since the doping concentration is high underneath the front finger, the contact resistance is reduced. Therefore, the contribution of the contact resistance to the cumulative series resistance is decreased.

Between the fingers, therefore in the illuminated region, a lower doping is preferred in order to reduce the loss of generated carriers close to the surface by means of Auger and SRH recombination, while both are increased in highly doped regions. This effect is referred to as 'blue-response', because high energy photons are the first to be absorbed. In comparison to p-type silicon solar cells, where the selective emitter (same as the s-FSF) only improves the IQE for short wavelengths, for n-type rear junction solar cells the IQE over the whole spectrum (below 1000 nm) is improved. The improved response for n-type silicon solar cells can be seen in an improvement for wavelengths below 1000 nm, if a homogeneously FSF PhosTop cell is compared with a selective FSF improved PhosTop cell.

For n-type solar cells featuring a FSF, the lateral conductivity to the contact is not only provided by the FSF, but also by a contribution of the base, since both have the same polarity. This reduces the share of the lateral resistance to the series resistance. The effective sheet resistance reduction is depending on the sheet resistance of the FSF, the base doping and the injection level since the base is in high-injection conditions under one sun illumination. Further details are given in section 4.1.1. A 'trade-off' between high blue-response and increased effective sheet resistance must be made in the illuminated area. Book et al. [8, 56] found, that an optimal sheet resistance of approx. 100 Ω/sq fits best for the illuminated region.

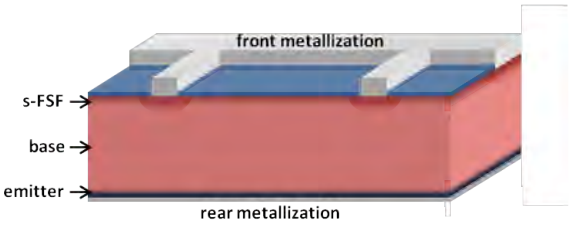

Figure 4.1.: Schematic representation of the improved PhosTop solar cell concept

The aluminium-alloyed emitter, as described in section 2.7, is created by co-firing of the screen-printed aluminium paste. This results in an emitter underneath the eutectic, which is usually around 5 to 8 µm thick and has a concentration at the junction of 1.5-2×10^{19} cm^{-3} (for a aluminium paste that includes boron). Overall, this leads to a sheet resistance of approx. 10-11 Ω/sq.

4.1.1. Influence of the Base Doping

The base doping is a crucial factor for solar cell performance. In cases, where solar cell performance is enhanced by means of an FSF, the doping difference of the FSF and base is important to consider for the effectiveness of the high-low junction and therefore the effective SRV. Book et al. [9] have shown in a simulation, that under j_{sc} conditions the hole concentration close to the surface is increased for low ohmic material (2 Ωcm) compared to high ohmic material (16 Ωcm). Therefore, the effective SRV (S_{eff}) is increased since the high-low junction effectiveness is reduced due to higher base doping while the SRV (S) stays constant. This results in increased recombination losses and hence j_{sc} is reduced. The effect on V_{oc} is marginal, since the same simulation for V_{oc} conditions has shown almost equal hole concentrations for both resistivities and hence j_{01} is constant. Moreover, the effect of the different bulk resistivities on the effective sheet resistances has been analysed by Book et al. [9, 56]. Since the base has the same polarity as the FSF, it contributes to the lateral conductivity of electrons. This results in a base doping, injection level and voltage dependence of the effective sheet resistance in the FSF, while the latter two are also depending upon each other. Under V_{MPP} conditions, the effective sheet resistance is reduced. From 2 Ωcm to 16 Ωcm bulk resistivity, the contribution of the bulk to the effective sheet resistance is reduced and hence, the effective sheet resistance increases.

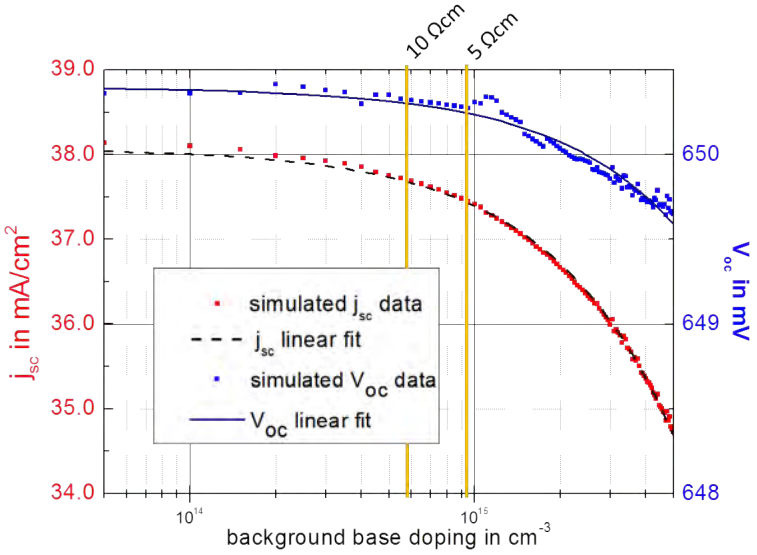

Figure 4.2.: Linear fit of the simulated influence of the background base doping on the short-circuit current density and open-circuit voltage with simulated data points

In figure 4.2, the base doping concentration is varied from 10^{14} cm^{-3} up to 5×10^{15} cm^{-3}, which equals a resistivity of 44.5 Ωcm down to about 1 Ωcm, respectively. This is done for a PhosTop cell by using PC1D, assuming a homogeneous etch-back FSF. Details on the used parameters are found in appendix A.

The simulation shows a strong effect on j_{sc}. While for lightly doped bases, j_{sc} can reach over 38 mA/cm^2, the higher the doping the lower the effectiveness of the high-low junction on the front becomes and as a result a reduction in j_{sc} takes place. On the other hand, V_{oc} declines only marginally for increased base doping level.

4.1.2. Process Sequence

Within this work, improved PhosTop solar cells are used as reference cells. Even more, the front side of the improved PhosTop cell concept is kept unchanged. On the rear side further improvements have been made in order to enhance the quantum efficiency as well as the open-circuit voltage. The direct comparison with the improved PhosTop cell allows to evaluate only enhancements resulting of the improved rear side properties. The process sequence as it is shown in figure 4.3 is discussed in detail, since these processing steps have been done generally for all fabricated solar cells.

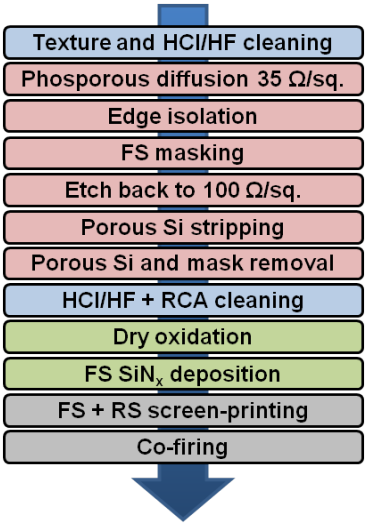

Figure 4.3.: PhosTop cell process sequence

Texture All wafers used to fabricate solar cells within this work are textured externally. An alkaline solution is used in order to obtain a randomized pyramidal structure on both surfaces with pyramids up to 10 µm height.

HCl/HF cleaning sequence A standard HCl/HF cleaning sequence involves successive steps. At first, the wafers are brought into a DI-H_2O bath, which is followed by a 10 min step in a 2 to 3 % solution of HCl. After that, another DI-H_2O rinsing step and a HF bathing step in a 2 % solution is carried out to remove the previously grown oxide from the surface. The wafers are usually held inside the HF solution, until they are hydrophobic.

Phosphorous diffusion A phosphourus diffusion is carried out in a Centrotherm E1200-HT 300 furnace, leading to a sheet resistance on both surfaces of the wafer of 35 Ω/sq. Basically, a liquid source of phosphorous ($POCl_3$) in a so called bubbler is interspersed by gaseous nitrogen, which carries the $POCl_3$ to the wafers. Three different reactions take place, resulting in the thin layer of phosphorous and silicon dioxide, the so called phosphorous silicate glass (PSG). The whole process consists of a heating up procedure, which is followed by a growing step of the PSG. Then, a 'drive-in' step takes place. Typical peak temperatures for a phosphorous diffusion are around 840 °C.

Edge isolation The edge isolation, more precisely removing the phosphorus diffusion on the rear, is done by single side etching (SSE) and is needed in order to avoid shunting. The wafers are brought into an acidic solution consisting of HNO_3 and HF after a previous cleaning sequence.

Masking A Schmid Inkjet DoD 300 is used in order to bring a protective wax on the surface of the wafer. This wax is printed on top of the regions, where the busbars and fingers are situated later on and hence allows to locally etch back the wafers surface.

Etch back and stripping The s-FSF formation is prepared by the earlier described masking. Then, an acidic solution consisting of nitric acid (HNO_3), fluoric acid (HF) and deionized water (DI-water) is used to create porous silicon in the non-covered area [19].

The etch back of the non-masked regions is done until a sheet resistance of around 100 Ω/sq is obtained. The etch back depth can be estimated by the thin porous layer of silicon,

that is remaining on the surface. Incident light is interfering and shows a characteristic color depending on the porous layer thickness. The porous silicon is then removed in an alkaline solution of potassium hydroxide (KOH), DI-water and an alcohol. This is usually carried out in an ultrasonic bath in order to remove the wax.

RCA cleaning Oxidizing the surface of silicon wafers and subsequently removing the oxidized layer is the main idea of RCA cleaning. The fabricated oxide consists of impurities of metal or organic origin and is removed in an acidic solution. Therefore, RCA cleaning is an enhanced method to reduce contamination close and on the surface of semiconductors [15, 57]. Standard RCA cleaning consists of several cleaning steps. First, the wafers are brought into a solution consisting of ammonia NH_3, hydrogen peroxide H_2O_2 and de-ionized water with a mixture of 1:1:5 at 80 °C. After 10 minutes, the wafers are flushed in water, which is then followed by a dipping step in a 2 % HF solution. Once the wafers are hydrophobic, the carriers are further passing through a second cleaning solution, that consists of de-ionized water, hydrochloric acid (HCl) and hydrogen peroxide (mixture 8:1:1). The oxidation, which takes place in this solution, is then removed in a second HF-bath. Depending on the following process, the last two steps are repeated.

Dry oxidation The dry oxidation is carried out in a Centrotherm E1200-HT 300 quartz furnace at 900 °C. Since silicon oxide growth speed depends on the underlying doping concentration of the wafer, layer thickness varies over the cell. Details about the oxidation are found in 2.6.1. Dry oxidation usually involves a heating up step of about 20 minutes, a temperature stabilisation phase which is followed by a varied exposure time to ultra pure oxygen and a cooling down procedure of approx. 30 minutes.

Front side silicon nitride deposition The ARC is usually brought onto the wafer by direct-plasma enhanced chemical vapour deposition (direct PECVD), where the deposited layer is referred to as CT-SiN_x. The typical thickness of about 75 nm is optimised for optimum AM 1.5G solar spectrum coupling of light. In the case of a stack system, e.g. a thin (5 - 10 nm) silicon oxide layer, the thickness of the SiN_x is adapted. Typical refractive indices are about 2.05.

Front and rear side screen-printing Up to this processing step, all wafers fabricated within this work to become solar cells have been treated the same, with some exceptions for the deposition method of the silicon nitride, which in some cases was also deposited by means of remote PECVD deposition (SiNA-SiN_x). From now on, the following process sequence is only carried out for PhosTop cells, while other cell designs need further additional steps.

The front and rear metallization is brought onto the wafer by screen-printing using commercially available silver and aluminium paste, respectively. On the front side a silver grid is screen-printed on the region, where the high doping of the s-FSF is present. On the rear side, the wafer is fully covered with aluminium paste.

Co-firing Co-firing of the solar cell leads to the formation of the emitter as described in section 2.7. Since the used silver paste is consisting of a glass frit, it etches itself through the thin front passivation and is contacting the n^{++} region of the s-FSF. Typical parameters are a set peak temperature of 860 °C and a chain speed of 5400 mm/min.

4.2. Aluminium-Locally Alloyed Rear Emitter (Al-LARE) Solar Cell

Aluminium-locally alloyed rear emitter solar cells (Al-LARE solar cells) are the basic idea behind this diploma thesis. The Al-LARE solar cell concept, an advancement of the improved PhosTop cell concept, features a full dielectric rear passivation, which is locally opened. From experience with PERC solar cells (*P*assivated *E*mitter *R*ear *C*ontact), line openings allow industrial-related process sequences and are therefore used [58, 59]. The front side is kept unchanged from the improved PhosTop cell concept and hence features a selective FSF as well as a SiO_2/SiN_x passivation stack. The cell concept is depicted in figure 4.4 and could be used as a bifacial solar cell as well, if on the rear side, a aluminium paste is locally screen-printed and alloyed. In this work, only full area screen-printing on the rear was done and therefore, no bifacial solar cells were fabricated.

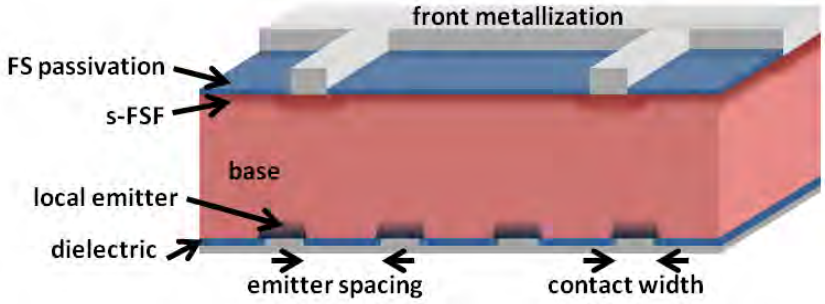

Figure 4.4.: Schematic of the Al - locally alloyed rear emitter (Al-LARE) cell design

There are basically two reasons for a dielectric rear passiation. Depending on the rear surface passivation quality, the resulting saturation current density j_{01} can be reduced compared to a full rear metallization. The first diode's saturation current density is composed of

$$j_{01} = j_{0,rear} + j_{0,b} + j_{0,FSF} \tag{4.1}$$

where $j_{0,rear} = j_{0e}$ is the emitter saturation current density, $j_{0,b}$ the contribution of the bulk and $j_{0,FSF}$ the influence of the FSF on the overall j_{01}. While the emitter area is reduced, it can be assumed that $j_{0,rear}$ is composed of

$$j_{0,rear} = x\ j_{0e} + (1-x)\ j_{0,pass} \tag{4.2}$$

where x represents the emitter fraction of the total cell rear surface. This assumes a linearly dependence of $j_{0,rear}$ on the emitter fraction, which in turn leads to a linear relationship for V_{oc}. This has been confirmed by a simulation. A good surface passivation leads to a low $j_{0,pass}$ and hence can reduce the overall j_{01}. This can then result in an increase of the open-circuit voltage via equation 2.2.

The use of a passivation layer, which covers the rear surface where no emitter has been formed, can lead to an improved internal reflection, since dielectric passivation has a higher reflectance than screen-printed aluminium paste or the formed eutectic. While it can be assumed, that the passivated area reflects about 95 % of the incident light, the metallized region reflects around 70 %. An enhanced internal reflection leads to a gain in the short-circuit current density j_{sc},

since more long-wavelength photons are able to be absorbed in the silicon. The thickness of the rear passivation layer can further be optimized to increase reflectance especially in the long wavelength region.
A typical characterization method to analyse the changes due to an enhanced internal reflection is the spectral response measurement. For high rear internal reflectance, the EQE and IQE in the long wavelength regime is increased compared to a full metallized rear. Furthermore, the measured reflectance curve shows higher reflectance for dielectric rear passivation in the long wavelengths, as well. A simulation of this gain in internal reflection as a fraction of the local emitter spacing and hence the emitter coverage is shown in section 4.2.2.

The effect of the second diode's saturation current density j_{02} was analysed for the best results from the emitter pitch simulation. This is done, because in this work, the recombination in the emitter or recombination at the edge of the pn-junction [60] was found to limit the presented cell concept.

4.2.1. Basic Notes on Simulation

Two-dimensional simulation is used to identify the potential and limitations of the presented solar cell concepts. Within this work, PC1D [61] and PC2D [62] are used separately for different purposes. PC1D, a one-dimensional solar cell simulation program, is widely known and accepted. It was used for analysing solar cells, which are sufficiently simulated neglecting two-dimensional effects such as lateral currents and series resistances. PC2D, which is based on PC1D, on the other hand is able to simulate solar cells with two-dimensional dependences. Examples for these besides the ones presented in this thesis are PERC solar cells, selective emitter cells or even interdigitated back contact (IBC) solar cells.

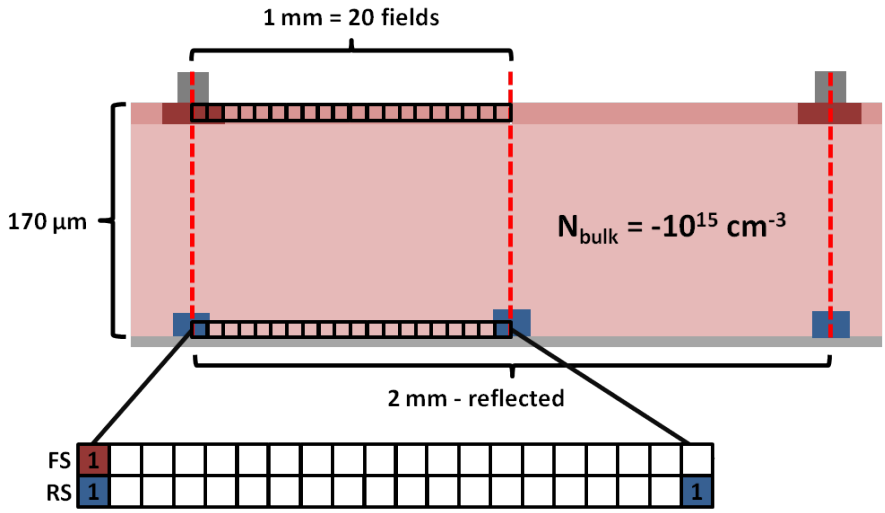

Figure 4.5.: Schematic representation of an Al-LARE solar cell as well as its simulated design for 1 mm rear finger pitch (10% emitter coverage)

Due to limitations of the Mircosoft Excel spreadsheet based PC2D, only a base resistance of 4.5 Ωcm was applicable. Higher base resistances have led to convergence errors. Therefore, a comparison between a 4.5 Ωcm and 10 Ωcm simplified PhosTop-cell is carried out in 4.1.1 using PC1D. Furthermore, PC2D is limited by the way it is constructed: consisting of twenty lateral

elements on each surface, which can be either repeated or reflected, the element size is limited in favour to the front grid design. As shown in figure 4.5, for a specific front grid pitch of 2 mm (from one middle to the other middle of the next front finger), only several discrete pitches on the rear are possible in order to keep the cell design symmetric.

Besides defining contact area as seen in the figure by setting specific elements to 1, PC2D allows to specify sheet resistances, j_{01} and j_{02} values as well as specific optical properties such as reflection and transmittance for all 20 elements on either cell side.

The simulation in figure 4.2 shows a difference in the short-circuit current density of about 0.38 mA/cm^2 between 4.5 Ωcm and 10 Ωcm, while the difference in the open-circuit voltage remains marginal. The reduction of j_{sc} can be explained by the reduced high-low junction effectiveness between a highly doped base and the FSF. This is one reason, why a short-circuit current density difference in fabricated compared to simulated cells is found.

4.2.2. Emitter Pitch

The emitter pitch and hence the contact pitch was varied by successively adding emitter and contact area to the rear side. The front contact pitch was held constant at 2 mm, with a finger width of 100 µm. This led to a slighly higher front surface metallization than the fabricated solar cells. The busbar was taken into account by setting the total transmission of light on the front side to 97.5%, while the shading of the fingers is accounted for by PC2D by locally setting the transmittance at the front position of the fingers to zero.
Al-LARE solar cells were simulated with emitter spacings from 1900 µm (5 %), 900 µm (10 %), 400 µm (20 %), 300 µm (25 %), 150 µm (40 %), down to 100 µm (50 %) with their respective emitter coverage. The emitter width was held constant at 100 µm. Furthermore, the internal reflection on the rear was set to be 95 % for the passivated area for both, specular and diffuse light, while for rear metallization these values were chosen to 75 % and 70 %, respectively. A detailed overview of used parameters can be found in appendix B.

Three simulation sets were carried out with the above mentioned pitches and emitter widths by varying the respective saturation current density $j_{0,pass}$ with values of 15, 50 and 150 fA/cm^2. The respective effective rear SRV is ranging from 0.9 cm/s over 3.1 cm/s to 9.3 cm/s. For low-level injection conditions (hence $\Delta n << N_{D,A}$), the following relationship between the effective SRV and saturation current density is valid [43]:

$$S_{eff} \approx j_0 \frac{N_A}{q n_i^2}$$

where N_A equals the acceptor concentration (in this case the donator concentrations), q the elementary charge and n_i the intrinsic carrier concentration, which is assumed to be 10^{10} cm^{-3}. The results are shown in figure 4.6.
While for the used PhosTop reference cell a second diode's saturation current density j_{02} of 2×10^{-8} mA/cm^2 was used, with consideration to the experiments, which showed higher values for Al-LARE solar cells, $j_{02} = 2.4\times10^{-8}$ mA/cm^2 was assumed. Moreover, the solar cell featuring an emitter pitch of 1900 µm was simulated for a total width of the cell structure of 2 mm, which was repeated afterwards. All other solar cells were simulated using a reflected 1 mm region, therefore with an element size of 50 µm.

The simulation shows an increase in the open-circuit voltage with an enlargement of the emitter spacing. This is due to the fact, that the passivation results in a lower overall saturation

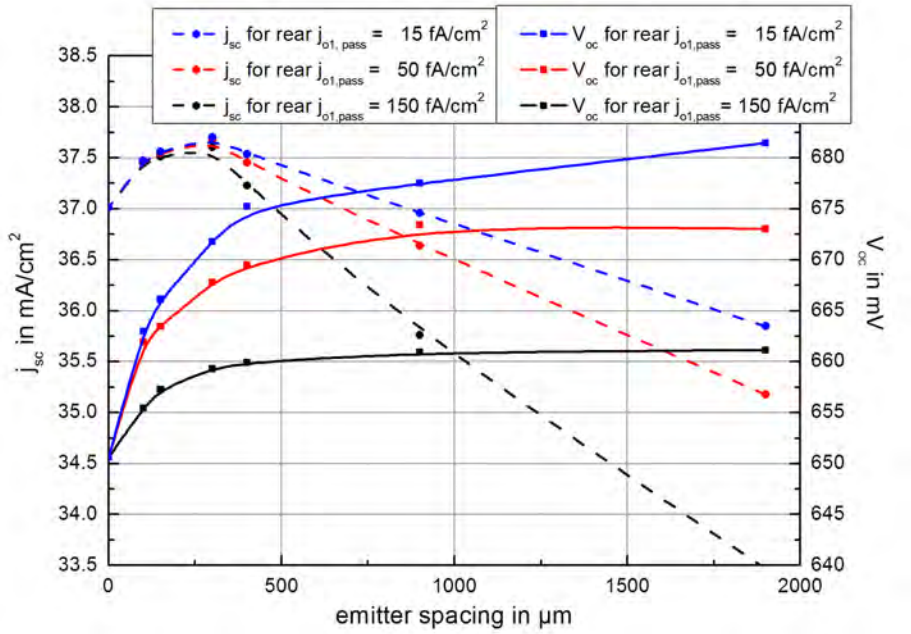

Figure 4.6.: Simulation of the locally contacted and formed emitter cell for different pitches with three different $j_{01,pass}$; Note: Lines are a guide to the eye.

current density j_{01} (see equation 4.2) and hence via equation 2.2 in an enhancement of V_{oc}. For reduced $j_{01,pass}$, the increase is even more pronounced and is becoming more dominant for increased pitches. As mentioned before, the j_{01} composition is showing a linear dependence on the passivated to metallized area ratio.

The short-circuit current density increases with an increased pitch until it peaks at 300 µm. Then it declines continuously, with a negative slope depending on the surface passivation quality. The higher the SRV, the more current is lost due to recombination at the passivated rear surface. Furthermore, the effect of the SRV on the j_{sc} shows only a small influence on the optimal emitter spacings. Therefore an optimum of the emitter pitch, emitter coverage and SRV can be found, where the latter two should be as small as possible.

Figure 4.7 shows the simulated efficiency as a function of the emitter pitches as well as a simulated EQE curve. While for high SRVs, the current loss seems to have a huge impact on the efficiency, the peak level for each curve further seems to be at the same pitch of 300 µm. Although the peak is increased with improved passivation quality, it is less pronounced the higher the passivation quality gets and further, the slope is reduced.

Simulation results for the EQE are shown in figure 4.7 on the right side for several pitches and a rear side passviation quality between the emitters of 50 fA/cm^2.

The simulated EQE shows two pronounced effects: First, the overall level in the main part of the spectrum consisting of wavelengths up to 1000 nm, is reduced for large pitches. This indicates a collection loss of generated carriers by the locally formed emitter for emitter spacings larger than 400 µm. This effect is visible until a pitch of roughly 400 µm. Second, the short-circuit current density gain as a result of increased emitter spacings and hence from increased internal rear reflection can be seen in the near infra-red range. The EQE therefore increases

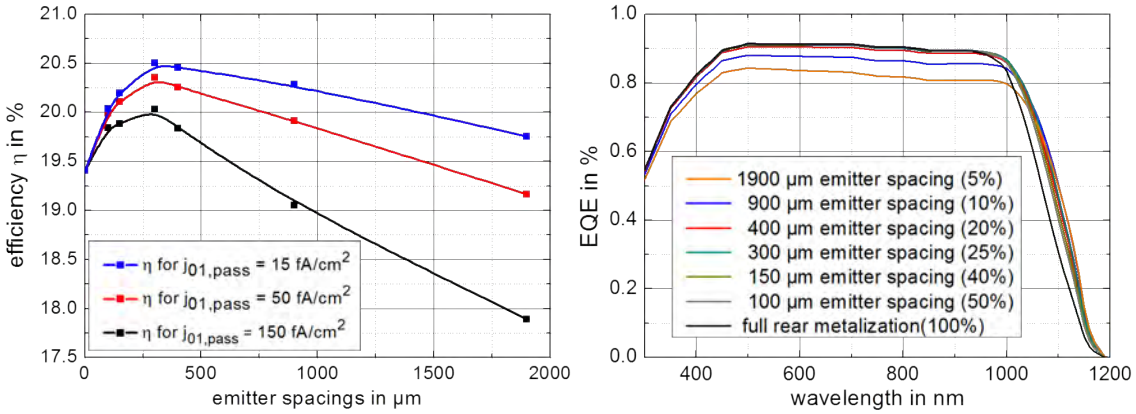

Figure 4.7.: Left side: Simulated efficiency; Right side: Simulated EQE of the presented cell concept with a rear passivation quality of 50 fA/cm^2 ; Note: Lines are a guide to the eye.

with decreasing emitter area in the near infrared.

4.2.3. Effect of an Increased j_{02} on the Performance of Al-LARE Solar Cells

The best performing solar cell from the first simulation 4.2.2 with a pitch of 300 µm is utilized in order to estimate the effect of increased space charge region recombination and edge recombination, which has been modelled by successively scaling the value of j_{02} from 1.5×10^{-8} A/cm^2 up to 200×10^{-8} A/cm^2. The resulting curve is shown in figure 4.8 and should follow the two-diode model.

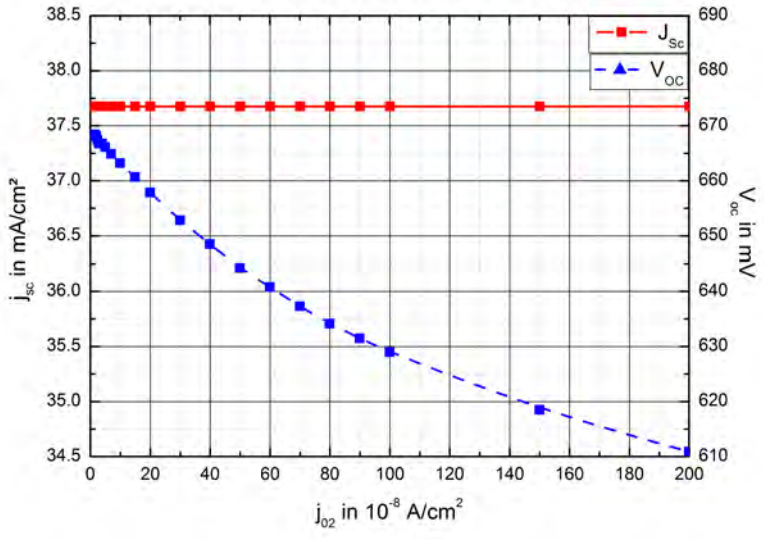

Figure 4.8.: Simulation of the emitter recombination by variation of j_{02} for a constant pitch of a locally contacted and formed emitter cell with 300 µm pitch; Note: lines are guide to the eye.

As expected from the two-diode model, the short-circuit current density j_{sc} is not affected by

the increased space charge region recombination and stays constant. On the other hand, the open-circuit voltage V_{oc} is reduced, since it depends on the quasi-fermi levels, which are in turn affected by the carrier densities in the junction. While the carrier density is affected by recombination in the junction, V_{oc} is reduced.

4.3. Full Area Locally Contacted Emitter (FALCON) Solar Cell

Besides locally formed emitter (Al-LARE) solar cells, also full area locally contacted rear emitter (FALCON) solar cells were fabricated.

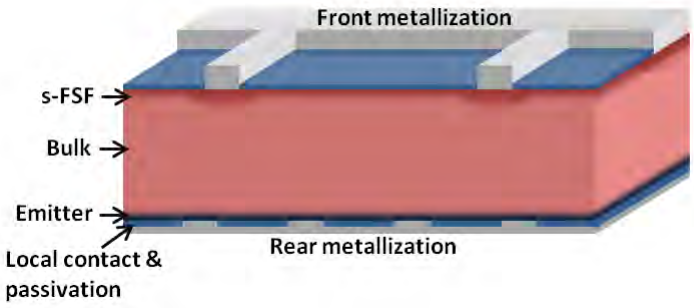

Figure 4.9.: Schematic of a locally contacted full rear emitter solar cell

This cell concept is depicted in figure 4.9 and is similar to the previous one, but features a full area rear emitter which is etched back to a specified emitter depth. Similarly to the locally formed emitter cell, this cell concept also features an enhanced internal rear reflection due to the dielectric rear passivation, which results in an increase in the short-circuit current. Furthermore, the rear side emitter passivation reduces the overall rear diode's saturation current j_{01} and hence should enable to achieve a higher V_{oc} compared to the improved PhosTop cell. Depending on the metallization, this cell concept can be used as a bifacial solar cells, as well. If a grid is used for screen-printing aluminium paste or silver-aluminium paste on the rear, locally passivated regions remain non-metallized and hence can couple light inside the cell.

4.3.1. Contact Pitch

Similar to the locally formed and contacted emitter cells, locally contacted cells are simulated using PC2D. The pitch has been varied, while front side metallization is held constant at a 2 mm pitch. The short-circuit current j_{sc} and the open-circuit voltage V_{oc} have been simulated for two different saturation currents j_{01} at the rear passivated area, 50 fA/cm^2 and 150 fA/cm^2. The emitter is treated as it has been etched back to roughly 2 µm, therefore having a sheet resistance of 50 Ω/sq.
While j_{sc} is not influenced by the passivation quality between the contacts on the rear, V_{oc} is improving. The short-circuit current is increased with enlarged pitch due to the enhanced internal reflection by the passivated rear emitter between the contacts to the emitter.
Compared to the locally formed emitter, a full rear emitter eliminates the loss due to lateral diffusion, since in between the contacts, the holes are majority charge carriers and hence are less likely to recombine.

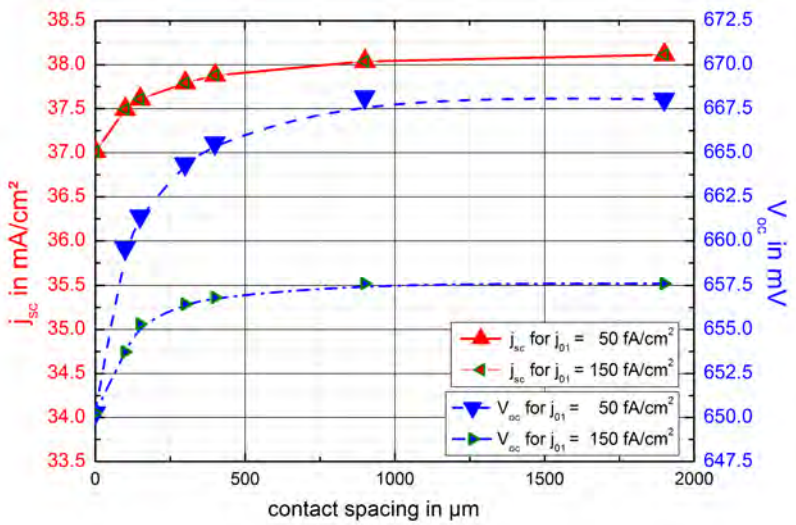

Figure 4.10.: Locally contacted full area rear emitter solar cell simulation for two different rear emitter saturation current densities (50 fA/cm^2 and 150 fA/cm^2)

4.3.2. Emitter Depth

By bringing the junction closer to the surface, recombination losses in the highly doped emitter are reduced, since the minority charge carrier lifetime is extremely low, only in the range of a few nanoseconds [63, 64]. If the junction is able to collect more generated minority carriers in the emitter, j_{sc} is increased. On the other hand, this should lead to a higher sensitivity to the surface passivation quality. Simulations using PC1D were carried out for 10 Ωcm bulk resistivity with a bulk lifetime of 10 ms. The open-circuit voltage, the short-circuit current as well as the efficiency are presented in figure 4.11 as a function of the rear surface recombination velocity.

The basis of the simulation was a PhosTop cell, which was simulated with a measured front side reflection spectrum as well as a FSF doping profile measured using an electrochemical capacitance-voltage (ECV) measurement assembly (both have been measured in a previous experiment, which is not part of this work). Details about this simulation are shown in appendix D. Since PC2D was not applicable, because no emitter or FSF profiles can be imported, one-dimensional simulation was used. It is important to note, that neither optical gain nor series resistance losses such as in the first case nor a j_{sc} gain due to enhanced internal reflection or in the latter case a lateral resistances in the highly doped emitter are included in the simulation. The open-circuit voltage dependence on the SRV increases the more the pn-junction gets closer to the surface. While this can improve the V_{oc} for a low rear SRV, it deteriorates V_{oc} for high SRV, starting roughly above 10^4 cm/s. This is a result of a reduced field-effect passivation of the emitter due to the doping profile. Therefore, far etched back emitters are much more sensible to the actual rear SRV, if the surface is passivated compared to less etched back emitters (not S_{eff}, which is reduced).
The short-circuit current density j_{sc} is affected by the junction depth, since the minority charge carrier lifetime and hence the effective diffusion length in the emitter is low, the distance from the junction is important. This results in a potential gain from a 8 µm deep junction to 0.5 µm of about 0.43 mA/cm^2. Moreover, the short-circuit current density is only marginal influenced

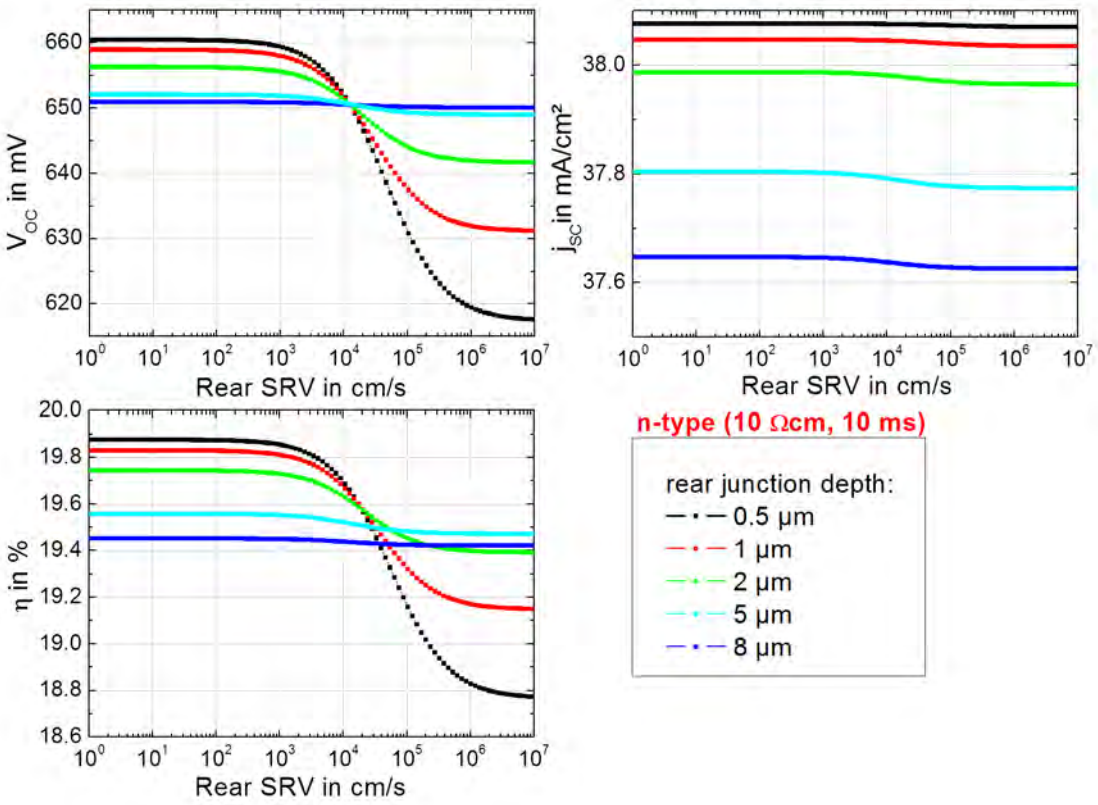

Figure 4.11.: Simulation of j_{sc}, V_{oc} and η as a function of the rear SRV for different emitter depths

by the SRV.

Overall, this results in a enhanced efficiency for a low SRV and far etched back emitter, compared to the standard roughly 5 µm deep PhosTop emitter. For less etched back emitters the efficiency is determined by the loss of the open-circuit voltage and hence deteriorates for increased SRV. Interestingly, the improved PhosTop cell with an unpassivated rear ($S = 10^7$ cm/s) and an emitter depth of 5 µm shows the highest efficiency for the respective SRV, which is also only marginally affected by the SRV, too. The reason for this is the behaviour of j_{sc} and V_{oc}. While j_{sc} varies only marginally due to the SRV, V_{oc} is strongly influenced.

5. Experiments and Methodology

The main goal of this thesis is to use the already well-performing front side of the PhosTop solar cell concept, which includes a s-FSF and a SiO_2/CT-SiN_x stack, and improve the rear side by means of a dielectric passivation.

Basically, three different solar cell concepts based on n-type mono-crystalline silicon are realized, which are prepared by preparatory experiments. These experiments are focused on evaluating the rear side passivation quality of different passivation layers and stacks on two differently doped silicon surfaces. That involves the passivation of n-type bulk substrates (10-12 Ωcm) and highly-doped p^{++} layers (11-13 Ω/sq). To complete, the emitter formation and quality is analysed.

Then, the Aluminium-locally alloyed rear emitter (Al-LARE) solar cell, which uses the PhosTop cell as reference, is presented. Starting with an emitter spacing analysis in order to find the optimum rear side geometry, results of fabricated 6" Al-LARE solar cells are given and furthermore, analysed and discussed.

Finally, FALCON solar cells are presented, which feature a full rear emitter that is locally contacted. Results of fabricated FALCON solar cells are given and further analysed.

5.1. n-Type Base Passivation: Firing Stability and Passivation Quality

The earlier presented Al-LARE solar cell features a rear n-type passivated surface. Therefore, the optimum choice for archiving low surface recombination velocities and hence high lifetimes, needs to be made. Moreover, during fabrication of the Al-LARE solar cell, a full rear screen-printing of a fritted aluminium paste is carried out, which can lead to a degradation of the passivation quality. Both are analysed in the first experiment in section 5.1.1. In this experiment, the obtained lifetimes were low, which made it necessary to repeat the passivation quality analysis. The repeated passivation quality evaluation is presented in section 5.1.2.

5.1.1. Passivation Quality and Stability Investigation

The stability and quality of the passivation layers and stacks are analysed in order to decide, whether the locally opened passivation can be covered by a full aluminium rear contact or needs to be contacted locally and furthermore, which passivation layer/stack is performing best. The first is important in order to avoid degradation of the underlying passivation stack/layer by an industrial-like fabrication of Al-LARE solar cells, which includes full rear metallization. The stability against co-firing of aluminium paste is therefore investigated by comparing metallized and non-metallized samples by means of their measured effective minority charge carrier lifetime (further referred to as lifetime) by using the photoconductance decay measurement assembly, which is explained in section 3.3. This experiment was originally planned to allow the evaluation of the passivation quality as well, but since the measured lifetimes are unexpectedly low for

certain layers/stacks, the quality of the passivation layers and stacks is repeatedly examined in a similar experiment, which is presented in section 5.1.2. Finally, possible sources and origins for the measured low lifetimes are discussed.

5.1.1.1. Sample Preparation

Asymmetric samples featuring the same passivation on either side were fabricated. The thickness of the silicon nitride capping layer was adapted to allow the same coupling in of light as for solar cells on the front side. Furthermore, aluminium was only screen-printed on the rear side in order to allow similar firing conditions to the actual solar cell process.
Starting from textured 6" n-type wafers, a HCl/HF cleaning sequence as well as an RCA cleaning step was carried out. This was followed by a separation of the wafers into 6 groups, which were then covered with different passivation layers and stacks. An overview of the used passivation layers & stacks and the process sequence is given in figure 5.1.
Depending on the type of passivation, the wafer was either oxidized, coated with aluminium oxide or silicon nitride. Furthermore, the samples were passivated using two different silicon nitride deposition techniques, direct PECVD or remote PECVD, referred to as CT-SiN_x and SiNA-SiN_x, respectively. Both deposition techniques are described in section 2.6.2. In the case of rear side passivation, both silicon nitride layers are referred to as capping layers, since in stack systems the silicon nitride is mainly protecting the underlying passivation layer from external influences such as co-firing of the aluminium paste. Approximately 200 nm thick silicon nitride capping layers were used that were deposited by either remote or direct PECVD deposition. On the front side, only 70 nm silicon nitride was deposited in order to allow optimum light coupling. This was followed by the separation of the 6" wafers into nine equally sized parts. Samples of each group were either not screen-printed at all or were screen-printed with one of the three aluminium pastes, Al D, Al O or Al N. All samples were fired at a temperature of 840 °C with a belt speed of 5400 mm/min. Samples, that were screen-printed with aluminium paste were then brought into a 37 % HCl solution in order to remove the paste residuals on top of the passivation layer/stack.

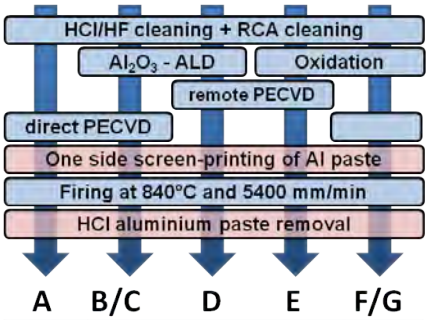

Group	Passivation stack/layer
A	SiN_x
B	10 nm Al_2O_3 / SiN_x
C	15 nm Al_2O_3 / SiN_x
D	15 nm Al_2O_3 / SiNA - SiN_x
E	15 min SiO_2 / SiNA - SiN_x
F	15 min SiO_2 / SiN_x
G	5 min SiO_2 / SiN_x

Figure 5.1.: Process sequence and different passivation groups

5.1.1.2. Stability Results

The stability of the passivation layers and stacks was analysed by comparing the arithmetic mean lifetime of non-metallized samples that were fired with the ones, which were screen-printed with aluminium paste and then co-fired, as well. The lifetime was measured using the photoconductance decay method, either in generalized or QSS mode. The results are shown in figure 5.2.
All passivation layers/stacks seem to be unaffected by the co-firing of one of the three used aluminium pastes, since in most cases the lifetime of the non-metallized samples is similar to

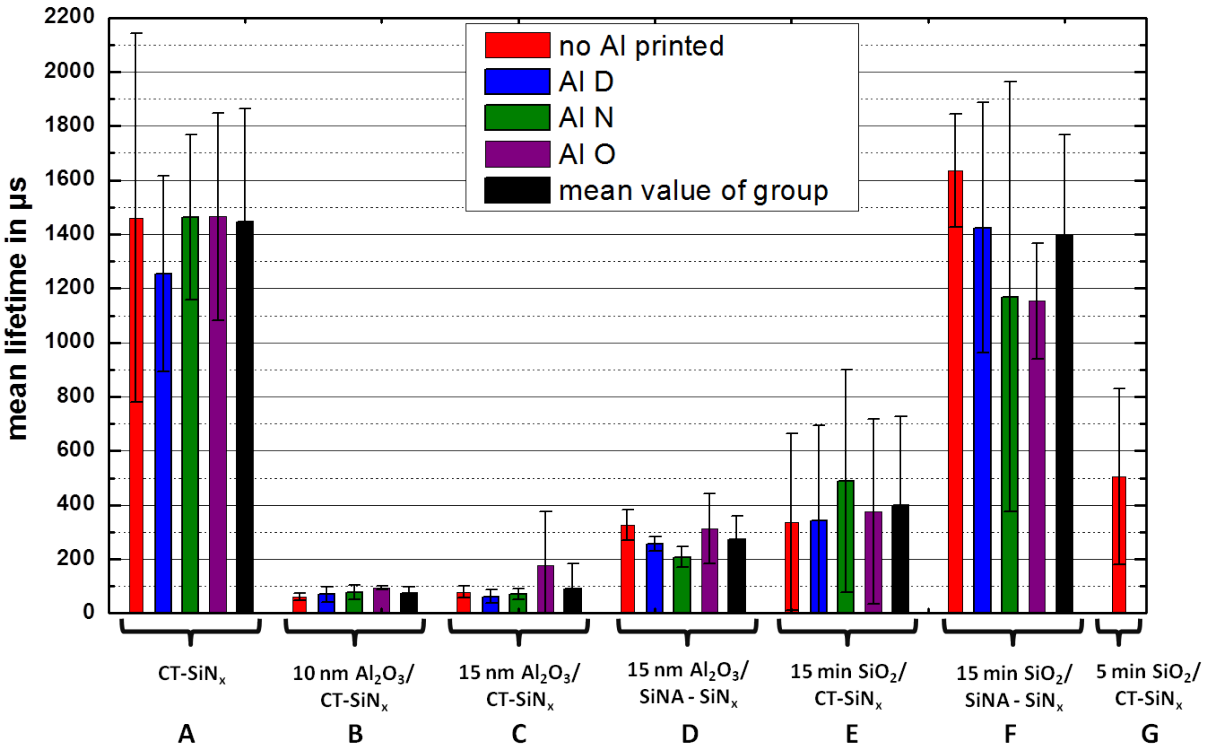

Figure 5.2.: Stability and quality analysis of the different passivation layers/stacks with one non-metallized, but fired group and three different metallized groups of which each is screen-printed with a different paste. The samples were analysed at a injection level of 10^{15} cm^{-3} in generalized mode.

the lifetimes of the metallized samples. This leads to the conclusion, that the passivation layers/stacks are stable for silicon nitride capping layers of 200 nm thickness. One exception can be group F, the (15 min) SiO_2/ SiNA-SiN_x passivation stack, in which the presented results indicate a deterioration of the passivation quality, since the mean lifetime is reduced for metallized samples. This is probably explained by the high standard variance of this group, and hence can be neglected.

5.1.1.3. Passivation Quality Analysis

Since measured lifetimes of most passivation layers/stacks are low, this section rather focuses on the analysis of the origin of these low lifetimes than on the total obtained values. Furthermore, the passivation quality analysis was repeated and is described in section 5.1.2.

Only two groups have shown an acceptable quality of surface passivation, assuming that all bulk lifetimes of the samples are similar. Previous experiments with the same substrate have shown bulk lifetimes exceeding 10 ms. The first group A, which is passivated by CT-SiN_x, average lifetimes of about 1400 - 1500 µs were obtained. Only group F has resulted in similar large lifetimes. The alumiunium oxide samples and the oxidized samples with a direct PECVD SiN_x

capping layer have shown medium to extremly low lifetimes.

Two different exterior influences are found on the performance of the samples and passivation layers/stacks, that have not been metallized but co-fired. This is carried out by using the photoluminescence method as it is explained in section 3.4.1.
First, strong imprints of the belt are found, which are visible in photoluminescence images as it can be seen in figure 5.3 **A**. These chain patterns indicate regions of higher (brighter - more counts/s) and lower (darker - less counts/s) excess carrier concentrations. Second, some samples have shown a distinct pattern in taken photoluminescence images such as the one shown in figure 5.3 **B**. This is referred to as pattern of three parts.

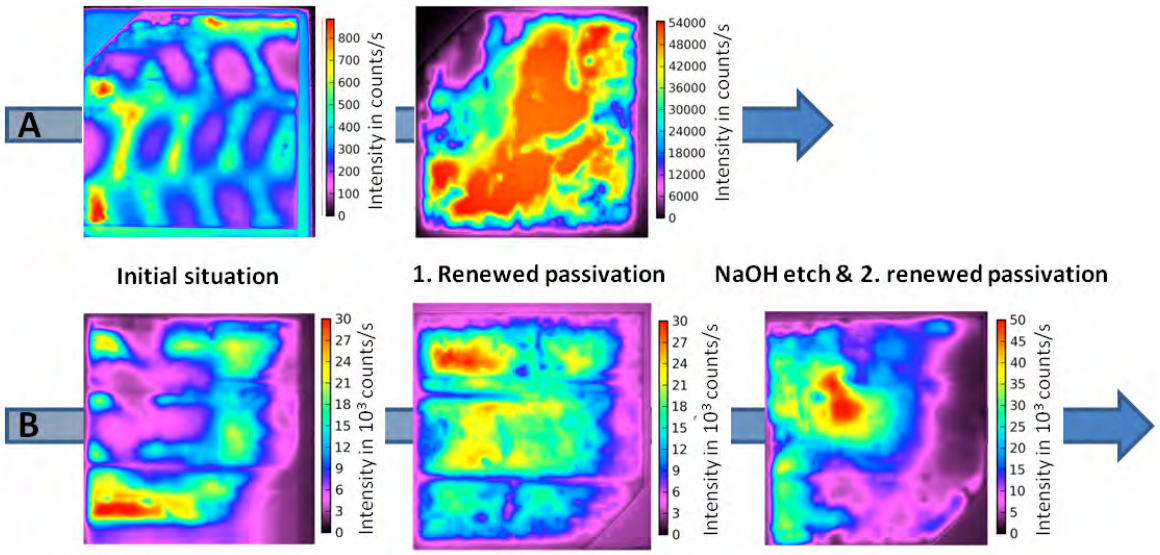

Figure 5.3.: **A**: Chain pattern before and after renewed passivation; **B**: Pattern of three parts. After first renewed passivation, no change is visible. An 10 min NaOH-etch and a followed renewed passivation is shown on the right side

The chain pattern is visible not in all samples, but throughout all the groups. Therefore it is not possible to find any relationship between the temperature sensitivity and the passivation layer/stack. Moreover, the pattern of three parts or similar patterns are also found in all groups.

The passivation was renewed for samples from group B and E in order to see, whether the passivation or the bulk was responsible for the obtained photoluminescence distributions. The passivation layer/stack was removed by a HF etch step, until the passivation stack fully vanished. After that, surface passivation was renewed by means of a temporarily Quinhydrone-methanol passivation.

Quinhydrone-methanol passivation is functioning as a chemical passiation by a previous HF-dip, which saturates dangling bonds, resulting in low densities of states at the surface. Then, residual hydrogen atoms, which are saturating the silicon surface, are forming strong bonds with quinhydrone. More on temporarily passivation using Quinhydrone-methanol can be found in [65] and [66].

After the renewed passivation, the sample that had shown a chain pattern showed an improved response in the photoluminescence image as well as no pattern. This indicates, that the chain

pattern is restricted to the surface passivation. Hence, temperature differences on the samples during co-firing have resulted in a varying lifetime over the sample, which was then removed by renewing the surface passivation. Brighter areas, therefore better performing regions were found right where the sample had been in contact with the chain and hence experienced a reduced temperature compared to the region in between the chain (purple region in the first image of **A**).
The pattern of three parts on the other hand remained on the sample after the first renewed passivation. A 10 minute NaOH etch back in a 20 % NaOH-solution after removing the first renewed passivation and a fresh temporarily passivation after the etch back led to a vanishing of the pattern. Furthermore, the measured counts are almost doubled, indicating a strong increase in the effective minority charge carrier lifetime. It can be assumed, that a surface contamination within the first few micrometers of the silicon resulted in an decrease of the lifetime and hence, after removal of these layers, the lifetime improved.

5.1.1.4. Discussion of the Stability Against Co-Firing and Passivation Quality Analysis

The passivation layers/stacks are found to be stable against co-firing of aluminium paste. This enables to fully cover the rear of wafers with locally opened passivation layers/stacks with aluminium paste, and therefore makes the fabrication of the Al-LARE and FALCON solar cell concepts possible. The absolute measured effective minority charge carrier lifetimes are low, especially for aluminium oxide passivation. Possibly, this is a result of contamination within the first 10 µms of the silicon wafer, which was incorporated during processing.
Another possible source for the low performance of aluminium oxide/silicon nitride stacks can be the insufficient formation of negative fixed charges, which are usually in need of an activation step in order to develop high densities. Low densities can lead to an increased SRV in the case of an n-type bulk, if the field-effect is attracting minority carriers to the surface and repelling majority carriers. This leads to the result, that both carrier densities are in a similar magnitude and hence SRH-recombination on the surface is peaking (assuming same capture cross sections for electrons and holes). This effect is discussed in section 2.6.3. A difference in the mean lifetime between CT-SiN_x (direct PECVD) and SiNA-SiN_x (remote PECVD) is found. This can be a result of the location, where the plasma is ignited. In the first case, the plasma is lit close to the wafers surface and could therefore damage the previously deposited aluminium oxide, while for remote-PECVD the plasma is lid far away from the wafer. The same argument fits for silicon oxide/silicon nitride stack passivation.

5.1.2. Analysis of Passivation Layers and Stacks

Symmetric samples fabricated from 5" 11 - 12 Ωcm n-type base material were used in order to evaluate the passivation quality of rear side passivation layers and stacks. The passivation quality is analysed by means of the effective minority charge carrier lifetime (further referred to as lifetime), which was measured before and after a high temperature step by photoconductance decay minority charge carrier lifetime measurements. For lifetimes exceeding 100 µs, the generalized mode was used, while below the QSS mode was applied. The lifetime was evaluated for an injection level of $\Delta n = 10^{15}$ cm^{-3}, which is important to acknowledge, since the passivation quality depends strongly on the injection level.
The samples were exposed to different peak temperatures in order to investigate the sensitivity of the passivation layers/stacks on high temperature processing.

5.1.2.1. Sample Preparation

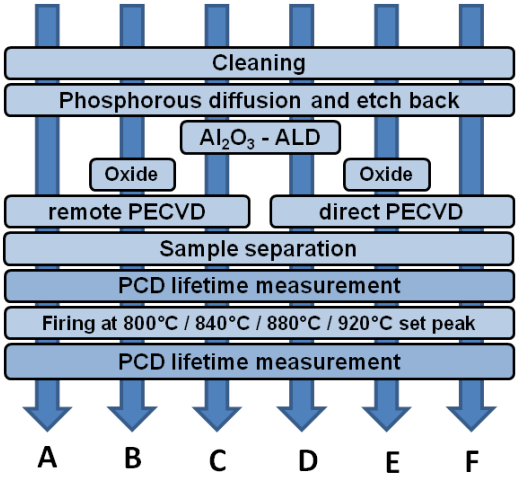

Group	Passivation stack/layer
A	SiNA-SiN$_x$ (remote PECVD)
B	15 min SiO$_2$ / SiNA-SiNx
C	15 nm Al$_2$O$_3$ / SiNA-SiNx
D	15 nm Al$_2$O$_3$ / SiN$_x$
E	15 min SiO$_2$ / SiNx
F	SiN$_x$ (direct PECVD)

Figure 5.4.: Sample preparation processing chart and overview over used passivation laysers/stacks

Previously textured wafers were etched back in a 22 % NaOH solution in order to remove the texture and fabricate non-textured samples. This was done, since the rear of passivated solar cells is also not textured. Subsequently, a standard HCl/HF cleaning process was carried out. For the dissolution of thermal donors incorporated in the substrate, a high temperature phosphorus diffusion was done which resulted in a FSF, that was removed in a 22 % NaOH solution etching for 5 minutes. This was followed by a successive cleaning step of HCl/HF as well as a standard RCA cleaning step. Depending on the planned passivation as they are shown in figure 5.4, the samples were either coated with a 15 nm Al_2O_3-layer, a SiO_2 layer or non of both. Furthermore, all samples were coated with a silicon nitride layer of 75 nm on the front side, either by means of direct PECVD (SiN_x) or remote PECVD (SiNA-SiN_x). Similarly, on the rear side, a 200 nm silicon nitride layer was deposited by means of remote PECVD or direct PECVD. A typical solar cell process was further emulated by a following firing step, which allows the incorporated hydrogen in the silicon nitride layer to be freed and saturate defects as well as dangling bonds [67]. The chain speed was held constant at 5400 mm/min, while the peak temperature was varied in intervals of 40 °C from 800 °C up to 920 °C.

5.1.2.2. Passivation Quality Results

The passivation quality is evaluated by comparing measured lifetimes before and after a firing step, which is carried out at different peak temperatures. The results are discussed by directly comparing two similar passivation layers/stacks, which feature the same passivation but different capping layers. As capping layers remote PECVD and direct PECVD, referred to as SiNA-SiN_x and CT-SiN_x, silicon nitride are used.

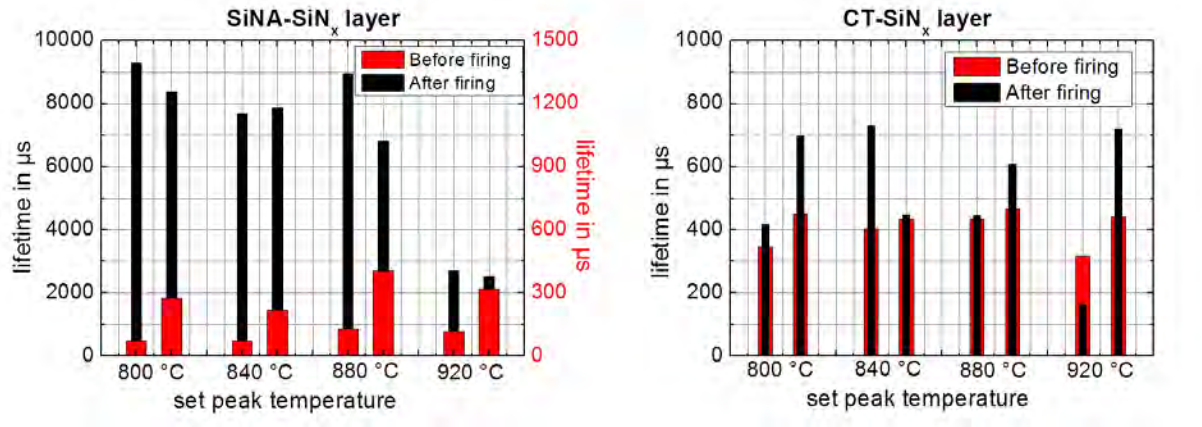

Figure 5.5.: Lifetime comparison of samples with SiNA-SiN_x and CT-SiN_x passivation layers for different peak firing temperatures before and after firing at an injection level of $\Delta n = 10^{15}$ cm^{-3} (measured in generalized mode)

In the first analysis, the quality of silicon nitride surface passivation deposited by means of either remote PECVD or direct PECVD is compared (thickness of 200 nm). The lifetimes prior to a firing step are quite similar for both deposition techniques and are between 200 to 450 µs (see figure 5.5).
This similarity is drastically changed after a firing step. While for SiNA-SiN_x, lifetimes of larger than 9 ms were obtained, CT-SiN_x led to only a small increase reaching up to 750 µs. Overall, considering the peak temperatures, a decrease of the passivation quality with increased firing peak temperature is visible for remote PECVD (SiNA-SiN_x) deposited silicon nitride, while for the direct PECVD deposited (CT-SiN_x) silicon nitride, the measured effective lifetime is varying strongly, but can be assumed not to be strongly influenced by the temperature. Altogether, having in mind the common firing set peak temperature of 860 °C, the SiNA-SiN_x is better suited to fit processing needs compared to CT-SiN_x.

In figure 5.6, the effective minority charge carrier lifetimes of silicon oxide/silicon nitride stacks (15 min/200 nm) are compared, whereas the silicon nitride was either deposited by means of remote PECVD or direct PECVD. Processing of both samples featuring different silicon nitride capping layers was equal, except for the deposition method of the silicon nitride. While the lifetime for the SiNA-SiN_x deposited silicon nitride before firing is reaching on average of 1 - 2.5 ms, the CT-SiN_x capping layer is resulting in lifetimes, that are much lower, about two orders of magnitude. Only lifetimes of roughly 20 - 40 µs were obtained, which were then measured using the QSS mode of the photoconductance decay assembly. This result is not changed after the firing step, while for low set firing peak temperatures an improvement for the SiNA-SiN_x capped samples in the case of silicon oxide/silicon nitride stacks can be found. Higher peak temperatures also led to a degradation of the lifetime compared to values obtained prior to the

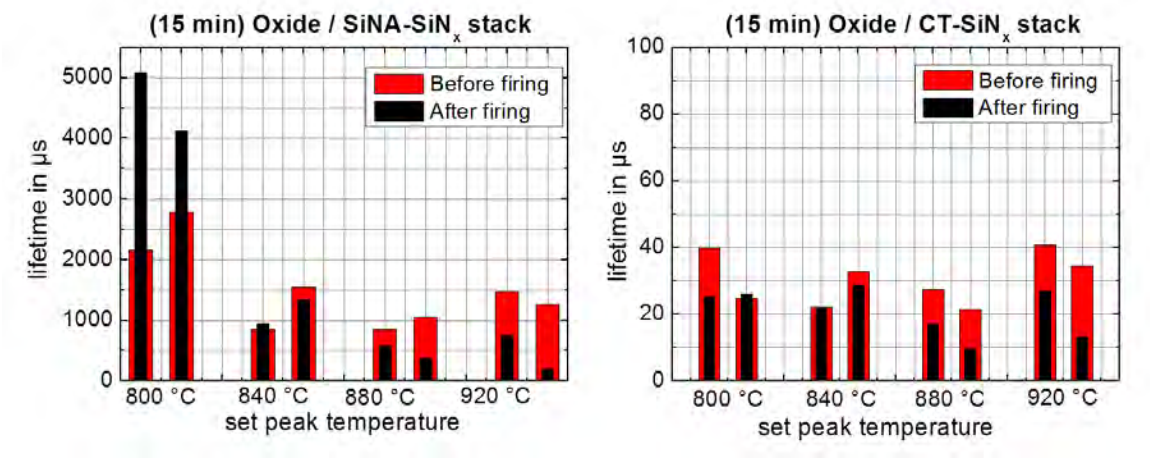

Figure 5.6.: Comparison of SiO_2/SiNA-SiN_x and SiO_2/CT-SiN_x stacks for diverse peak firing temperatures before and after firing at an injection level of $\Delta n = 10^{15}$ cm^{-3} (generalized mode)

firing. This indicates, that the silicon oxide/silicon nitride stack is not stable for high firing temperatures, since only an improvement of minority charge carrier lifetime can be found for the lowest set peak firing temperature (800 °C). Similar to this, the fired samples featuring a CT-SiN_x capping layer show also degraded lifetimes compared to the values measured before firing.

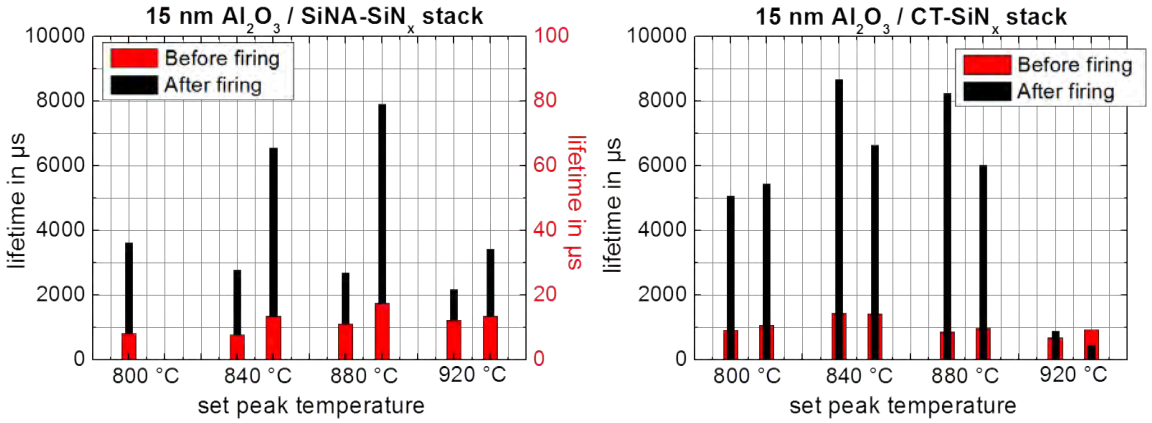

Figure 5.7.: Comparison of Al_2O_3/SiNA-SiN_x and Al_2O_3/CT-SiN_x stacks for different peak firing temperatures before and after firing at an injection level of $\Delta n = 10^{15}$ cm^{-3} (generalized mode)

Finally, the lifetimes of samples passivated by aluminium oxide/silicon nitride stacks (15 nm/ 200 nm) are compared and are showing interesting results, as well. The lifetimes prior to the firing step are low for the stack featuring a SiNA-SiN_x capping layer, whereas for samples with CT-SiN_x capping layer, the lifetime is reaching up to 1.5 ms. Firing of the samples covered with a SiNA-SiN_x capping layer results in a strong increase through all set peak firing temperatures to 2-8 ms. The CT-SiN_x capping layer group has performed very well (5-9 ms) for set peak

firing temperatures of 840 ℃ and 880 ℃, but showed a decreased performance for a higher temperature of 920 ℃.

5.1.3. Discussion of n-Type Base Passivation

The passivation quality of different passivation layers and stacks on lowly doped n-type silicon surfaces was analysed by means of measured effective minority charge carrier lifetimes.

Silicon nitride layer The SiNA-SiN_x layer performs very good after a firing step, while for the highest applied set peak temperature, a decrease in minority charge carrier lifetime was found. The n-type bulk passivation by means of SiNA-SiN_x obviously needs a high-temperature step, before it can unfold its potential. This is well researched especially for multi-crystalline silicon [17, 68] and has its origin in the freed hydrogen, which is diffusing in the silicon and saturates dangling bonds. On the contrast, the hydrogen passivation is only minimal for the case of CT-SiN_x. Overall, SiNA-SiN_x passivation performs best and is on a comparable level of Al_2O_3/SiNA-SiN_x bulk passivation. For conclusion it can be said, that the surface passivation quality is better in the case of remote PECVD deposited SiNA-SiN_x compared to silicon nitride deposited by direct PECVD.

Oxide/silicon nitride stack Unexpectedly, the lifetime of samples passivated by SiO_2/SiNA-SiN_x show a strong temperature instability. High lifetime improvements compared to the non-fired samples were measured for a set peak temperature of 800 ℃. To the contrary, no increase or even a decrease of the lifetime for higher temperatures is found. Thereby, this passivation stack is obviously not stable against high temperature processing, which is in strong contrast to the well performing passivation of highly doped n-type silicon surfaces by means of a SiO_2/CT-SiN_x stack that is commonly applied on the front side. Moreover, the lifetimes are two magnitudes higher for capping layers deposited by remote PECVD compared to direct PECVD deposited silicon nitride.

Aluminium oxide/silicon nitride stack The measured lifetimes for all samples are high, reaching up to several miliseconds and even higher for a CT-SiN_x capping layer. The latter is in strong contrast to the presented results in section 5.1.1, which showed an advantage of the Al_2O_3/SiNA-SiN_x stack compared to the Al_2O_3/CT-SiN_x, where measured lifetimes in the first case were approx. four times as high as the Al_2O_3/SiNA-SiN_x stack (see figure 5.2 group C and D). Only in the case of an Al_2O_3/CT-SiN_x stack, a temperature influence can be found for a high temperature firing step with a set peak temperature of 920 ℃. The very good performance after firing of the stacks is probably a result of increased hydrogen diffusion during high temperature resulting in a saturation of surface defects [69].

Overall, the highest passivation quality was achieved by the SiNA-SiN_x passivation layer, that performed best after a firing step and resulted in lifetimes of up to 9.5 ms.

5.2. Aluminium Emitter Formation and Passivation

Emitter alloying experiments were carried out in order to gain insights into the emitter formation, which depends on the co-firing parameters such as set peak temperature and belt speed (constant temperature profile assumed), but also on the deposited thickness of aluminium paste during screen-printing. In general, the more aluminium paste is brought onto the wafer, the deeper the emitter is alloyed. The emitter is characterized for different set peak temperatures as well as diverse belt speeds. It is assumed, that the same paste thickness is deposited onto all wafers. The emitter formation analysis is found in section 5.2.1.

High quality passivation of highly doped p^{++} regions (especially on boron emitters) has shown to be challenging due to the polarity of typical passivation layers such as silicon nitride and silicon dioxide [70, 71]. Passivated aluminium emitters are used in the FALCON cell concept and in order to achieve high efficiencies, identifying best performing passivation layers/stacks is important. The passivation quality on highly doped aluminium emitters is analysed in section 5.2.2.

5.2.1. Aluminium Emitter Formation

Asymmetric aluminium-alloyed emitter samples were fabricated in order to estimate the quality of the emitter by means of the emitter saturation current density j_{0e} and implied-V_{oc}. The samples were fabricated similar to the PhosTop solar cell, except for the FSF, which was etched back homogeneously. Furthermore, the front side was not metallized. The evaluation of the emitter was carried out by analysing the junction depth and doping profile concentration, which was done using an electrochemical capacitance-voltage profiler (ECV). The sample structure is depicted in figure 3.4 **B**.

5.2.1.1. Sample Preparation

n-type silicon wafers with a base resistance of approximately 10 - 11 Ωcm are used as the base material. The wafers were chemically textured prior arrival at our facilities. The 6" wafers were laser-cut into nine 5x5 cm^2 pieces.
Starting from this, a cleaning step with successive HCl and HF was done, which was then followed by a standard phosphourus diffusion in a quartz furnace at 859 °C. The process sequence is shown in figure 5.8. The phosphorus diffusion led to a sheet resistance of the surface of approx. 35 Ω/sq. Then, the samples were etched back to 100 Ω/sq in an EEB solution, which created porous silicon on top of the wafer. Porous silicon was then removed in a 0.1 % KOH solution. A HCl/HF and RCA cleaning step was carried out, which was followed by a dry oxidation at 900 °C for 7 minutes as it is explained in section 4.1.2. This was followed by a standard silicon nitride deposition on the front side in a direct PECVD quartz furnace leading to a thickness of 75 nm. Afterwards, screen-printing of three different aluminium pastes referred to as Al D, Al O and Al N was carried out on the rear side. The firing step was modified to evaluate different alloying speeds and temperatures

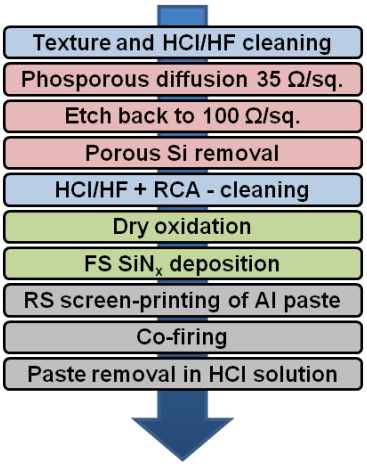

Figure 5.8.: Process sequence for the fabrication of emitter samples

for the samples. To be able to measure the samples by using a photoconductance decay setup, the paste was removed after the firing in a 37 % HCl solution.

5.2.1.2. Emitter Doping Profile

Typical emitter profiles are presented, which are measured using an electrochemical capacitance-voltage (ECV) profiler. The evaluation is carried out at varied set voltages for each measurement data point, which were adapted in some cases to fit the data in a proper manner. This is neccessary, since some problems with evaluating aluminium profiles were experienced. Furthermore, a few points were removed, which showed strong deviations from several neighbouring data points.

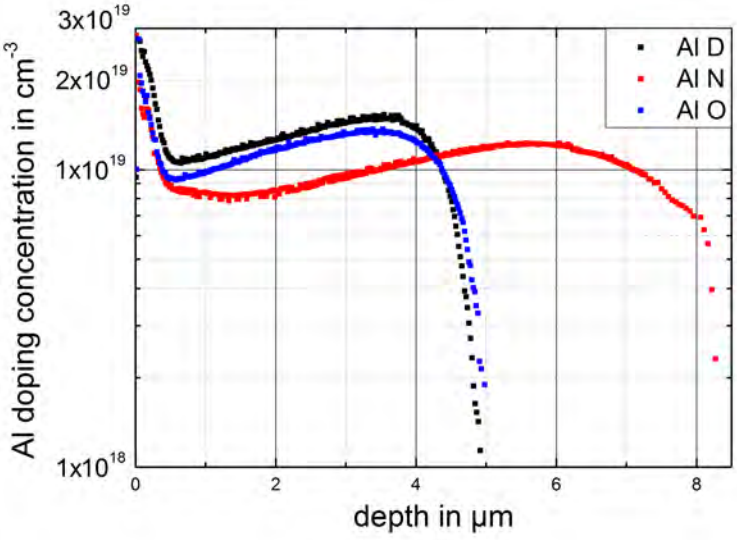

Figure 5.9.: Three different emitter profiles that are measured using the ECV method, fired with the same process parameters at 820 °C and a chain speed of 4400 mm/min

The measured emitter profiles are shown in figure 5.9. While the pastes Al D and Al O have resulted in a quite similar profile for the emitter having equal junction depths, the paste Al N is alloyed much deeper into the silicon. The latter resulted in a junction depth of almost 7 - 8 µm, while the other two are reaching only up to 4.5 µm deep. The peak concentrations are quite high (above 1.2 x 10^{19} atoms cm^{-3}), which leads to the conclusion, that boron was added to the selected pastes.

5.2.1.3. Emitter Saturation Current Density

The total saturation current density was measured using the photoconductance decay method previously described in section 3.3. Groups of two to three samples were formed for each paste and the respective firing parameters. The results are shown in figure 5.10. From the measured j_0 values, 20 fA/cm^2 were subtracted in order to account for the front side [9], while the base contribution was neglected.
Overall, the measured j_{0e} values are extremely low, considering, that the rear side is not passivated. Although the emitter profiles, which are shown in figure 5.9, exhibit different junc-

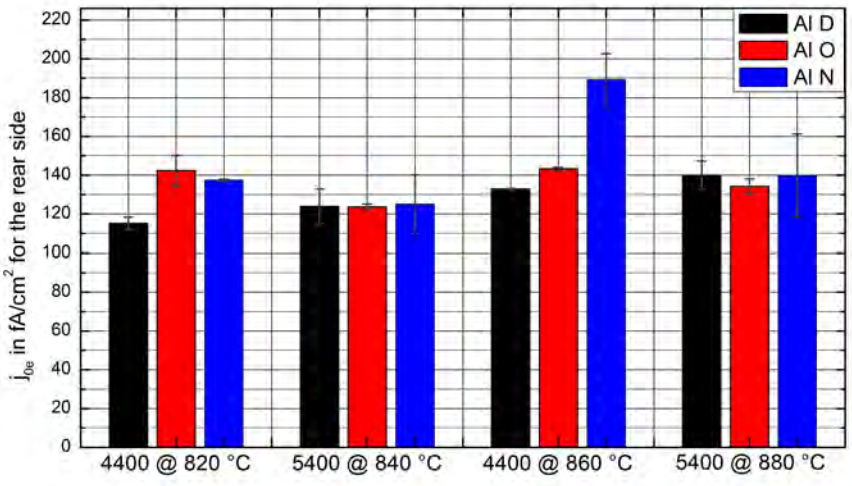

Figure 5.10.: Measured emitter saturation current density with subtracted front side influence (20 fA/cm^2) for different firing conditions and pastes. The values are obtained by using the slope of the fitted auger corrected inverse lifetime data as a function of the injection level, while a value at $\Delta n = 10^{16}$ cm^{-3} is used.

tion depths and even different surface concentrations, no correlation to the measured emitter saturation current can be identified, since almost all j_{0e} values are similar. This can be a result of the similar maximum peak concentration which is only slightly varying from 1.5×10^{19} dopants cm^{-3} for Al D to 1.4×10^{19} dopants cm^{-3} dopants cm^{-3} for Al O and further down to 1.2×10^{19} dopants cm^{-3} for the case of the Al N paste. The obtained values are ranging from 115 fA/cm^2 up to 140 fA/cm^2, while no significant influence of the firing conditions on the measured j_0 values can be found. Only one significant discordant value for Al N with an emitter saturation current of 180 fA/cm^2 is measured, which is probably a statistical outlier.

5.2.2. Etched Back Aluminium Emitter Passivation

The passivation quality of aluminium oxide/silicon nitride and silicon nitride on differently deep etched back asymmetric aluminium emitter samples with a homogeneously etched back FSF of 100 Ω/sq is analysed. The assessment is done using the so called Implied-V_{oc}.
First, the emitter profile is given for a sample, that has not been etched back at all. Second, the analysis of the emitter passivation is carried out.

5.2.2.1. Sample Preparation and Evaluation Sequence

The samples were fabricated in a similar manner as the FALCON solar cells that are presented in section 5.4. Mainly, three exceptions can be given. The FSF was fully etched back to 100 Ω/sq and therefore the samples feature only a homogeneous FSF. Since the samples do not need a metallization, the rear passivation was not opened locally by a laser and no pastes were screen-printed on the passivation.

Starting from 6" textured 11 Ωcm wafers, samples similar to the previously in section 5.2.1 presented structure featuring a homogeneous FSF and SiO_2/CT-SiN_x front side passivation, were fabricated.One exception during processing was the single side etching, which was carried out on the rear in order to remove the highly doped phosphorus layer. After the front side passivation was finished, the emitter was alloyed on the rear side by full area screen-printing of aluminium paste (Al Q) and subsequent co-firing at a set peak temperature of 840 °C and a belt speed of 4400 mm/min with the screen-printed side facing the top. The aluminium paste was etched off in a 37 % HCl solution for approx. 30 minutes. Subsequently, separation of the samples was carried out by using a Powerline 100D laser from Rofin, which included marking of the wafers on the rear side.
The alloyed emitter, which had a junction depth of approx. 5 µm was etched back in an approx. 20 % NaOH solution at 80 °C to various emitter depths. The etch back was monitored by weight differences prior and after the etch back. Furthermore, resulting sheet resistances were measured using a 4-point probe measurement assembly. This was followed by the first lifetime measurement using a Sinton Lifetime tester WCT-120, from which the saturation current density j_0 and implied-V_{oc} was calculated. This was followed by a further HCl/HF and Piraniha cleaning step. Two different rear side passivations were applied. One half of the samples were coated with aluminium oxide in the earlier described rpa-ALD of 15 nm thickness, whereas the other half were directly passivated by means of remote PECVD (SiNA-SiN_x), which was also used for the first group as capping layer (in both cases about 150 nm thick). Then, the resulting implied-V_{oc} and j_{0e} values were measured again with the help of the Sinton Lifetime tester. All samples were then fired at a set peak temperature of 850 °C and a belt speed of

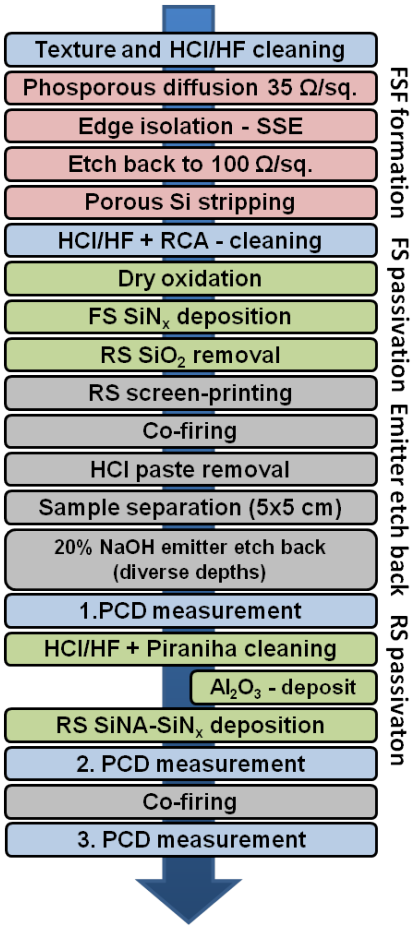

Figure 5.11.: Process sequence

5400 mm/min. This was done to reproduce real solar cell manufacturing, in which the silicon nitride passivation is activated and thereby the incorporated hydrogen freed. Finally, a third PCD measurement was carried out.

5.2.2.2. Emitter Formation and Passivation Results

The emitter formation is analysed by mapping of sheet resistance with the help of a 4-point probe and ECV measurements. ECV measurements are based on successively etching back a semiconductor surface e.g. silicon. By exposing the surface to an electrolyte, which under reverse bias conditions is acting as a Schottky-like contact (for n-type silicon), it is possible to determine the electrically active dopant concentration. Detailed explanation on this measurement technique can be found in [52] or [51].

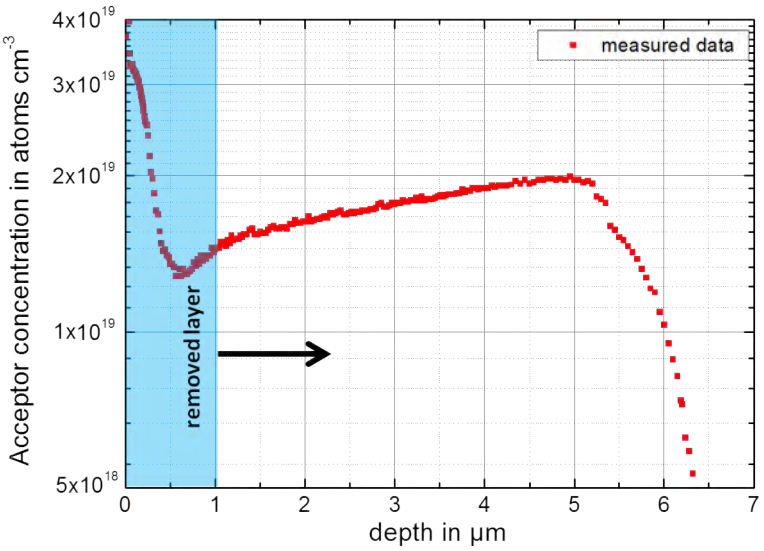

Figure 5.12.: Emitter profile obtained by ECV measurements for one non-etched back sample and indicated minimum etch back depth.

The surface peak of the non-etched sample exceeds 3×10^{19} atoms cm^{-3} due to aluminium-rich residuals on the surface (eutectic and lamellas). The junction depth is approx. 5.5 µm.

The emitter passivation quality was analysed by comparing measured implied-V_{oc} values of the differently deep etched back samples prior to the deposition of the passivation layer/stack, after it and past the firing step. The measured sheet resistances of etched back samples were not usable, since they vary strongly over the whole etched back surface. Strong variations of the obtained j_0 values for similarly deep etched back emitter samples were found. This is due to the fact, that j_0 is not calculated directly, but from the slope of a fit of the Auger corrected inverse lifetime data as a function of the minority charge carrier density [51].
Therefore, using the implied-V_{oc} as the emitter passivation quality criterion leads to much lower spread of the data, since it is directly calculated from the excess charge carrier density as it is shown in equation 3.13.

In figure 5.13 the measured implied-V_{oc} values are given for non-passivated differently deep etched back emitter samples as well as for both rear side passivations.

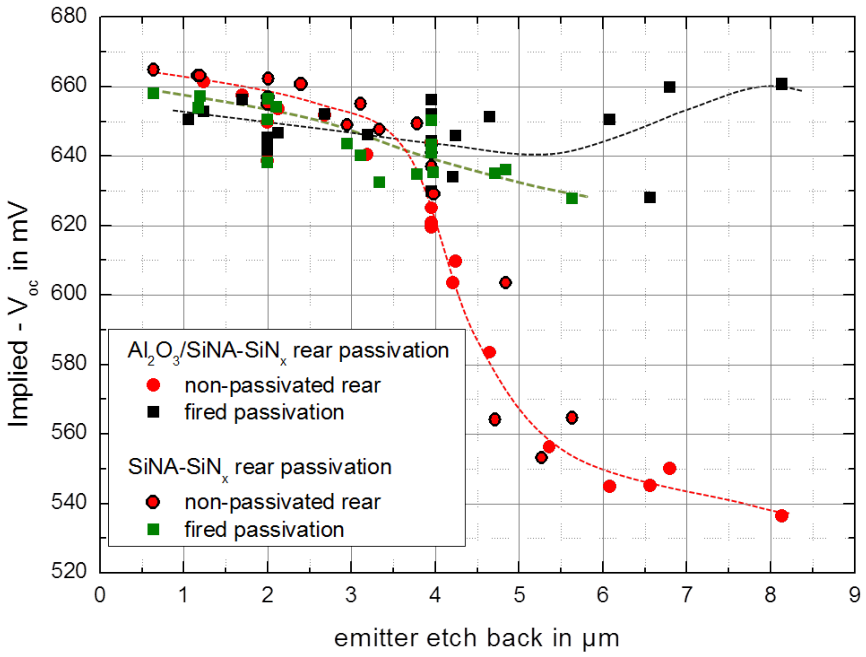

Figure 5.13.: Measured implied-V_{oc} values for differently deep etched back samples prior deposition of the rear passivation and after firing. Al_2O_3/SiNA-SiN_x and SiNA-SiN_x rear passivated samples are shown. Analysed at an injection level of $\Delta n = 5 \times 10^{15}$ cm^{-3}; Note: The dashed lines are a guide to the eye.

Starting from a non-passivated rear emitter, the measured implied-V_{oc} values are increasingly reduced the closer the surface gets to the actual pn-junction and stay almost constant after the emitter is fully removed. This is in good agreement with the simulation shown in section 4.3.2 (for the respective SRV). Furthermore, that clearly shows the effect of the field-effect passivation due to the emitter.
After firing at a set peak temperature of 850 °C with a belt speed of 5400 mm/min, the passivation quality of samples passivated by means of Al_2O_3/SiNA-SiN_x is showing implied-V_{oc} values of up to 650 mV to 660 mV over the whole etch back spectrum from about 2 µm to 8 µm. In contrary to the expectations, no increase of the implied-V_{oc} was found compared to the non-etched unpassivated rear side. Therefore, the passivation of the etched back emitter is not leading to a reduced effective SRV. An improvement was expected, since Bock [72, 75] showed enhanced rear side performance for etched back and passivated emitters.
Samples, passivated on the rear by SiNA-SiN_x show a similar result after firing of the passivation. While for slightly etched back emitters, the implied-V_{oc} results in higher values than for the Al_2O_3/SiNA-SiN_x passivation, the result changes with increased etch back depth and thereby lower field-effect passivation by the emitter. Then, the passivation quality is reduced for SiNA-SiN_x passivated samples, resulting in lower implied-V_{oc} values.

5.2.2.3. Renewed Passivation for Selected Samples

The passivation of selected samples was renewed, since the measured passivation quality was not improved compared to the unpassivated and non-etched case. Therefore the best applicable passivation was carried out in order to evaluate, if an improvement compared to the unpassivated rear can be nevertheless found.

First, the front side of selected samples from the last experiment was fully covered by protective wax using a Schmid Inkjet DoD 300. Then, the passivation on the rear side was removed in a 10 % HF solution. This was followed by a stripping step similar to the one described in section 4.1.2 in order to remove the protective wax on the front side. Before a renewed aluminium oxide deposit was possible, a HCl/HF cleaning sequence was carried out. The aluminium oxide was deposited in a FlexAl-reactor (rpa-ALD) at 300 °C for approx. 30 minutes, leading to a 30 nm thick layer on the rear side. After a 30 min anneal at 420 °C in a nitrogen atmosphere, the samples were again analysed using a Sinton lifetime tester at an injection level of $\Delta n = 5\times10^{15}$ cm^{-3} in QSS mode.

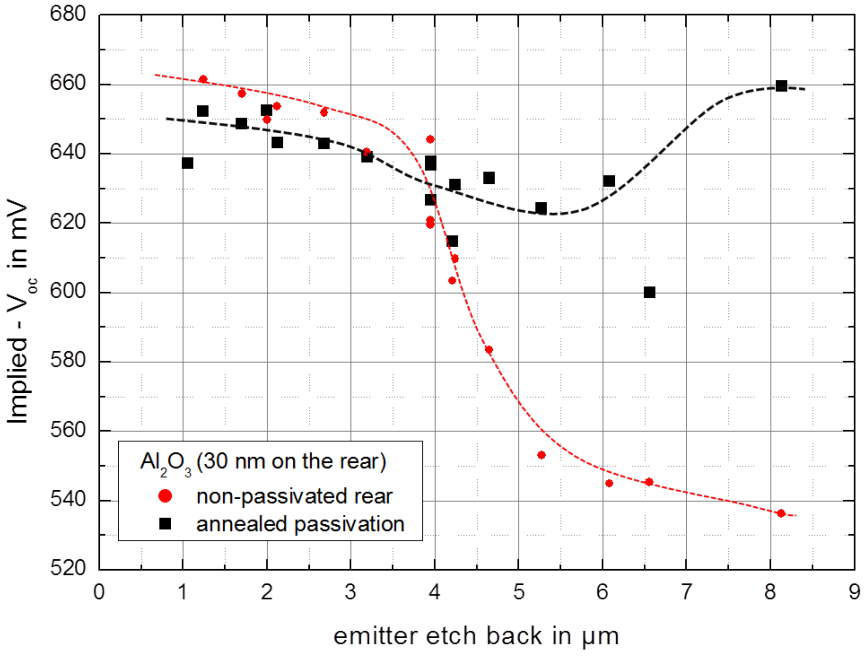

Figure 5.14.: Measured implied-V_{oc} values for differently deep etched back samples prior to the first deposition of the rear passivation and after the second passivation, which further was annealed at 420 °C in a nitrogen atmosphere for 30 minutes. The samples were analysed at an injection level of $\Delta n = 5\times10^{15}$ cm^{-3}; Note: The dashed lines are a guide to the eye

The data indicates, that even under a high quality passivation of annealed aluminium oxide, which usually leads to well passivated p^{++} surfaces [70], the passivation quality of the etched back emitter could not be improved, since implied-V_{oc} values are reduced compared to non-etched unpassivated case. For shallow emitters, the passivation is performing better than the etched back unpassivated case. Further the bulk is well passivated using aluminium oxide, too.

5.2.3. Discussion of Emitter Passivation

Most important, no improvement of the etched back passivated aluminium emitter compared to the unpassivated non-etched emitter could be found. In the first experiment, it was found that the passivation quality of Al_2O_3/SiNA-SiN_x and SiNA-SiN_x only outperform the strong field-effect passivation of the emitter, if the field-effect is already reduced (thinner emitter). This is in strong contrast to Bock [72, 75], who found an improvement of the passivated etched back emitter compared to the unpassivated non-etched rear side.
Bock showed in his thesis [72], that a p^{++} layer with a peak concentration of roughly 4×10^{18} atoms cm^{-3}, leading to a sheet resistance of 50 Ω/sq, can be well passivated using Al_2O_3, Al_2O_3/SiN_x or SiN_x. Since in our case an increased peak doping of slightly below 2×10^{19} atoms cm^{-3} (11 Ω/sq) is used (aluminium paste with additional boron), the unpassivated rear side features a reduced j_{0e} of 180-220 fA/cm^2 for roughly the same emitter depth of 5 µm, if compared to the values obtained by Bock ($j_{0e} = (800 \pm 200\ fA/cm^2)$. This enormous difference is a result of the strongly more effective field-effect in the emitter for the higher doping concentration. Therefore, in our case, the passivation quality is not enough to provide satisfactory, improved surface passivation on deep emitters, whereas Bock obtained satisfactory passivation results.
In order to validate the obtained results, the best available surface passivation was applied. A renewed passivation was carried out using an annealed 30 nm thick aluminium oxide layer on the rear. Although, the highest available quality of surface passivation for p^{++} layers was used, the passivation of the emitter was not satisfactory, leading to reduced implied-V_{oc} values if compared to the unpassivated non-etched rear. From this, it can be concluded that the firing of the passivation stack in the first passivation experiment did not lead to a reduction in passivation quality. Therefore, with the used passivation layers and stacks, no improvement on highly doped etched back emitters can be found compared to the unpassivated non-etched rear.

5.3. Al-LARE Solar Cells

n-type silicon solar cells with aluminium - locally alloyed rear emitter (Al-LARE) were fabricated. The front side passivation and metallization was unaltered from the improved PhosTop cell concept and hence featured a SiO_2/SiN_x stack as well as a s-FSF. The concept of the fabricated solar cells is described in detail in section 4.2.

The first analysis is focused on the emitter line spacings and widths, which were varied in order to determine the best performing rear side geometry. The rear was fully passivated with a SiO_2/SiN_x stack, which was then opened locally (or fully) by an externally provided picosecond laser. The rear geometry is evaluated by using j_{sc}, since the best trade-off between the effective diffusion length of minority carriers and the maximum gain in internal reflection due to the rear side passivation is leading to a maximum of j_{sc}.

Based on these results, the process was adapted and improved, which resulted in a best-performing Al-LARE solar cell of 17.0 %. Al-LARE solar cells are then compared with their in parallel fabricated improved PhosTop references.

5.3.1. Emitter Spacing and Width Analysis

Al-LARE solar cells were fabricated with rear grid finger widths ranging from 60 µm up to 180 µm in steps of 40 µm. Furthermore, total pitches of 400 µm up to 1200 µm in steps of 200 µm and a full area emitter reference PhosTop cell were used to identify best performing rear contact designs. An overview about the varied parameters is given in figure 5.15.

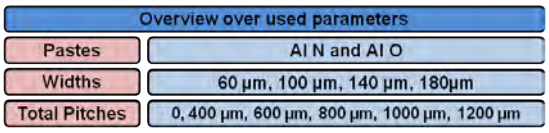

Figure 5.15.: Varied parameters

The results are averaged over two to three samples, while in some cases this was not useful and the highest obtained j_{sc} value has been used.
Initially, the experimental results for emitter widths of 100 µm are compared to the simulation results, that are presented in section 4.3.1. This is followed by a complete analysis of j_{sc} of the fabricated solar cells in order to identify best fitting widths and emitter spacings. Finally, a discussion of the experiment is carried out.

5.3.1.1. Solar Cell Fabrication Sequence

The solar cells fabricated for the emitter spacing and width analysis were manufactured similar to the improved PhosTop cell (see section 4.1.2). 6" wafers were processed until the front side was finished in this manner. One exception to the earlier presented standard process is the front side silicon nitride anti-reflection coating. In this case, it was deposited by means of remote PECVD. The whole process sequence for the presented emitter spacing and width analysis is shown in figure 5.16.

The rear side was covered with a 200 nm thick silicon nitride layer by remote PECVD, as well. Therefore, the rear was passivated by a silicon oxide/silicon nitride stack (approximately 7 nm thick SiO_2 layer), which was then opened using an externally provided picosecond laser. The pitches and widths of the openings were varied as shown in figure 5.15.

On one wafer, six 5 x 5 cm^2 cells featuring different rear line grids were lasered as it is shown in figure 5.17 **B**. The 5 x 5 cm^2 full area emitter PhosTop reference cell was fabricated by a full removal of the passivation layers.

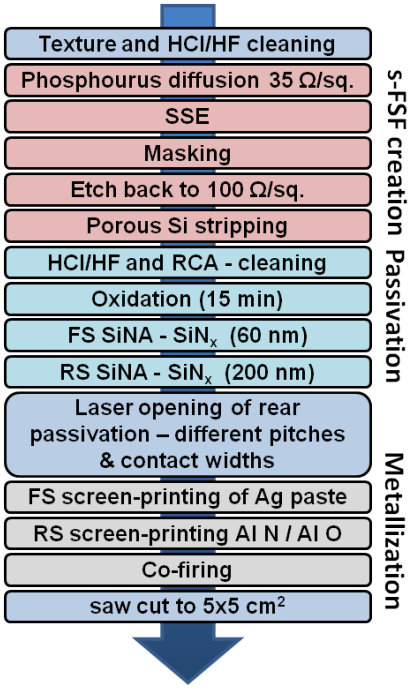

Figure 5.16.: Process sequence

The local removal of the passivation layer was followed by a standard front side and rear side screen-printing of silver and aluminium paste, respectively. Two different pastes were used, referred to as Al N and Al O. After the metallization was screen-printed onto the wafers, co-firing was carried out at a peak temperature of 840 °C and a belt speed of 4400 mm/min. Finally, the cells were saw-cut in 5×5 cm^2 samples, as it is indicated in picture 5.17 **B**.

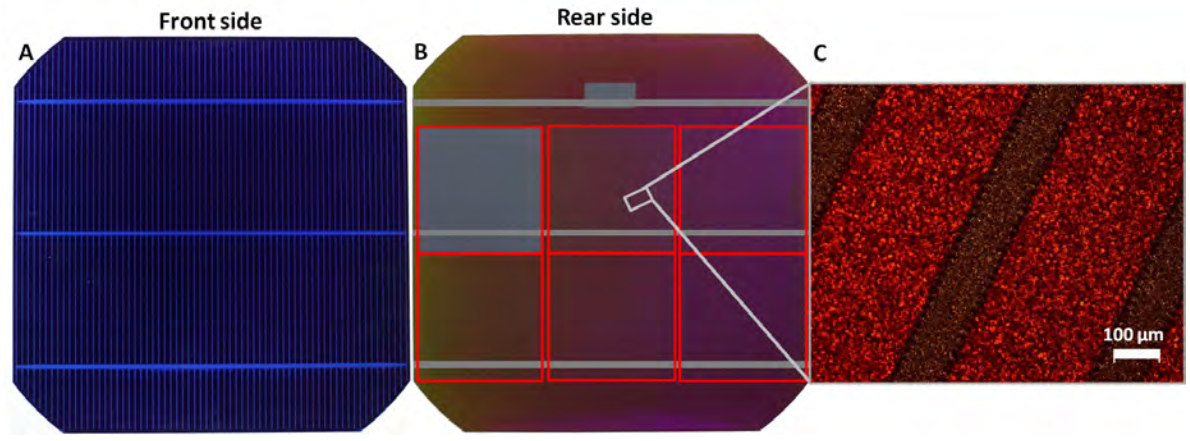

Figure 5.17.: **A**: Non-metallized front side image of a Al-LARE solar cell with visible s-FSF due to thickness variations of the oxide (brighter regions are the highly doped ones); **B** Non-metallized rear side image of the presented cell concept with 6 different rear grid design 5x5 cm^2 cells and the location of the busbar; **C**: Optical microscope image of a laser-opened passivated rear side with pitch of 400 µm and a line width of 100 µm.

Figure 5.17 shows the non-metallized front and rear side. On the front, the well-defined selective FSF is visible due to thicker silicon oxide layer underneath the silicon nitride, leading to a different reflection minimum. In **B**, the passivated rear side is opened locally with different width and pitches for each highlighted cell, which are the later on cut 5 x 5 cm^2 cells. Furthermore, the position of the busbar is shown. It is not situated in the middle, since the rear side laser openings were twisted by 90 degrees during the externally provided laser ablation of the passivation. This leads to an increased series resistance, which influences the FF of the finished solar cell, but not the j_{sc}. In **C**, a microscope image of a small region of one 5 x 5 cm^2 rear side cell design is shown.

5.3.1.2. Comparison of Fabricated and Simulated Al-LARE Solar Cells

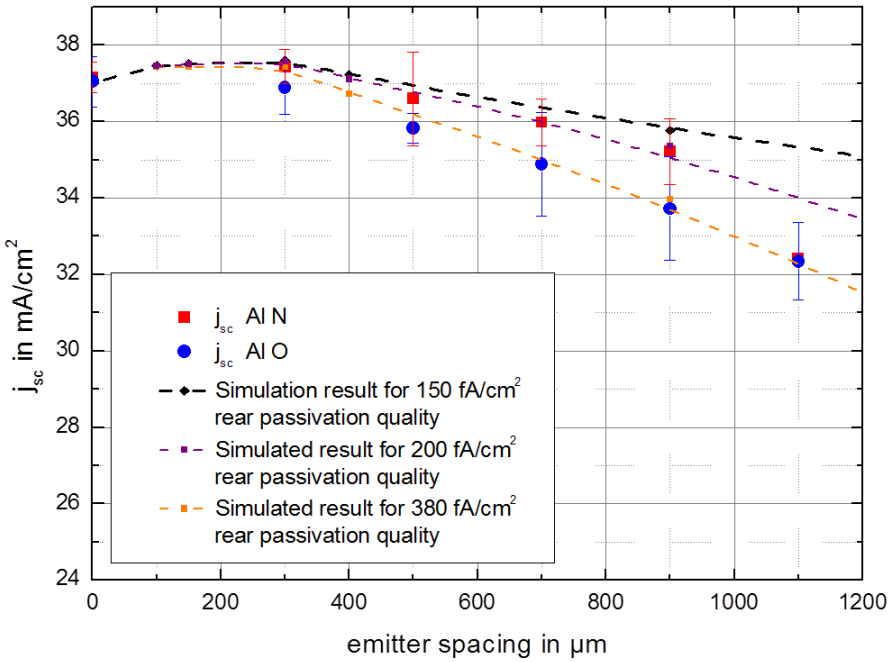

Figure 5.18.: j_{sc} as a function of the emitter spacing for two different Al pastes Al N and Al O and a rear finger width of 100 µm. Furthermore, the experimental data is compared to the previously in section 4.2.2 presented simulation for a passivation quality of $j_{01,passivated}$ = 150 fA/cm^2. The data is compared to further simulations; Note: The lines are a guide to the eye.

Al-LARE solar cells with a varied emitter spacing and an emitter width of 100 µm are analysed. The passivated area between two emitter fingers (referred to as emitter spacing) was enlarged to a maximum of 1.1 mm. The resulting curves are presented in figure 5.18 and are directly compared to PC2D simulation results.
The data indicates a maximum increase in the short-circuit current density for the Al N paste of about 0.3 mA/cm^2 at an emitter spacing of 300 µm compared to the reference cell. From this emitter spacing, the short-circuit current density is decreasing quite strongly for the paste Al N and faster than the simulation for a passivation quality of j_{01} = 150 fA/cm^2 indicates.

Further simulations were carried out in order to fit the measured values with PC2D simulations (same parameters used, except j_{01} at the rear surface passivation was varied). For Al N, the rear passivation quality is approximated to be 200 fA/cm^2, while for Al O the simulation shows a rear passivation quality of 380 fA/cm^2. In both cases, the simulation and measured values both fit well and decline almost linearly for increased emitter spacings. The paste Al O seems to affect the passivation quality stronger than Al N and hence the decrease of j_{sc} starts even earlier for Al O at emitter spacings of roughly 200 µm. The j_{01} value representing the passivation quality seems to be too low for allowing minority charge carriers in between two emitters to reach one of the emitters and hence the minority charge carrier diffusion length can be said to be strongly reduced by the surface.

5.3.1.3. Full Emitter Spacing and Width Evaluation

Besides emitter widths of 100 µm, solar cells featuring emitter widths of 60 µm, 140 µm and 180 µm were fabricated. The results are presented in figure 5.19 with lines for a small and a large emitter width for each paste. The lines are a guide to the eye only.

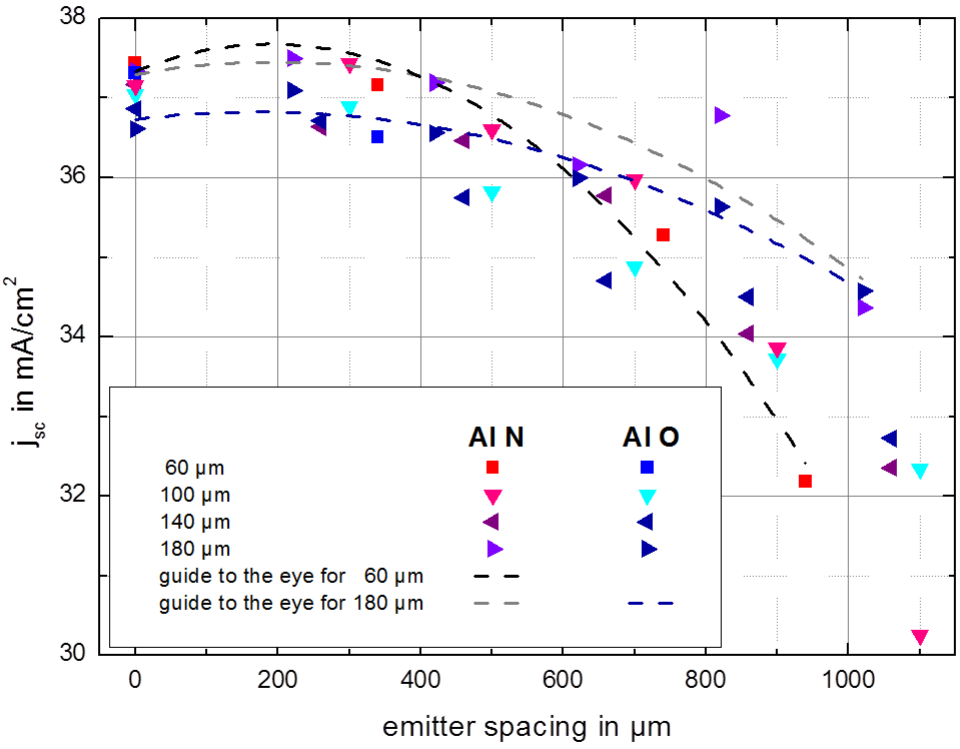

Figure 5.19.: j_{sc} as a function of the emitter spacing for two different pastes Al N and Al O and rear finger widths of 60 µm up to 180 µm in steps of 40 µm. Guides for the eye are given for the highest and lowest emitter spacing (except for Al O and 60 µm case due to missing data)

Basically, three trends can be identified from the results. First, j_{sc} is peaking at 300 µm emitter spacing for all emitter widths that are featuring a gain. For some emitter width groups no gain is found at all compared to the reference. Second, for increasing emitter width, the decrease of

j_{sc} as a result of increased emitter spacings and hence collection by the pn-junction, is reduced. Therefore, the influence of the surface passivation quality is reduced the wider the rear emitter fingers get. Third, overall, the aluminium paste Al N seems to perform better than Al O for all emitter widths. As discussed in the case of 100 µm emitter width, this seems to be a result of a paste induced degradation of the passivation quality.

By using spectral response measurements, it is possible to resolve the wavelength dependence of the quantum efficiency (averaged over the measured area) and hence with the help of a measured reflectivity to calculate the IQE. This was done for cells featuring 180 µm emitter widths and is shown in figure 5.20 for four different emitter spacings. The IQE and reflectivity is given in the wavelength range from 900 nm to 1200 nm, because shorter wavelengths are mostly absorbed before reaching the rear and hence, photons with wavelengths lower and closer to the gap energy are the biggest contributors to the j_{sc} gain from enhanced rear reflection.

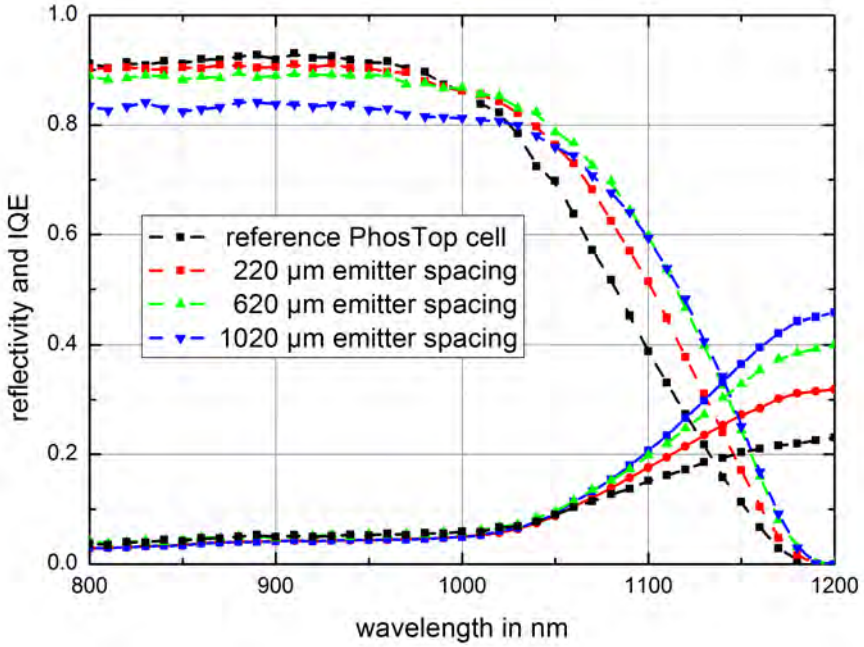

Figure 5.20.: Calcuated IQE and reflectivity for 180 µm emitter width for several emitter spacings and a full area rear emitter reference. The calibration was done using the measured j_{sc}

Calculated from the measured EQE, the IQE shows an improvement for all emitter spacings in the long wavelength regime, starting at wavelengths of around 1000 nm. This is due to the enhanced rear reflection of long-wavelength photons, resulting in an increased current generation, since less photons are absorbed in the rear metallization. This gain is also visible in the improved rear reflection at wavelengths above 1000 nm, if a full rear metallized solar cell is compared to an Al-LARE solar cell. In the case of emitter spacings above 1000 µm at a wavelength of 1200 nm, an increase in the measured reflection from 22 % to almost 46 % is visible.
Another effect is visible for increased emitter spacings. An overall reduction of the IQE is apparent in the plateau at wavelengths below 950 nm. While for small emitter spacings no such

effect is pesent, the difference of the plateau between the reference and Al-LARE solar cells is increasing with the emitter spacing. This seems to be due to a only slightly increased diffusion length, which is a result of a low rear passivation quality, if compared to a full metallized rear. This effect is intensified since the passivated area increases with increasing emitter spacing. Hence, with increased emitter spacing, carrier collection by the junction is reduced for carriers generated from wavelengths over the whole spectrum. If the front side passivation quality would be too low, the IQE would also increase from short to long wavelength, which is not the case for the presented IQE's.

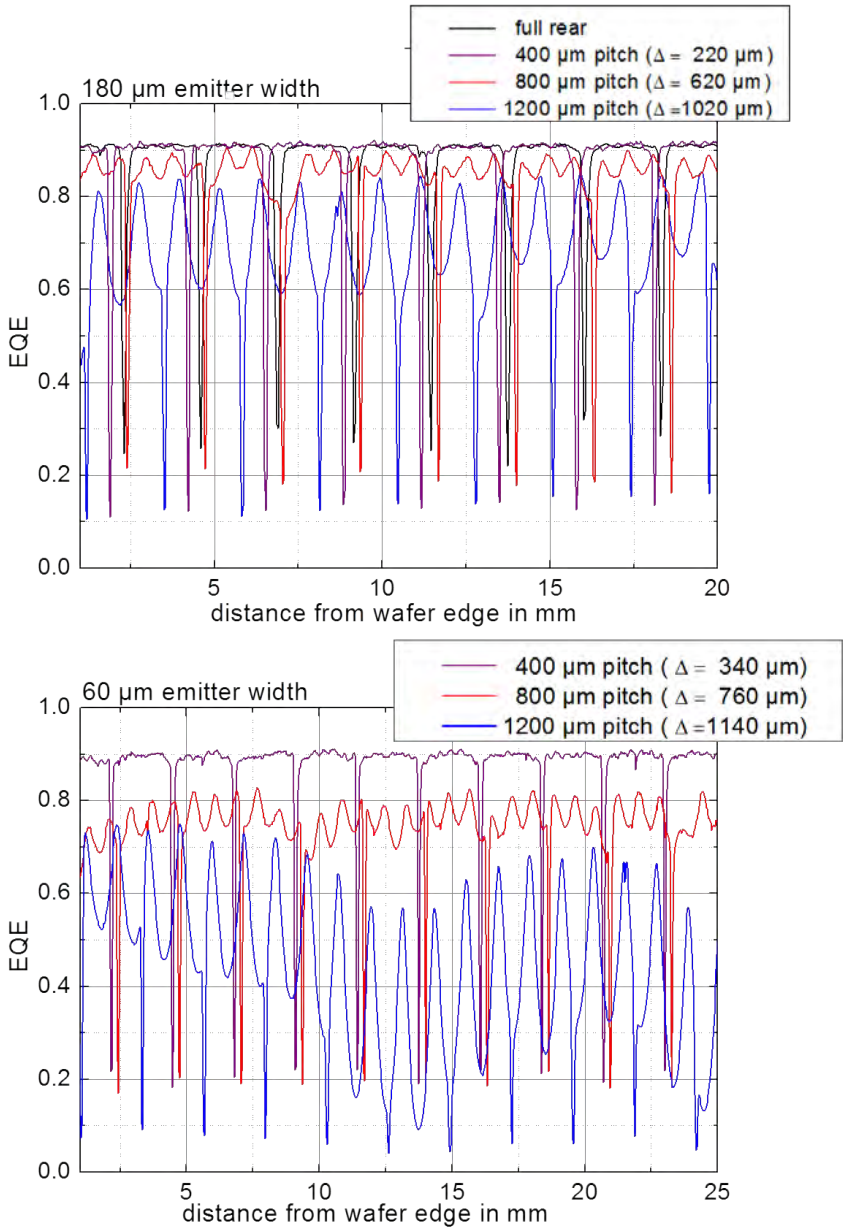

Figure 5.21.: Measured EQE for 180 µm (top) and 60 µm (bottom) emitter width for several emitter spacings and a full area emitter reference; Note: Δ refers to emitter spacing

The simulated EQE presented in figure 4.7 shows a similar behaviour. Since the reflection can

be assumed to be on the same level below wavelengths of 1000 nm for all simulated EQEs, the EQE drop of the simulated Al-LARE solar cells compared to the full rear metallized reference solar cell can be compared to the IQE drop, as well. Both curves show a strong drop over the whole spectrum starting for emitter spacings of roughly 400 µm or 620 µm, respectively.

The effect of the emitter spacings and width is furthermore analysed by using the Light-Beam Induced Current (LBIC) method. This method allows to locally resolve the quantum efficiency at a given wavelength. Therefore, it is possible to analyse the reasons for the decrease in j_{sc} with increased emitter spacings and the effect of the width, as well.
Since the main focus of this analysis is laid on the rear side, wavelengths in the near infra-red region were used. In this particular case, a laser diode with an intensity of 1.5 µW and a wavelength of 980 nm is used to locally excite carriers in the bulk, which are then collected by the junction and hence can be used to calculate the external quantum efficiency (EQE) via equation 3.1. For this analysis, line scans perpendicular to the front and rear side grid (both are parallel), were made. Therefore, a strong drop of the EQE is visible where the front metallization is situated. The measured results are shown in figure 5.21.

As expected from the previous results for the short-circuit current density and EQE dependence on the emitter spacings, the average EQE is decreased for increased emitter distances. This effect is more pronounced for an emitter width of 60 µm (emitter spacing increases as well). An average EQE of roughly 0.9 is obtained by both emitter widths for small emitter spacings and is on a comparable level with the EQE of the reference full aluminium covered improved PhosTop cell.
The EQE average is declining not only far away from the emitters, but also the average EQE at the location of the emitters is reduced. This effect is strong for the largest emitter spacing and results in an average EQE at the emitters of 0.8 and below 0.7 for 180 µm and 60 µm, respectively. The same behaviour of the EQE is presented in the spectral response measurements. Both drops are a result of a reduced diffusion length which is caused by the low passivation quality and its effect on the diffusion length.

5.3.1.4. SEM Analysis of Selected Samples

Scanning electron microscope (SEM) images are shown in figure 5.22 in order to gain insights into the formation of the emitter and the contact.

Scanning electron microscopy delivers superiorly resolved images compared to optical microscopy, since the optical resolving capacity is limited by the Abbe diffraction limit to about $\lambda/2$ (assuming maximum numerical aperature). For visible light, this limits the resolution to about 200 nm. In the case of a SEM, the wavelength of electrons can be varied by means of their acceleration voltage, and hence lower wavelength are possible. The resolution limit for two objects is then given by $0.61\lambda/\alpha$, with α being the aperture angle and λ the wavelength of the electron, leading to a maximum resolution of 1 nm for an acceleration voltage of 20 kV for the used SEM, a Zeiss Neon40 EsB. Detailed information about the used SEM can be found in [73]. Two different detectors are briefly described. The Inlens-detector, which is situated in the incident electron beam is the main collector of secondary electrons ($E \leq 50$ eV), which are either slowed down primary electrons (through scattering processes) or through scattering released electrons. Both are descendent from close to the surface and hence deliver surface information. Since the detector is placed in the electron beam, it gives only material contrast and surface information. The mentioned material contrast, including doping difference contrasts, can be made visible by using low energy primary electrons (with acceleration voltages of about 1 kV),

which results in a high secondary electron yield, that delivers information about the material condition. Topographic information is better resolved by the SE2-detector, which is detecting secondary electrons and/or back scattered electrons, depending on the polarity and strength of the applied voltage at the collector (a part of the SE2-detector). This allows to gather information about the topography of the sample.

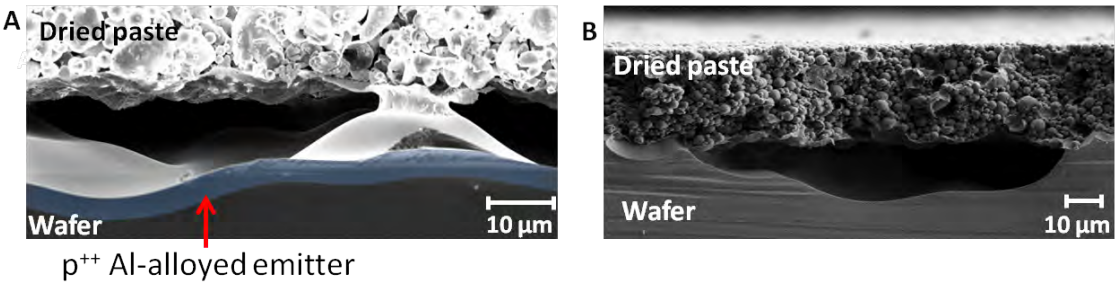

Figure 5.22.: SEM images of the rear of a 100 µm emitter width solar cell; **A**: not well alloyed and contacted reference PhosTop cell; **B**: unfilled contact of a Al-LARE cell; Note: The emitter is highlighted with a blue color

In picture **A**, a reference cell's alloyed emitter and contact is shown. It is important to notice, that the full rear emitter reference cells were fabricated by removing the passivation layer completely by using the same externally provided picosecond laser that was used for the local line openings. In the image it can be seen, that only a small contact has been formed to the highly doped aluminium-silicon alloy. If a small contact is present, the resulting series resistance is high in this region.
In picture **A** at the bottom of the paste, a thin layer of particles can be seen, which can be a result of laser damage caused by the laser opening or from residual passivation particles. This layer is supposedly been responsible for the bad emitter formation for the references but also for the Al-LARE solar cells.
In the case of Al-LARE solar cells, sometimes the emitter was not formed everywhere in every line opening, as it can be seen in figure 5.22 **B**. For lines, that are partially contacted, high series resistances of the current in the emitter should lower the FF. In some cases, the emitter was alloyed, but not contacted afterwards, as well.

5.3.2. Discussion of the Emitter Spacing and Width Analysis

The short-circuit current density gain compared to the reference improved PhosTop cell with a fully alloyed rear emitter was used as an assessment criterion. First, this was done because an overall low cell performance with extremely low V_{oc} values ranging from 500 mV to 610 mV, with especially low values for the references, were obtained. This should not influence the j_{sc}. Second, the dielectric on the rear was supposed to increase the j_{sc}, since the internal reflection is enhanced and thus long wavelength photons are more likely to be absorbed due to the increased optical path in the semiconductor.

Summarizing, this analysis shows an improved rear internal quantum efficiency and reflectivity in the near infra-red for all fabricated Al-LARE solar cells compared to the in parallel fabricated reference PhosTop cells. Furthermore, a gain in the short-circuit current density was obtained for Al-LARE solar cells, while emitter spacings of about 200 µm to 300 µm performed best for all emitter widths.

In this experiment, emitter formation and hence emitter quality is identified as the main problem. Low open-circuit voltages ranging from 500 mV to 610 mV were measured, which were very low compared to 640 mV to 650 mV for well performing PhosTop solar cells. Besides low open-circuit voltages, low fill factors ranging from about 55 % to rarely 70 % were measured.

By using measured dark I-V curves for estimating the j_{02} and shunt resistance, extremely high and low values, respectively were obtained by fitting the measured curve to the two-diode model. In extreme cases j_{02} was estimated to be around 2×10^{-5} A/cm^2, while normal values are around 2×10^{-8} A/cm^2. The shunt resistance, for well performing solar cells typically above a few thousand Ωcm^2, was in this case only a couple of hundred Ωcm^2. Both parameters are a result of contact and emitter formation problems and hence quality of the pn-junction as well as the intersection of the pn-junction with the surface.

From this analysis it can be concluded, that emitter widths of at least 100 µm are needed in order to sustain a expectable level of the quantum efficiency over the whole spectrum. Furthermore, emitter spacings of 300 µm to 400 µm perform best for low passivation qualities. If improvements in the passivation quality on the 11 Ωcm n-type material can be made, the emitter spacing can be extended, reducing the contact fraction even further and improving the rear side reflectance and hence j_{sc}.

5.3.3. Large-Area Al-LARE Solar Cells: Fabrication Sequence

Using the experience from earlier experiments, including the ones presented in the previous section 5.3, improved 6" Al-LARE Solar cells were fabricated. This was again carried out by starting with the front side passivation and s-FSF from the improved PhosTop cell concept and enhance the rear side performance by means of a SiNA-SiN_x, SiO_2/SiNA-SiN_x or Al_2O_3/SiNA-SiN_x passivation layer/stack. More details about the Al-LARE solar cell and a simulation-assisted analysis of the limitations and capabilities of this solar cell concept can be found in section 4.2.
In the emitter width and spacing analysis in section 5.3.1, it was concluded that an emitter spacing of 300 µm is fitting well. Furthermore, the width of the opened passivation was set to 100 µm, which results in a slightly higher alloyed emitter width. Overall, this results in an emitter and contact fraction of about 25 %.

First, the fabrication sequence is given in detail, which is then followed by the presentation of measured Al-LARE solar cell results. The key performance values such as j_{sc}, V_{oc}, the FF and efficiency η are presented and discussed. Furthermore, typical light-IV curves are fitted using the two-diode model, which allows to extract several properties of the solar cell, including cumulative series resistance and shunt resistance as well as j_{01} and j_{02}. This is followed by a loss analysis of the Al-LARE solar cells, including spectral response measurements, MLM (Multi-Light Method) series resistance measurements, electroluminescence images, LBIC EQE measurements and thermography images. The latter three are used combined in order to analyse the problems found with emitter formation and/or contacting of the emitter. This effect was already introduced in section 5.3.1.4.

Solar Cell Fabrication

Starting from the processing sequence of the improved PhosTop cell's front side, which was fabricated similar to the presented sequence given in section 4.1.2, the front side capping and

anti-reflection layer was deposited by means of remote PECVD (60 nm SiNA-SiN_x) after the oxidation. The whole process sequence is illustrated in figure 5.23.

For the SiNA-SiN_x and Al_2O_3/SiNA-SiN_x rear passivation, this was followed by a subsequent HCl/HF and RCA cleaning step. Al-LARE solar cells featuring a Al_2O_3/SiNA-SiN_x passivation stack were then brought into the rpa-ALD (remote plasma-assisted ALD), in which a layer of 15 nm aluminium oxide was deposited onto the bare silicon rear side. Then, all groups were deposited with a SiNA-SiN_x capping layer of approx. 150 nm thickness. By using a Coherent Talisker Ultra picosecond laser (wavelength of 532 nm, an intensity of about 1.22 W and a fluence of approx. 470 mJ/cm^2), the rear side passivation was locally removed. A spacing of 300 µm between the openings and a width of 100 µm was used. After the rear side was locally opened, a one minute NaOH etch in a 22 % solution was carried out in order to remove laser damaged silicon as well as residual particles. This was followed by a HCl/HF cleaning step.

On the front, a standard three busbar grid design was screen-printed with a fritted silver paste, which resulted in 60 µm wide fingers at a pitch of 2.32 µm. On the rear, full area screen-printing of a fritted aluminium paste Al O was carried out.

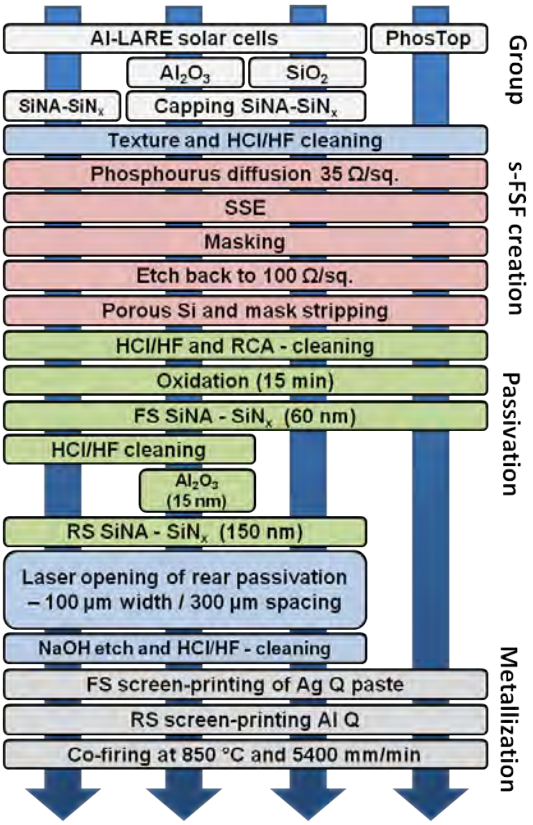

Figure 5.23.: Al-LARE and reference PhosTop solar cell process sequence

Finally, after a short paste drying step at a maximum set temperature of 375 °C, the solar cells were co-fired at a set peak temperature of 850 °C and a belt speed of 5400 mm/min.

For in parallel produced reference PhosTop cells, which are fabricated in the in section 4.1.2 presented manner, the non-metallized edge (about 1 mm) was removed by using a Disco DAD 341 saw. The reduced solar cell area mainly results in a short-circuit current density gain, since the rear side is only featuring an alloyed emitter area, which prior to the sawing step exhibited a 1 mm thick non screen-printed edge line, which was not passivated nor contacted and hence does not contribute to I_{sc}.

5.3.4. IV-Results

First, the IV results of the fabricated Al-LARE solar cells are presented in table 5.1, which were obtained using the sun simulator presented in section 3.1. The results are compared to the in parallel fabricated improved PhosTop cell references. Further result discussion and interpretation is done in section 5.3.5.6.

Fill factor The FF is strongly reduced compared to the references, while the reduction varies with the rear side passivation. From almost 80 % for the reference improved PhosTop

Table 5.1.: Results of Al-LARE solar cells corrected with the method described in section 3.1

Group	Cell Concept		FF in %	j_{sc} in mA/cm^2	V_{oc} in mV	η in %
A	Improved PhosTop cell	average	79.8	37.4	647.6	19.3
		best cell	80.0	37.5	648.2	19.4
B	Al-LARE cell (SiO_2/SiNA-SiN_x pass.)	average	72.2	36.8	625.6	16.6
		best cell	72.4	37.4	627.2	17.0
C	Al-LARE cell (Al_2O_3/SiNA-SiN_x pass.)	average	69.7	37.6	612.4	16.0
		best cell	71.0	37.6	619.7	16.5
D	Al-LARE cell (SiNA-SiN_x pass.)	average	66.0	36.5	599.7	14.4
		best cell	66.6	37.1	601.6	14.6

solar cells, the average FF is decreasing down to 72.2 % for a SiO_2/SiNA-SiN_x passivation and further below 70 % for Al_2O_3/SiNA-SiN_x rear passivation. The lowest obtained FF is the one for SiNA-SiN_x rear side passivation of roughly 66 %. Since the front side in all four cases is the same, the detoriation of the FF can be attributed to the rear side.

Short-circuit current density Improved rear internal reflection in some cases leads to a gain in the short-circuit current density compared to the reference, which is only found for Al-LARE solar cells featuring a Al_2O_3/SiNA-SiN_x passivation. From 37.5 mA/cm^2 of the best performing PhosTop cell (non-alloyed rear is removed by a sawing step), the current gain is approx. 0.4 mA/cm^2 for the best performing Al-LARE solar cell, which can be seen in the distribution of j_{sc} in figure 5.24. Overall, the obtained short-circuit current densities of the Al-LARE are moderately reduced compared to the reference.

Open-circuit voltage From almost 650 mV obtained for the improved PhosTop references, the open-circuit voltage is reduced for all Al-LARE solar cells. The average reduction depends on the type of rear passivation, while for SiO_2/SiNA-SiN_x rear side passivation the highest values are obtained of 627.2 mV and for Al_2O_3/SiNA-SiN_x passivation, typical open-circuit voltages are below 620 mV. For a rear side passivation by means of a SiNA-SiN_x layer, the measured V_{oc} is even more reduced down to 601.6 mV for best performing cells. Overall, this might refer to a high j_{01} for all cells, which can be a result of the rear side passivation quality. The distribution of the measured V_{oc} for the different rear side passivations is shown in figure 5.24.

Efficiency While for the best performing PhosTop solar cell an efficiency of 19.4 % is obtained, the solar cell featuring an SiO_2/SiNA-SiN_x rear passivation performs best, reaching 17.0 % efficiency. Furthermore, for Al-LARE solar cells featuring a Al_2O_3/SiNA-SiN_x rear passivation, the best performing cell leads to 16.5 %, while Al-LARE cells with SiNA-SiN_x rear side passivation resulted in a moderate best efficiency of 14.6 %. A short-circuit current density gain of 0.4 mA/cm^2 was only found for Al-LARE solar cells featuring a SiO_2/SiNA-SiN_x passivation, but due to very low V_{oc}, the efficiency was low. The reduced efficiency is caused by a low FF reaching only 72.4 % for the best cell, which is approx. 7.5 % less than the typical value for PhosTop solar cells. In combination with a strongly reduced open-circuit voltage, this results in the measured difference in the performance.

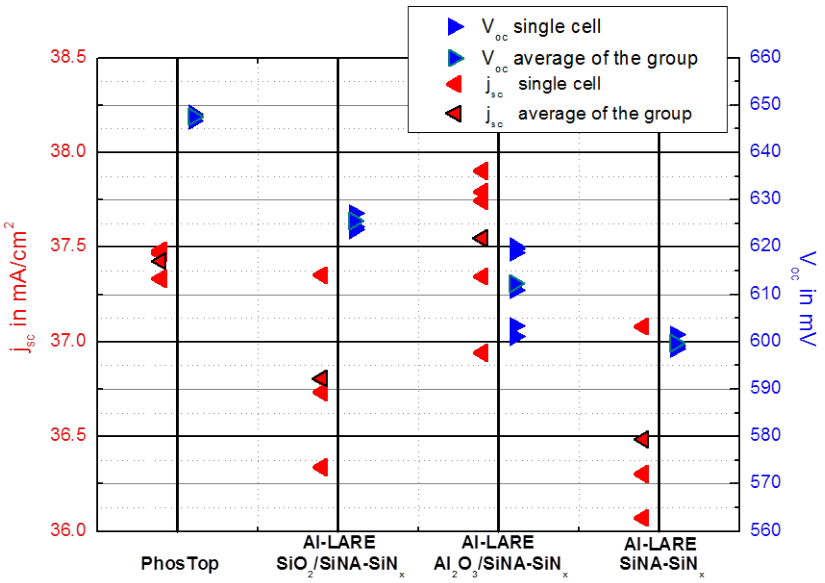

Figure 5.24.: Distribution of the measured j_{sc} and V_{oc} values for all cells and their respective average

5.3.5. Advanced Characterization and Discussion

The performance of Al-LARE and improved PhosTop solar cells is further investigated using several methods. First, the two-diode model is applied in order to extract series and shunt resistance as well as j_{01} and j_{02}. Subsequently, electroluminescence and spectral response measurements are presented. This is followed by a measurement of the series resistance using the multi-light method (MLM). Furthermore, the rear contact and emitter formation is analysed by using electroluminescence, illuminated lock-in thermography (V_{oc}-ILIT) in combination with SEM images and LBIC linescans. Finally the obtained results are discussed and compared.

5.3.5.1. Two-Diode Model Fitting

Light-IV curves of selected Al-LARE and reference PhosTop solar cells were fitted using the two-diode model, which is presented in section 2.2. This allows to extract the first and second diode's saturation current densities j_{01} and j_{02} as well as the series resistance R_s, shunt resistance R_{shunt} and if appropriate, another second diode's ideality factor n_2. The latter will be explained in detail later on. First, two fits are presented in figure 5.25 for a reference PhosTop cell and the best perfoming Al-LARE solar cell, which is passivated on the rear by means of a SiO_2/SiNA-SiN_x stack. The resulting parameters are presented in table 5.2. While for the PhosTop and Al-LARE passivated with SiO_2/SiNA-SiN_x solar cell it was possible to fit the IV curves fairly well, this was not the case for low performing Al-LARE solar cells, especially ones where the rear is passivated with Al_2O_3/SiNA-SiN_x and SiNA-SiN_x. Interestingly, it was possible to fit the logarithmic IV curve in an appropriate manner by adapting the second diode's ideality factor n_2, while such an adaptation is strongly controversial and therefore not presented.
The fit of the PhosTop solar cell gives a j_{01} of approx. 390 fA/cm^2, which is quite low for a non-passivated rear side. This is probably due to the strong field-effect passivation of the

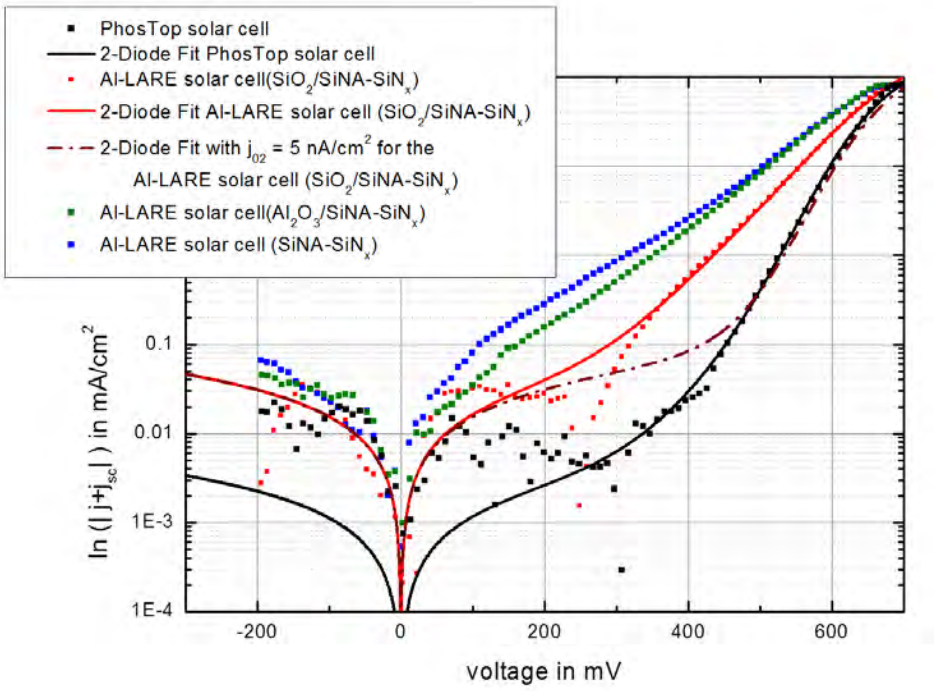

Figure 5.25.: Four different measured logarithmic IV curves with two-diode model fits for a PhosTop and the best Al-LARE solar cell

highly doped emitter. As expected, the Al-LARE cell fit with a SiO_2/SiNA-SiN_x passivated rear side resulted in a reduced value of 280 fA/cm^2, which is in agreement with an improved passivation quality. By using the linear relationship presented in equation 4.2 and 4.1 as well as by assuming that a first diodes saturation current density of 370 fA/cm^2 is plausible for a locally contacted area too (390 fA/cm^2 for the PhosTop - 20 fA/cm^2 from the front surface), the resulting passivation quality would further lead to a $j_{01,pass}$ of $\approx$ 250 fA/cm^2. This is in good agreement with the results presented in figure 5.18.
An extreme difference is found for j_{02}, with an increase from 5 to 130 nA/cm^2. Furthermore, the series resistance R_s is in both cases approx 0.6 Ωcm^2.

Table 5.2.: Two-diode model fitted values for the best Al-LARE and PhosTop solar cell.

Group	Cell Concept		FF in %	j_{sc} in mA/cm^2	V_{oc} in mV	η in %	j_{01} in fA/cm^2	j_{02} in nA/cm^2	R_{series} in Ωcm^2	R_{shunt} in Ωcm^2
A	Improved PhosTop cell	Cell	80.0	37.4	648.5	19.4				
		Fit	80.1	37.4	648.6	19.4	385	5	0.6	1.10E+05
B	Al-LARE cell (SiO_2/SiNA-SiN_x pass.)	Cell	72.4	37.4	627.2	17.0				
		Fit	72.4	37.4	627.3	17.0	280	130	0.6	6.50E+03

A two-diode model fit of the Al-LARE solar cell featuring a SiO_2/SiNA-SiN_x rear side passivation was adapted by changing the second diode's saturation current density to the same value of the reference PhosTop cell, while the other parameters were held constant. The resulting

curve is visible as a dashed line in figure 5.25. j_{02} was reduced in the fit from 130 nA/cm^2 to the value extracted for PhosTop solar cells of 5 nA/cm^2. This resulted in a FF improvement of 7.6 % to 80 % and an increase of approx. 30 mV to 657 mV in open-circuit voltage compared to the fabricated cell. Together, this resulted in an efficiency gain of 2.7 % absolute to 19.7 %. That indicates the potential of the cell concept, if the second diode saturation current density can be strongly reduced. It is important to mention, that the lower j_{02}, the more j_{01} and R_s are dominant and hence affecting the performance. Therefore, small changes in j_{01} and R_s can change the presented results dramatically. The accuracy of fitting j_{01} on the measured IV-curve depends on the value of j_{02}, since both express themselves in the same region of the IV-curve.

5.3.5.2. Electroluminescence

Electroluminescence images for selected solar cells of each group are shown. All images were taken with the electroluminescence assembly explained in section 3.4.1. A current density of 34.9 mA/cm^2 was applied, which led to different voltages, depending on the performance of the cell.

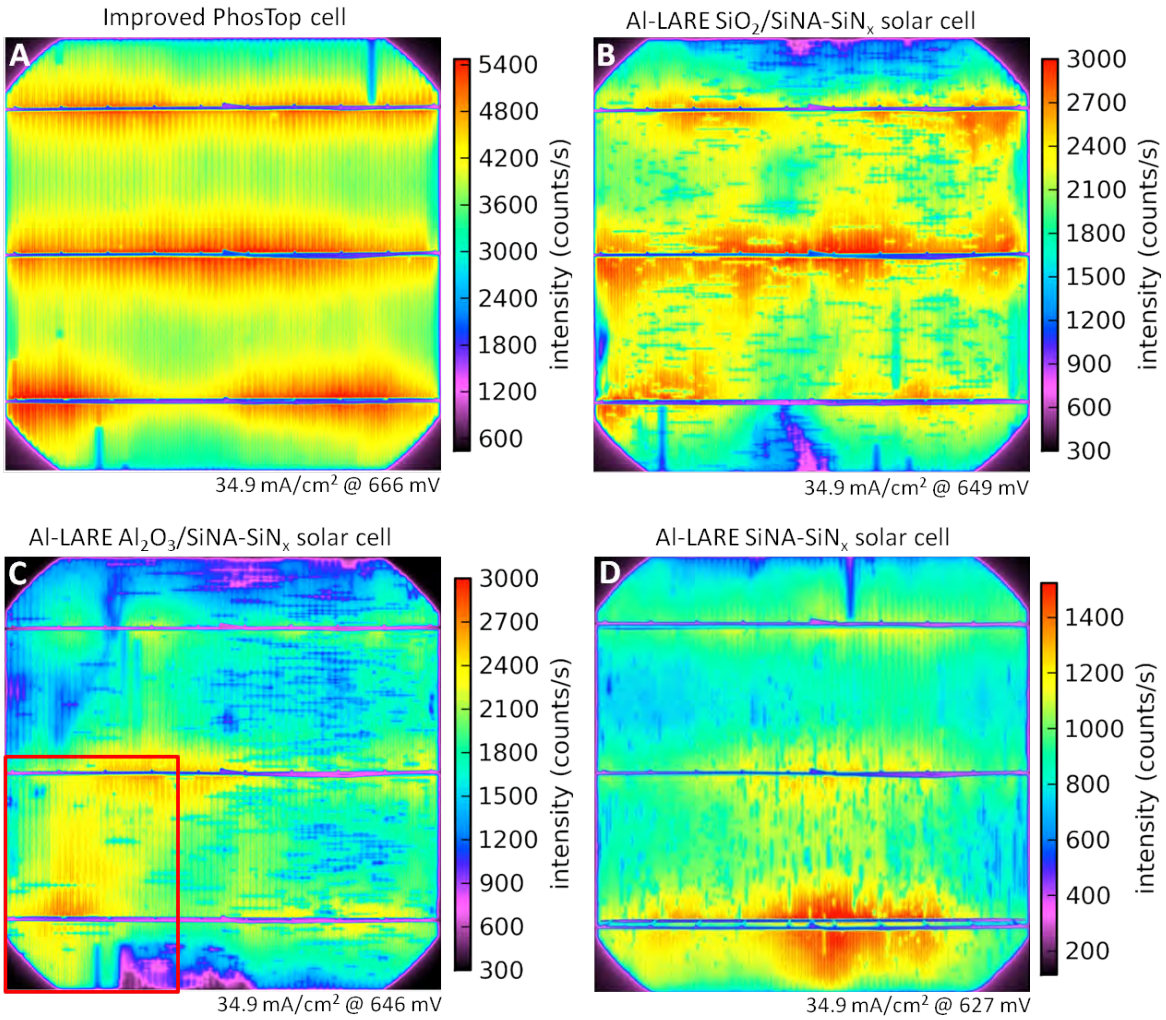

Figure 5.26.: Selected electroluminescence images of an improved PhosTop cell **A** and diverese Al-LARE solar cells **B-D**

While for the reference improved PhosTop cell (see figure 5.26 **A**), high intensities (counts/s) over the whole wafer are visible, all Al-LARE cells show strong indications of local contact or alloying problems at the rear. For all differently passivated Al-LARE solar cells (**C-D**), lines are visible, that are indicating rear side contact or emitter collection problems, since the luminescence in this region is reduced. Image **B** and **C** are cells, where the rear contact grid was twisted by 90 degrees to the front fingers. This enables to separate front and rear side effects more clearly.
The improved PhosTop solar cell in **A** shows a normal electroluminescence. The signal typically decreases between the busbars due to the fact, that the current is applied at the busbars and hence decreases, the further it travels into the finger. In figure 5.27 **B**, a typical result for an Al-LARE solar cell is shown, that in this particular case features a SiO_2/SiNA-SiN_xrear passivation stack. The signal level in this case is the strongest for all Al-LARE solar cells, while all differently passivated Al-LARE solar cells show regions of not well performing areas, that are probably a result of non-contacted or non-alloyed emitter lines. This can be assumed, since the visible, less well performing regions or lines (contrast) are at the location of the local opening. This is analysed in a direct comparison of electroluminescence images, LBIC linescans, thermography and SEM images in section 5.3.5.5 by using the highlighted area of figure 5.26 **C**.
In the case of SiO_2/SiNA-SiN_x rear side passivation, the average measured intensity is slightly reduced compared to the Al_2O_3/SiNA-SiN_x passivated Al-LARE solar cell. As the solar cell results indicate, SiNA-SiN_x rear passivated solar cells are showing an even stronger reduction of the average intensity. In both cases, many bad performing regions are line shaped, if they are compared to their vicinities.

5.3.5.3. Spectral Response

Spectral response measurements were carried out in order to analyse the short-circuit current density results of the Al-LARE solar cells as well as the optical performance. The resulting curves are shown from 370 nm up to 1200 nm, while some measured data points were removed, that clearly showed a non-physical behaviour (e.g. IQE above one). The calculated IQE was scaled to the measured j_{sc} values of each solar cell.
A small variation in the reflection minimum is visible for the presented solar cells in the reflection curves (measured including busbar reflection). The improved PhosTop shows the lowest reflection with the optimum minimum at 600 nm, while the others, especially the SiO_2/SiNA-SiN_x and SiNA-SiN_x passivated Al-LARE have their minimum in reflection at lower and higher wavelengths, respectively. Since the effect on j_{sc} is probably small, it can be neglected.
A gain in the rear reflection above 1100 nm of the Al-LARE solar cells compared to the improved PhosTop cell is clearly visible. The measured reflection (incident direct reflection and front escape) is increased at 1200 nm from 21.6 % for the reference up to 35.2 % for the with SiO_2/SiNA-SiN_x passivated rear Al-LARE solar cell. This results in an increase in the IQE, which can be found for all Al-LARE solar cells compared to the reference. The long-wavelength IQE improvement should have resulted in an increased j_{sc}, but due to a lowered plateau of the IQE over the whole spectrum compared to the reference, this was not the case.
For all solar cells a slope in the plateau of the IQE from large to short wavelengths is visible, which can be attributed to front side recombination. This is because the junction is on the rear side and low wavelength photons are mainly absorbed close to the front surface and therefore more losses occur for minority charge carriers generated from short wavelengths due to the front surface passivation.

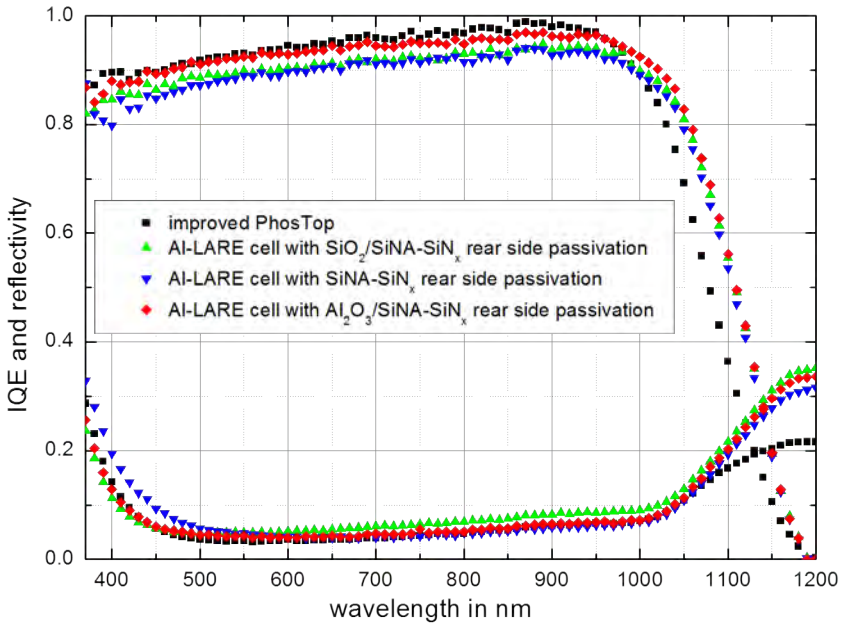

Figure 5.27.: Measured reflectivity and calculated IQE from the reference and all differently rear passivated Al-LARE solar cells; Note: the IQE was scaled after the respectively measured j_{sc}.

For wavelengths below 400 nm, the measured results are not reliable anymore, since the measurement assembly is not well performing while analysing low occuring currents during measurement due to low excitation intensities.

5.3.5.4. Series Resistance Evaluation Using the Multi-Light Method

By using the sun simulator, which was presented in section 3.1, it is possible to extract the series resistance as a function of applied voltage [37]. This was done using metallic gratings, resulting in reduced light intensities of approx. 82 % and 93 %. It is important to vary the light intensity only slightly in order to avoid changing conditions of the solar cells due to e.g. the injection level dependence, which can alter the current paths and diode currents of the solar cell. In this analysis, the series resistance was only analysed for voltages ranging from 450 mV to slightly above 650 mV, since the maximum power point MPP series resistance and the series resistance at V_{oc} are the most relevant.
In figure 5.28 typical series resistances as a function of voltage are given for three different solar cells. The first, a reference PhosTop solar cell, shows a decrease from the MPP, where R_s is slighly above 0.7 Ωcm^2 down to below 0.6 Ωcm^2 for V_{oc}. This is in good agreement with the series resistance value of 0.6 Ωcm^2, which was extracted from the fit. In the case of a rear passivated Al-LARE solar cell, the obtained values are higher, with some cells showing series resistances at the MPP of up to 1.8 Ωcm^2. The presented Al-LARE solar cell passivated on the rear by means of Al_2O_3/SiNA-SiN_x showed a strong decline from the MPP ($R_s \approx 1.2\ \Omega cm^2$) down to V_{oc} (R_s slightly above 0.7 Ωcm^2). While this is a higher series resistance, the performance would not suffer as extremely as the performance has if compared to the reference. Interestingly, this is also in good agreement with the fit of a Al-LARE solar cell, which features a Al_2O_3/SiNA-

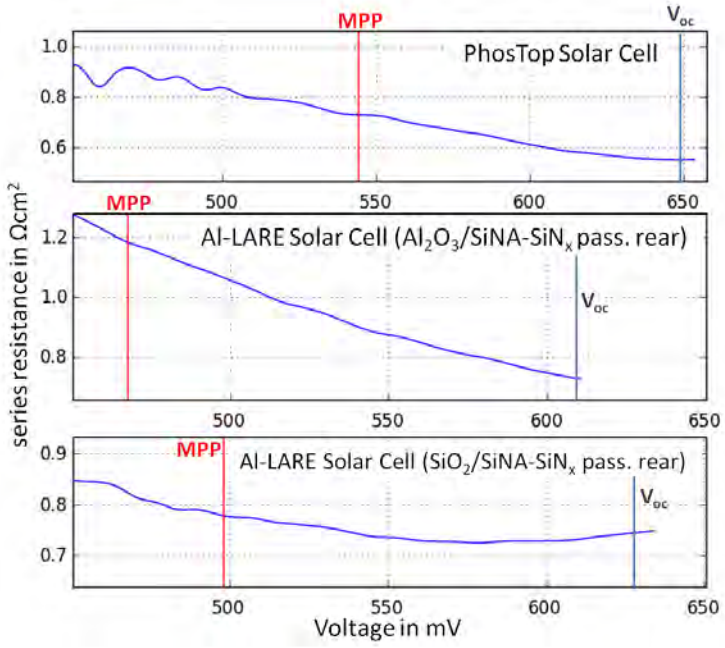

Figure 5.28.: Series resistance trends as a function of voltage are given for a PhosTop solar cell and two differently passivated Al-LARE solar cells. The red line indicates the maximum power point (MPP) and the blue line V_{oc}.

SiN_x rear side passivation (not shown). Furthermore, the best performing Al-LARE solar cell concept, which features a SiO_2/SiNA-SiN_x rear side passivation again shows a decreasing series resistance from below 0.8 Ωcm^2 at the MPP down to approx. 0.75 Ωcm^2 at V_{oc}. This R_s is slightly higher as the series resistance extracted from the fit in section 5.3.5.1, which was 0.6 Ωcm^2.

5.3.5.5. Rear Contact and Emitter Formation Analysis

In this section, a selected area of an electroluminescence image taken from Al-LARE solar cells is further analysed. Previously referred to as low performing lines, this destinct element is further investigated. First, temperature differences within a region of a selected Al-LARE solar cell are compared to the same region under electroluminescence investigation. Temperature variations in the solar cell are monitored using the illuminated Lock-in thermography under V_{oc}-conditions.
Illuminated Lock-in Thermography under V_{oc}-conditions (V_{oc}-ILIT) with one sun illumination gives information about local ohmic shunts. If only minor shunts are present, local variations of the first diode's saturation current (recombination current induced shunts) and the effective lifetime are rather responsible for the visible temperature difference [23, 74]. This is due to the not applied current during measurement, leading to a map of dissipating currents from excited charge carriers rather than from current flow in the actual solar cell under working conditions. Therefore, this method allows to evaluate factors, that have an influence of V_{oc} and on shunt resistance R_{shunt}. Second, scanning electron microscopy (SEM) images of a vertical cross-section through a distinct low performing line are taken and combined with an LBIC line scan, which was taken at the same location.

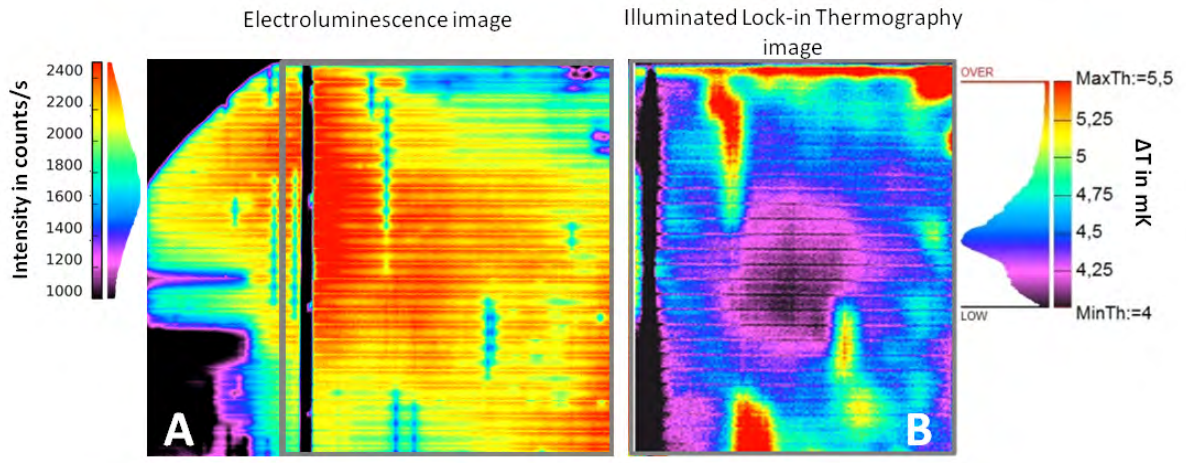

Figure 5.29.: Direct comparison of a selected electroluminescence image area to a thermography image

Starting with the temperature difference image shown in figure 5.29 **B**, which is directly correlated to the highlighted area in **A**, it can be seen that especially where the low performing lines are present, an increased temperature is found. The actual difference is low, about 1-2 mK. This is unusually low, since for PhosTop cells, higher differences were found in the range of a few mK and mostly at the edges of the solar cell. It is assumed, that in this case V_{oc}-ILIT rather gives an increased temperature due to currents from the first diode than actual shunt recombination, which is in good correlation to the electroluminescence image, where visible low performing lines are due to a reduced voltage difference (reduced quasi-fermi level difference). Therefore, from the V_{oc}-ILIT image probably follows, that increased j_{01} currents dissipating heat are present at the low performing lines, reducing the local V_{oc} and R_{shunt}. For further investigation applying dark-LIT under a slight reverse bias would allow to resolve only ohmic shunts (under the actual diode voltage) and remove the influence of j_{01}. This has not yet been done.

A single low performing line from an area with a relatively high luminescence intensity is used since it allows an exact identification. This analysis is carried out in order to understand the electroluminescence images in a better way and gain insights into the degraded FF as well as reduced V_{oc} of Al-LARE solar cells.
In image 5.30 **A**, the selected region is shown with an arrow marking the direction and location of the LBIC line scan at 980 nm and SEM cross-section. In **B** the LBIC linescan is presented, where the distance is given from the edge of the busbar. It shows a slight improvement of the EQE from approx. 0.91 % to above 0.915 % at the location of the low performing line. Furthermore, the variations show a half period compared to the pitch of the rear contacts. This might suggest, that either between or at the emitter edges (two in one period), a small improvement of the EQE can be found. This is an unexpected effect, which is not fully understood yet.
Furthermore, in **C** a SEM image is shown, which demonstrates three contacts on the rear of a Al-LARE solar cell of which the one in the middle is not filled. This was the only non-filled contact, which was found at the exact position of the bad performing line. In the close vicinity (at least 1 cm in either direction of the cross-section) no further unfilled contact was found. At this local opening in **D**, no emitter was visible in a contrast image. In picture **E**, a small area of

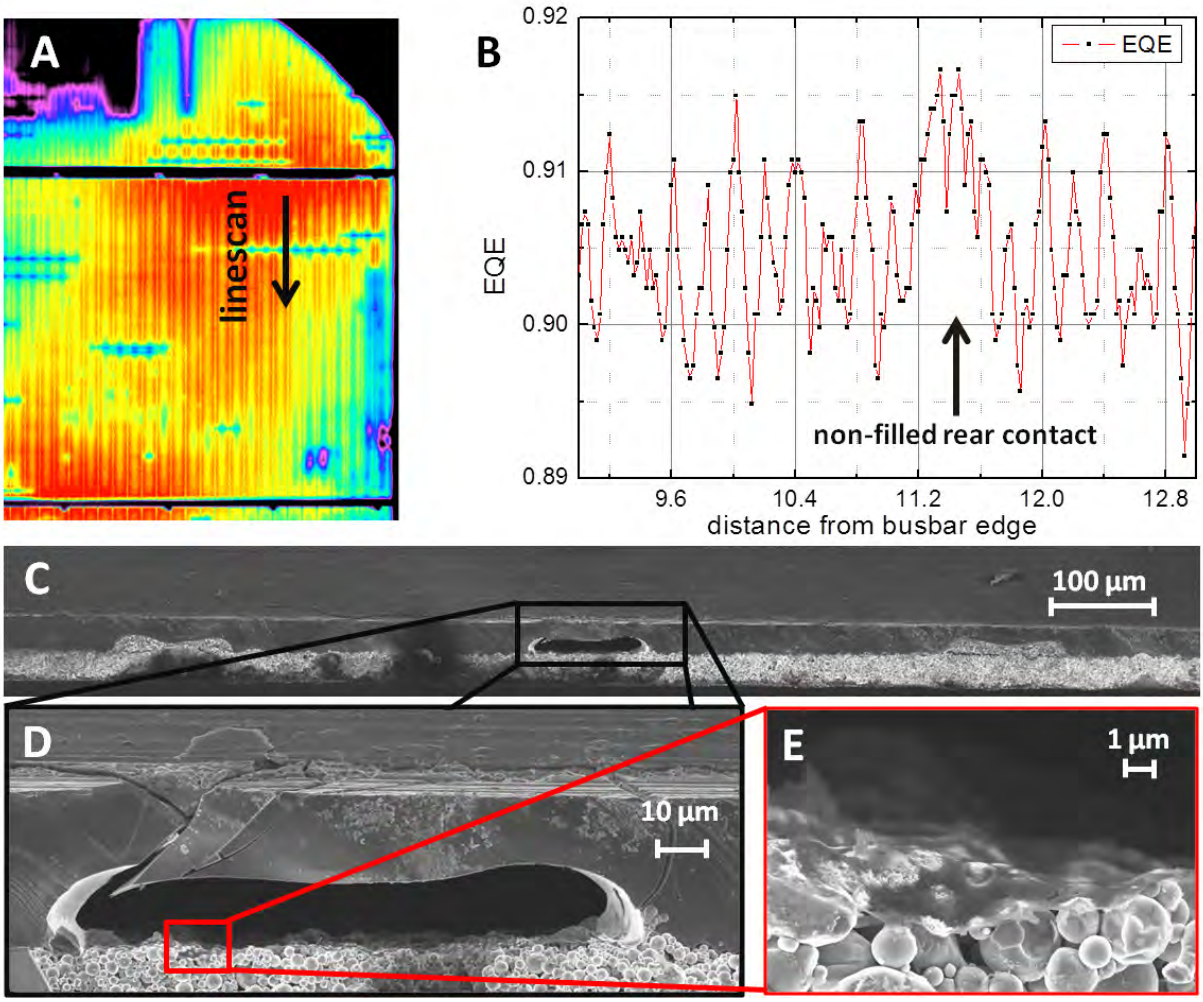

Figure 5.30.: **A,B**: Correlation of an electroluminescence image including a low performing line with a LBIC linescan (980 nm excitation wavelength - taken along the arrow in **A**). In **C** a non-alloyed emitter and not formed contact is visible in between two proper contacts. In **D**, the non-alloyed or contacted opening is shown in higher resolution - no emitter nor eutectic was formed; **E** A thin layer on top of the paste is visible - possibly the eutectic or aluminium (needs further investigation)

the aluminium paste's surface is enlarged, showing a thin layer, which probably is the eutectic or a thin aluminium layer.
Unfilled contacts have been also observed for PERC solar cells and are further discussed and analysed in e.g. [58].

5.3.5.6. Discussion of Al-LARE Solar Cell Results

The overall performance of the fabricated Al-LARE solar cells is low compared to the reference PhosTop solar cell. Similar to the result presentation, the main four IV-characteristics of the

fabricated solar cells are discussed in detail with their influences on the whole performance and possible sources of reduced values.

Fill factor Since the front side of all solar cells in this experiment is equally fabricated, the low values for the FF can be attributed to the rear side. For Al-LARE solar cells, extracted series and shunt resistance are only responsible for a minor reduction of the FF. Incomplete removal of the passivation by the picosecond laser or laser damage can be one main source of high series resistance, since the contact resistance can be increased. This can be a result of thickness variations of the passivation layers/stacks over one wafer or even for each group, resulting in a slightly varying removal quality of the passivation layer. In order to avoid influences by this, an one minute NaOH etch was carried out after local opening, that removed about 1 µm of silicon at the passivation openings. Therefore, opening problems can not be totally accounted for the reduction of the FF.

Furthermore, fitting of selected Al-LARE solar cells and MLM measurements revealed that the total series resistance is not extremely high, reaching only approx. 1 Ωcm^2 or less for fitted IV-curves and for MLM measurements values of 0.75-1.4 Ωcm^2 at MPP. Furthermore, the contact problems can result in locally varying series resistance, which can change the current flow in the cell drastically.

According to the two-diode model, the main source of the reduced FF is j_{02}, which is extremely high compared to the improved PhosTop cell. From approximately 5-20 nA/cm^2 in the latter case, for Al-LARE solar cells values of up to several hundred nA/cm^2 were extracted. High j_{02} values are either a result of edge recombination, which refers to a depletion region that is in direct contact with the surface, and depletion region recombination. Both can occur in Al-LARE solar cells, since the junction is locally alloyed. This can lead to shunts or edge recombination currents at the edge of the contact, when no emitter is formed.

Short-circuit current density A small short-circuit current density increase for Al-LARE solar cells passivated by Al_2O_3/SiNA-SiN_x on the rear side of 0.45 mA/cm^2 was found. The gain in IQE in the long wavelength regime and hence the short-circuit current density gain is in most cases eliminated by the reduced plateau in the visible light range compared to the PhosTop reference. The only exception for this is the Al_2O_3/SiNA-SiN_x passivated Al-LARE solar cell. The reduced plateau is a result of losses due to the lateral diffusion in the bulk of the minority charge carriers to the locally alloyed emitter. Reducing this effect by improving the passivation quality is possible since different drops in the plateau for different passivation stacks are found.

Finally, a blur effect of the inkjet mask during creation of the s-FSF for all solar cells resulted in an increased region of highly doped silicon on the front side. These larger, non-etched back regions surrounding the fingers and busbars reduce the blue response and the overall IQE in all solar cells. Therefore, it can be said, that all solar cells have higher potential.

Open-circuit voltage V_{oc} was expected to have improved due to an enhanced rear passivation by one of the three passivation layers/stacks compared to a direct full area rear contact emitter (PhosTop cell). This was not the case, however the extracted first diode's saturation current density is only slightly reduced compared to the reference. A passivation quality resulting in a j_{01} of approx. 250 fA/cm^2 for the best performing Al-LARE solar cell featuring a SiO_2/SiNA-SiN_x passivation can be calculated using the equations 4.2 and

4.1. The respective surface recombination velocity on a 10 Ωcm n-type bulk can be given using equation 3.12 to approx. 7 cm/s.

It can be suggested from the thermography image, which shows a strong correlation to the electroluminescence image that j_{01} is locally increased at the low performing lines under V_{oc}-conditions and hence, the local V_{oc} and R_{shunt} is reduced.

But from the extracted fits follows that the main source for a high reduction of V_{oc} is the strongly increased j_{02}.

Efficiency Compared to the reference PhosTop solar cell, the main efficiency losses are due to the reduced FF and the relatively low open-circuit voltages, both being limited by j_{02}. By comparing the simulated best performing (also 300 µm emitter spacing) Al-LARE solar cells from section 4.2.2 with the fabricated ones, this results in an overall efficiency loss, assuming a well passivated rear side of j_{01} = 150 fA/cm^2, of approx. 2 % total. The best fitted Al-LARE solar cell was further used to approximate the effect of j_{02}, which resulted for a similar j_{02} as the PhosTop solar cell in an efficiency of 19.7 %. This indicates a high potential, if j_{02} can be strongly reduced.

5.3.6. Conclusion on Al-LARE Solar Cells

Al-LARE solar cells show a gain in j_{sc} of 0.45 mA/cm^2 compared to the reference, which can be attributed to enhanced rear internal reflection. This is in good agreement with the presented simulation in section 4.2.2.

Basically, two main limitations of the Al-LARE solar cell concept can be identified. First, an insufficient improvement of the passivation quality, which resulted in a saturation current density of approx. 250 fA/cm^2 if compared to the unpassivated rear of the reference (370 fA/cm^2). This slight improvement was not sufficient enough to sustain the IQE plateau on a comparable level to the reference. This is due to the needed lateral diffusion of the minority charge carriers to the emitter and contact.
Second and more important, a very high j_{02} due to increased edge recombination and depletion region recombination results in a strongly reduced FF and V_{oc}. This increased j_{02} can be a general problem of the Al-LARE solar cell concept, since two lines can have about the same emitter edge length as a fully alloyed emitter solar cell. The strongly increased j_{02} in combination with a slightly higher series resistance leads to a reduced FF.

In conclusion, the efficiency of Al-LARE solar cells is not expected to outperform the improved PhosTop solar cells as long as j_{02} is not strongly decreased and the series resistance on a comparable level to the PhosTop solar cell. If j_{02} can be strongly reduced and brought on a comparable value to the PhosTop solar cell, an efficiency of up to 19.7 % could be achieved.

5.4. FALCON Solar Cells

The FALCON solar cell concept is similar to the Alu$^+$ solar cell concept presented by Bock et al [72, 75]. The Alu$^+$ concept features a homogeneous FSF on the front side and an amorphous silicon or Al_2O_3/SiN_x passivated, locally by line or point contacted full area aluminium-alloyed rear emitter, which is either contacted by evaporated or screen-printed aluminium. On the contrary, the presented cell concept's front side is based on the improved PhosTop solar cell and therefore features a selective FSF and a front side passivation, which is identical to the one of the improved PhosTop cell. On the rear side, an emitter is fully alloyed and etched back to approx. 2 µm depth, which brings the junction closer to the surface. In section 4.3.2 it was shown, that for a well passivated rear surface this can result in a gain in V_{oc}, j_{sc} as well as in efficiency. For this cell concept, three different rear passivation layers/stacks were used. Similar to Al-LARE solar cells, the rear side was passivated using SiO_2/SiNA-SiN_x, Al_2O_3/SiNA-SiN_x and SiNA-SiN_x passivation layers/stacks. Except for the SiO_2/SiNA-SiN_x rear side passivation, the quality and stability of the passivation layers/stacks on an etched back emitter is analysed in section 5.2.2. Two different processing sequences were carried out, referred to as experiment **A** and **B**, of which either had a dry oxidation after or prior to the full area emitter formation, respectively. The FALCON solar cell concept is depicted in figure 4.9.

5.4.1. Fabrication Sequence

Two different processing sequences are described in this section for the fabrication of FALCON solar cells. Both involve the same steps, but the order has been re-arranged to allow SiO_2/SiNA-SiN_x passivation of the highly doped emitter on the rear. Therefore, in experiment **A** the previously alloyed emitter was exposed to a high-temperature oxidation at 900 °C for about 7 minutes. In experiment **B**, the emitter formation was carried out after the front side passivation by means of a SiO_2/CT-SiN_x passivation stack was completed and hence, the emitter was not exposed to a high temperature step at 900 °C. Therefore, in experiment **B** no SiO_2/SiNA-SiN_x passivation was possible. The process sequence for both experiments is shown in figure 5.31.

s-FSF formation The s-FSF formation was carried out in the same way, as it is described in section 4.1.2 for all PhosTop solar cells. This was followed by a HCl/HF cleaning sequence for experiment **A** and **B**.

Front side passivation (Exp. B only) The surface was first prepared by a standard RCA cleaning sequence, which was then followed by a dry oxidation at a peak temperature of 900 °C for 7 minutes. Subsequently, the deposition of the CT-SiN_x layer (70 nm thickness) was carried out.

Emitter formation and etch back In both experiments, the rear was fully screen-printed with the aluminium paste Al Q and subsequently, after a short drying step, co-fired at a set peak temperature of 840 °C and a belt velocity of 4400 mm/min (sunny side down). In experiment **B**, this has resulted in the emitter profile, which is shown in section 5.2.2.2 figure 5.12 (the samples in section 5.2.2.2 are fabricated in parallel with experiment **B**, while the here presented experiments **A** and **B** were separately fabricated). The aluminium paste was removed in a 37 % HCl solution. Residual lamellas were then removed, while emitter etch back was carried out. This was done in an approx. 20 % NaOH solution at 80 °C. The highly-doped silicon loss was measured by weight differences. Furthermore the

sheet resistance of the emitter was measured. In both experiments, the etch back was carried out, until about 3 to 4 µm were removed and a sheet resistance range ranging from 35 to 55 Ω/sq was obtained. The sheet resistance was measured on samples that were fabricated in parallel to experiment **B** by using a four-point probe. Finally, all cells were cleaned by a HCl/HF cleaning sequence which was followed by a Piranha cleaning step.

Front (+rear) side passivation (Exp. A only) For experiment **A**, the front side passivation was prepared by another cleaning step, involving an RCA cleaning. Subsequently, dry oxidation at 900 ℃ for 7 minutes was carried out. The front side passivation was then finalized by a direct PECVD silicon nitride deposition, leading to a CT-SiN_x layer of 70 nm thickness. For one group, the SiO_2 layer was used as passivation on the rear, as well.

Rear side passivation & local opening Depending on the final rear passivation layer/stack, the cells were either covered by means of an aluminium oxide layer of 15 nm thickness (Exp. **A** and **B**) or directly covered by a 150 nm thick SiNA-SiN_x layer, which led to a SiO_2/SiNA-SiN_x (Exp. **A**), SiNA-SiN_x (Exp. **B**) and Al_2O_3/SiNA-SiN_x (Exp. **A** and **B**) rear surface passivation. The rear was opened in the next processing step by using a Coherent Talisker Ultra picosecond laser at a wavelength of 532 nm, an intensity of 1.22 W and a fluence of approx. 470 mJ/cm^2. The laser parameters were adapted in order to optimize the opening results for each layer/stack. The opening width was set to 100 µm with a total pitch of 1.16 mm. This led to a contacted fraction of about 11.6 % on the rear side after the solar cell was finished. Then, the cells were brought into 22 % NaOH at 80 ℃ for 1 minute in order to remove residual passivation particles in between the contact openings and further remove the top of the potentially laser-damaged silicon surface.

Metallization Finally, the metallization was carried out. The front side was screen-printed with a silver paste, which was then followed by a full area screen-printing of the rear with the aluminium paste Al O in the case of experiment **A** and Al Q in experiment **B** (similar pastes from the same manufacturer). After a short drying step in both experiments, co-firing was carried out at different set peak temperatures and belt velocities. In experiment **A**, the co-firing parameters were set to a peak temperature of 840 ℃ and a belt velocity of 4400 mm/min, while in experiment **B** these parameters were set to 850 ℃ and 5400 mm/min, respectively. Since the etch-back resulted in an emitter, which was about 2 µm deep, at the local openings, re-alloying of aluminium took place, that resulted in an emitter depth of roughly 5 µm underneath the openings (see figure 5.35). Therefore, the FALCON solar cell features a selective emitter.

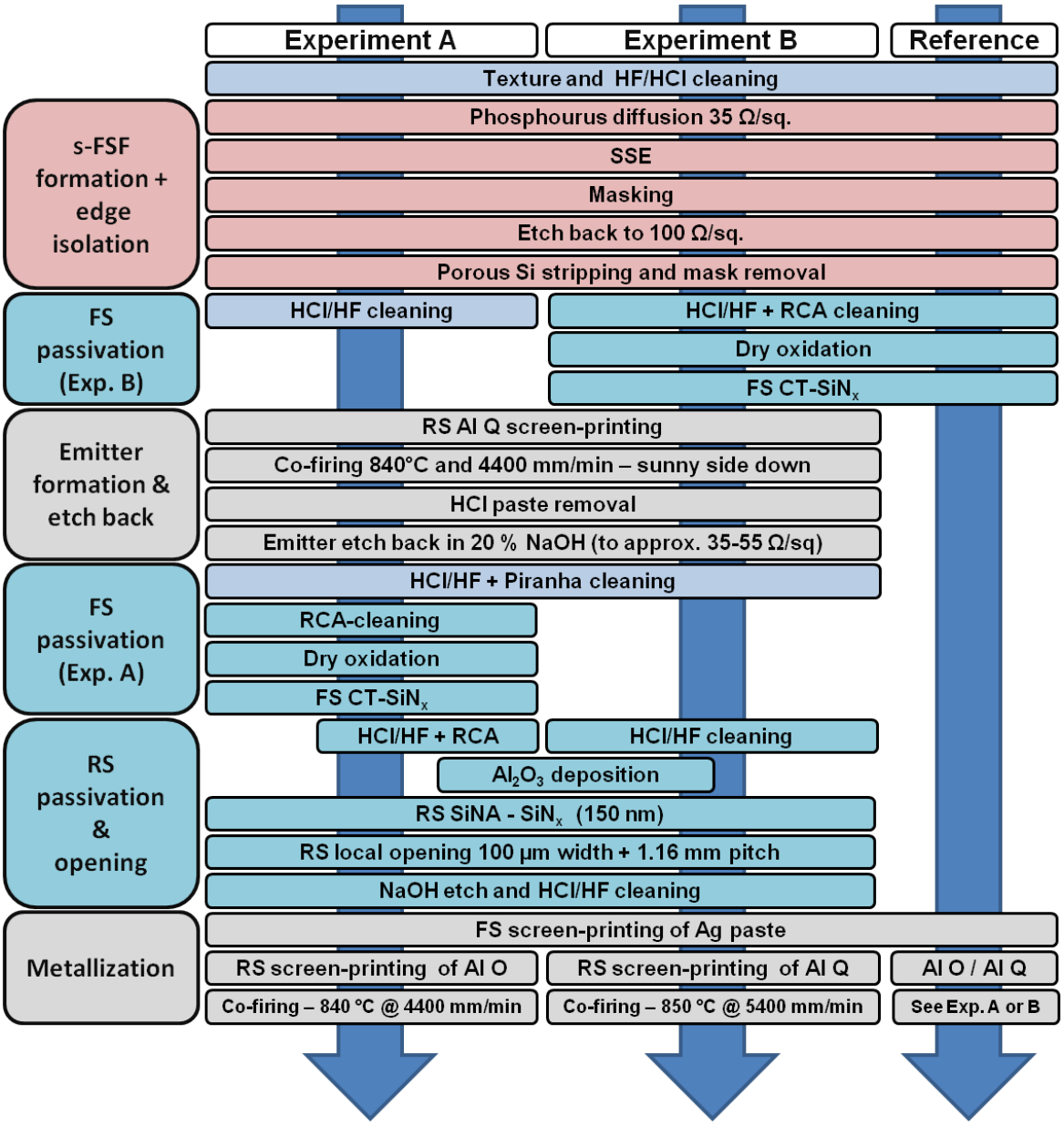

Figure 5.31.: Processing sequences of the reference PhosTop solar cells and FALCON solar cells with a high-temperature dry oxidation before (Experiment **A**) and after (Experiment **B**) aluminium emitter formation

5.4.2. IV-Results

This section presents the obtained IV-parameters such as the efficiency, j_{sc}, V_{oc} and the FF for FALCON and the reference improved PhosTop solar cells. The obtained results are shown in table 5.3.

Table 5.3.: IV results of FALCON and PhosTop solar cells for experiment **A** and **B** corrected with the method described in section 3.1

Exp	Cell Concept	Value	FF in %	j_{sc} in mA/cm^2	V_{oc} in mV	η in %
A	Improved PhosTop cell (Reference)	average	78.5	37.6	646.2	19.1
		best cell	78.8	37.8	647	19.3
A	FALCON cell (SiO_2/SiNA-SiN_x pass.)	average	76.6	37.9	640.8	18.6
		best cell	76.6	38.3	642.9	18.9
A	FALCON cell (Al_2O_3/SiNA-SiN_x pass.)	average	76	37.3	639.8	18.1
		best cell	75.4	37.8	640.8	18.3
B	Improved PhosTop cell (Reference)	average	79.8	37.4	647.6	19.3
		best cell	80	37.5	648.2	19.4
B	FALCON cell (Al_2O_3/SiNA-SiN_x pass.)	average	76	36.7	634.8	17.7
		best cell	76.8	37	634.2	18
B	FALCON cell (SiNA-SiN_x pass.)		69.6	37.2	599.9	15.5

Fill factor

Experiment A A FF reduction of approx. 2 % for the FALCON compared to the PhosTop cells is measured. The FF of FALCON solar cells featuring an Al_2O_3/SiNA-SiN_x passivated rear side is even further decreased to approx. 76 % , which results in a moderate efficiency loss.

Experiment B For solar cells fabricated in experiment **B**, the FF is very high for the reference, reaching 80 %. Al_2O_3/SiNA-SiN_x passivated FALCON solar cells also experience a slight improvement of the FF of approx. 1 % compared to the same rear passivated FALCON solar cells that were fabricated in experiment **A**. The FALCON solar cell featuring a SiNA-SiN_x passivated emitter shows a strong loss in FF, falling below 70 %.

Short-circuit current density

Experiment A The obtained short-circuit current density results show an increase from a maximum 37.8 mA/cm^2 for the best performing reference to 38.3 mA/cm^2 for the best FALCON solar cell passivated by means of a SiO_2/SiNA-SiN_x stack. Interestingly, FALCON solar cells passivated by Al_2O_3/SiNA-SiN_x show no improvement in the short-circuit current density compared to the reference.

Experiment B Al_2O_3/SiNA-SiN_x passivated FALCON solar cells show a decrease in j_{sc} compared to the reference, which is also visible for experiment **B**. In the latter case, this reduction is even more pronounced, leading to approx. 0.5 - 0.8 mA/cm^2 lower values compared to the reference PhosTop cells. The measured j_{sc} values for all solar cells are shown in figure 5.32.

Open-circuit voltage

Experiment A The open-circuit voltage decreases from approx. 647 mV for the reference down to below 640 mV for the Al_2O_3/SiNA-SiN_x passivated FALCON solar cell. The obtained V_{oc} values for SiO_2/SiNA-SiN_x FALCON solar cells are low too, reaching a maximum of almost 643 mV.

Experiment B Compared to experiment **A**, an increase of approx. 1 mV is found for the

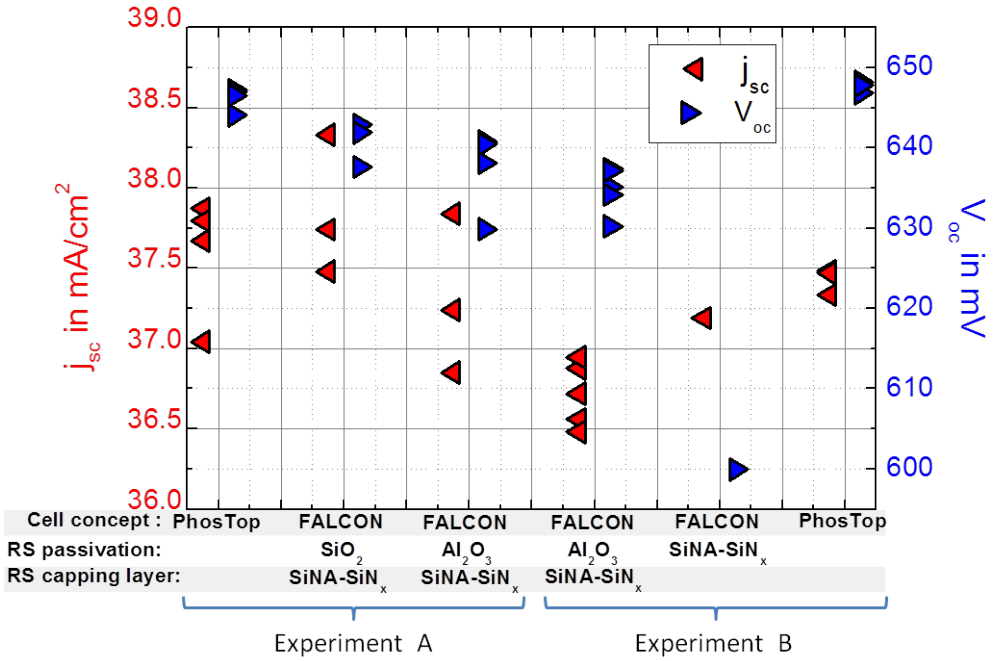

Figure 5.32.: The distribution of measured j_{sc} and V_{oc} of reference and differently passivated FALCON solar cells

best performing PhosTop cells in experiment **B**. The Al_2O_3/SiNA-SiN_x passivated FALCON solar cells show a decrease in the maximum obtained V_{oc}, down to an average of roughly 634 mV. Only one FALCON solar cell featuring a SiNA-SiN_x rear side passivation was finished, which resulted in a maximum obtained V_{oc} of below 600 mV.

Efficiency

Experiment A Although a SiO_2/SiNA-SiN_x FALCON solar cell showed the highest short-circuit current density and hence could allow a strong improvement of the solar cell performance, the efficiency is mainly limited by a moderate FF and V_{oc}, which results in a maximum efficiency of 18.9 %. Therefore, no improvement to the sawn reference improved PhosTop solar cell can be found, which resulted in a best performing efficiency of 19.3 %. Al_2O_3/SiNA-SiN_x FALCON solar cells performed even less successful, reaching a best performing of 18.3 %.

Experiment B Since it was assumed, that the performance of experiment **A** was reduced due to the high-temperature step after the formation of the emitter, experiment **B** was carried out. The references, which were fabricated in both experiments in the same way, reached a maximum efficiency of 19.4 %. While for the best performing Al_2O_3/SiNA-SiN_x FALCON solar cells 18 % was obtained, in the case of Al_2O_3/SiNA-SiN_x passivation the efficiency dropped down to 15.5 %.

The best performing rear passivation for FALCON solar cell of both experiments **A** and **B** is SiO_2/SiNA-SiN_x, reaching up to 18.9 % efficiency. A high j_{sc} of 38.3 mA/cm^2 was obtained, which results in an approx. 0.5 mA/cm^2 improvement compared to the sawn reference PhosTop

cell. Al_2O_3/SiNA-SiN_x passivated FALCON solar cells showed no improvement in j_{sc} compared to the reference, although the enhanced internal reflection properties should allow a higher j_{sc}. Therefore, increased losses are present, which lead to a FF below 76 %.

5.4.3. Advanced Characterization and Discussion

FALCON solar cells were further analysed by using different characterization methods. Starting with two-diode model fitting of selected FALCON and reference PhosTop solar cells, more parameters were extracted from the measured light-IV curve, such as series resistance, shunt resistance, j_{01} and j_{02}. This is followed by an investigation of the performance of FALCON solar cells by electroluminescence and spectral response measurements. Furthermore, the contact formation on the rear was analysed using SEM imaging. This is followed by an evaluation of additional series resistances contributions due to the locally contacted emitter. Subsequently, a discussion on the high temperature treatment effect on the emitter is carried out. Finally, the obtained information is discussed.

5.4.3.1. Two-Diode Fits of Selected FALCON Solar Cells

By using the two-diode model, selected solar cells of experiment **A** and **B** were fitted. The fits are shown in figure 5.33. The extracted parameters are discussed and furthermore shown in table 5.4.

j_{01} None of the fitted IV-curves of the FALCON solar cells showed an improvement of the j_{01}, which would indicate a gain in emitter and passivation quality compared to the full metallized rear of a improved PhosTop solar cell. This is in good agreement with the result of the in parallel fabricated samples shown in section 5.2.2.2 that indicate no improvement of the passivated to the unpassivated rear side for slightly etched back emitters. This is due to the strong field-effect passivation of the highly doped emitter. From the extracted j_{01} values follows, that the passivation quality was not improved, but held on a comparable level at least for the FALCON solar cell passivated by SiO_2/SiNA-SiN_x. The lowest level, a j_{01} of $\approx$ 410 fA/cm^2 was extracted from the fit for FALCON passivated by SiO_2/SiNA-SiN_x.

j_{02} The fits indicate an increase of the second diode's saturation current density from 5 nA/cm^2 for the PhosTop solar cell up to roughly 25 nA/cm^2 for a well performing FALCON solar cell. While the j_{02} values for well performing FALCON solar cells is in an acceptable magnitude, extremely high values of up to 210 nA/cm^2 are found for bad performing FALCON solar cells e.g. the one featuring a passivated rear by means of SiNA-SiN_x.

The bad performance of the FALCON solar cell passivated by SiNA-SiN_x is due to inversion layer shunting.

Series resistance For the reference improved PhosTop solar cell, a series resistance R_s of 0.6 Ωcm^2 is extracted, while the series resistance for FALCON solar cells is increased, reaching up to 1 Ωcm^2. For further discussion on series resistance see section 5.4.3.5.

Shunt resistance All obtained values are on a very high level. The shunt resistance is therefore not limiting the solar cell performance.

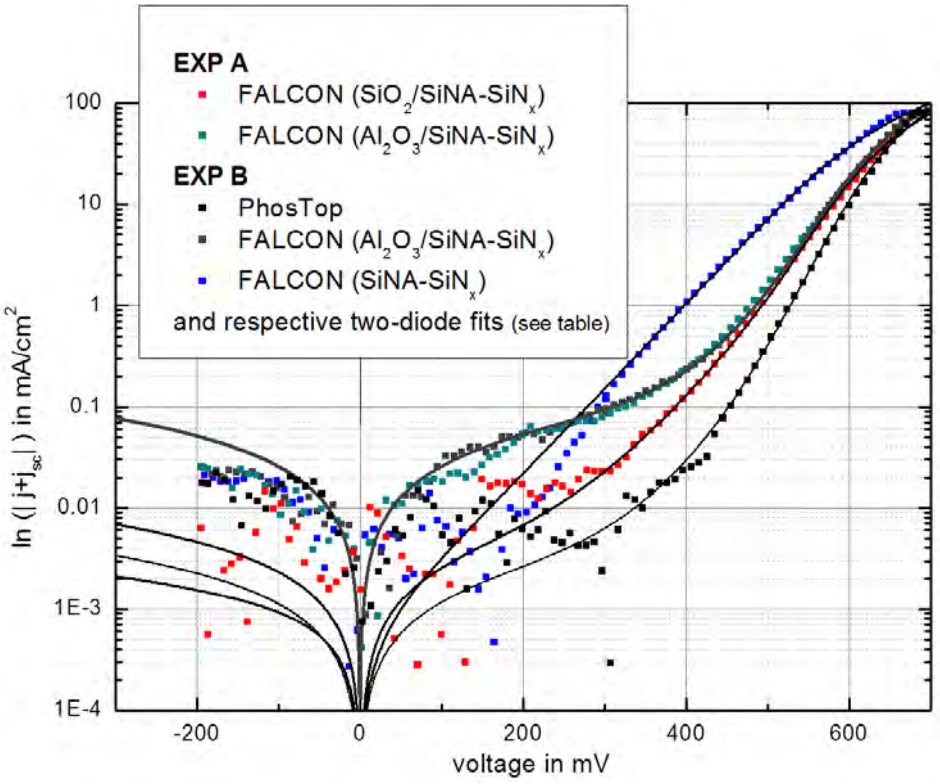

Figure 5.33.: Two-diode model fits of selected FALCON solar cells from both experiments and the best PhosTop reference from experiment B

Table 5.4.: Two-diode model parameters extracted from fitting of selected PhosTop and FALCON solar cell IV characteristics

EXP	Cell Concept		FF in %	j_{sc} in mA/cm^2	V_{oc} in mV	η in %	j_{01} in fA/cm^2	j_{02} in nA/cm^2	R_{series} in Ωcm^2	R_{shunt} in Ωcm^2
A	FALCON cell (SiO_2/SiNA-SiN_x pass.)	Cell	76.6	38.3	643.2	18.9				
		Fit	76.7	38.3	643.7	18.9	410	24	0.9	4.4E+04
B	FALCON cell (Al_2O_3/SiNA-SiN_x pass.)	Cell	76.8	37.1	634.3	18.1				
		Fit	76.9	37.1	634.1	18.1	580	28	0.8	3.90E+03
B	FALCON cell (SiNA-SiN_x pass.)	Cell	69.6	37.4	600.6	15.6				
		Fit	69.8	37.4	600.9	15.7	800	210	1.0	1.8E+05
B	PhosTop cell (best solar cell)	Cell	80.0	37.4	648.6	19.4				
		Fit	80.1	37.4	648.6	19.4	385	5	0.6	9.0E+04

5.4.3.2. Electroluminescence

In this section, typical electroluminescence images of the FALCON solar cells are presented. In figure 5.34, on the left hand side, an electroluminescence image is presented from experiment **A**. The selected FALCON solar cell features a SiO_2/SiNA-SiN_x passivated rear and has been the best performing one, reaching a short-circuit current density of 38.3 mA/cm^2 and a V_{oc} of

643 mV. A reference PhosTop solar cell from experiment **B** can be found in figure 5.26 **A**.

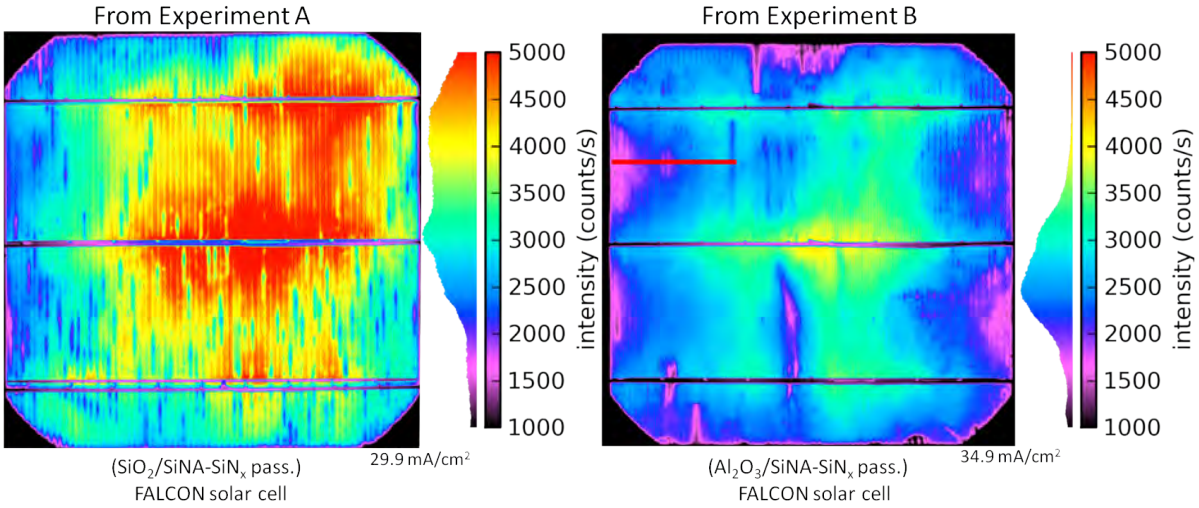

Figure 5.34.: Electroluminescence images of the best FALCON solar cell (experiment **A**), whose rear side is passivated by means of SiO_2/SiNA-SiN_x and a selected Al_2O_3/SiNA-SiN_x passivated FALCON solar cell from experiment **B**. In **B**, a highlighted line is shown, along which a cross-section was carried out and is analysed using the SEM in the next section.

The electroluminescence image 5.34 of the solar cell on the left hand side shows strong intensity reductions in some regions that correlate to the rear side geometry of the contacts and therefore indicates a problem with the formation of the contact on the rear side. The emitter was previously alloyed all-over the rear with an emitter depth after the etch back of roughly 2 µm. The visible lines probably indicate a contact issue on the rear. These lines are also visible for low excitation current densities (and hence low applied voltages), which leads to the conclusion, that these are not an effect of series resistance.
In the second image on the right hand side in figure 5.34, a typical FALCON solar cell from experiment **B** is given, showing although taken at a higher applied current density of 34.9 mA/cm^2 compared to 29.9 mA/cm^2, a reduced intensity. This is due to the fact, that the performance of the by Al_2O_3/SiNA-SiN_x passivated FALCON solar cells was lower compared to FALCON solar cell featuring a SiO_2/SiNA-SiN_x passivated rear side.

5.4.3.3. SEM Contact Analysis

A cross-section through the low responding region in figure 5.34 was done using a Disco DAD 341 dicing saw. The analysed cross-section is highlighted in figure 5.34 as a red line. Within this region, most rear contacts were found to show strong contact problems, although an emitter has been formed. This is in contrast to the contact formation for Al-LARE solar cells, in which in most observed cases, no emitter formation was found for non-contacted contacts.
In image 5.35 **A**, the pre-alloyed emitter above the passivation is clearly visible due to the contrast in the image. The emitter is approx. 1.5-2.5 µm thick, which is in good agreement with the expected etched back depth. The alloyed emitter during contact formation in the right part of image 5.35 **B** is in fact about twice as deep (approx. 5 µm), showing depth variations.

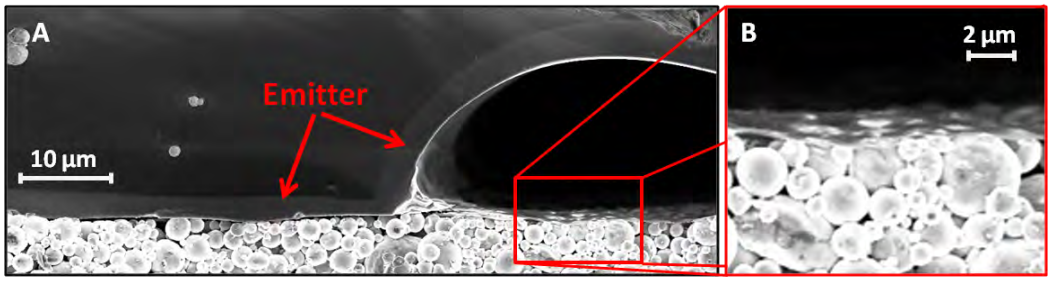

Figure 5.35.: SEM images of a cross-section through a low luminescence region in the right electroluminescence image along the highlighted line (see figure 5.34). The etch back emitter is visible in image **A** as well as a second, during co-firing of the contact alloyed emitter. A enlarged region in the area, where no eutectic was formed, is shown in **B**

Similar to SEM images of Al-LARE solar cells, the bottom surface within non-formed contacts was found to be covered with a thin layer (see image 5.35 **B**). Possibly, these are residuals of the eutectic or a thin aluminium layer, that formed during co-firing. Since the surface of the hole seems to be covered with a thin eutectic, which is also connected to the aluminium paste on the rear, it can be assumed that a very small contact was nevertheless formed.

5.4.3.4. Spectral Response

The spectral response was measured using the spectral response measurement setup, which was presented in section 3.2. For each solar cell concept and experiment, the IQE and reflectivity is given as a function of the wavelength, which ranges from 350 nm up to 1200 nm. Non-physical data points or data points being distinct outliers were removed, since these points are a result of problems resulting from the measurement assembly.

The IQE shows basically two effects. First, a gap and different slope between the plateaus of the internal quantum efficiency for wavelengths ranging from 400 nm to 1000 nm is visible, if the solar cells from experiment **A** and **B** are compared. This difference is a result of a reduced effective SRV due to the enlarged highly doped silicon caused by the earlier mentioned blur effect during etch back of the FSF. Second, the increase in the IQE for photons with wavelengths above 1000 nm is more pronounced for experiment **A** than it is for solar cells from experiment **B**, if compared with their respective reference PhosTop solar cell.

Interestingly, the measured reflectivity in the long-wavelength regime above 1000 nm (direct reflected and front escape) shows a strong improvement for the in experiment **A** fabricated solar cells from 23 % up to almost 42 %. In experiment **B**, the increased reflectivity is only reaching 33.7 %, whereas the reflectivity for a in parallel fabricated PhosTop cell was close to 20 %. Therefore, it is possible to account for the difference in the reflectivity at 1200 nm of experiment **A** and **B** partly by the different front side escape, which can be a result of an increased free carrier absorption (FCA) in the enlarged highly doped regions of the s-FSF in experiment **B**. FCA basically refers to intra-band transitions of charge carriers due to especially long wavelength photons, which then release their excitation energy by emitting phonons. The gap in the IQE plateau between the PhosTop and FALCON solar cells from experiment **B** is probably a result of reduced diffusion lengths or deteriorated collection of minority charge carriers, whereas the first can be due to a twice fired front side passivation.

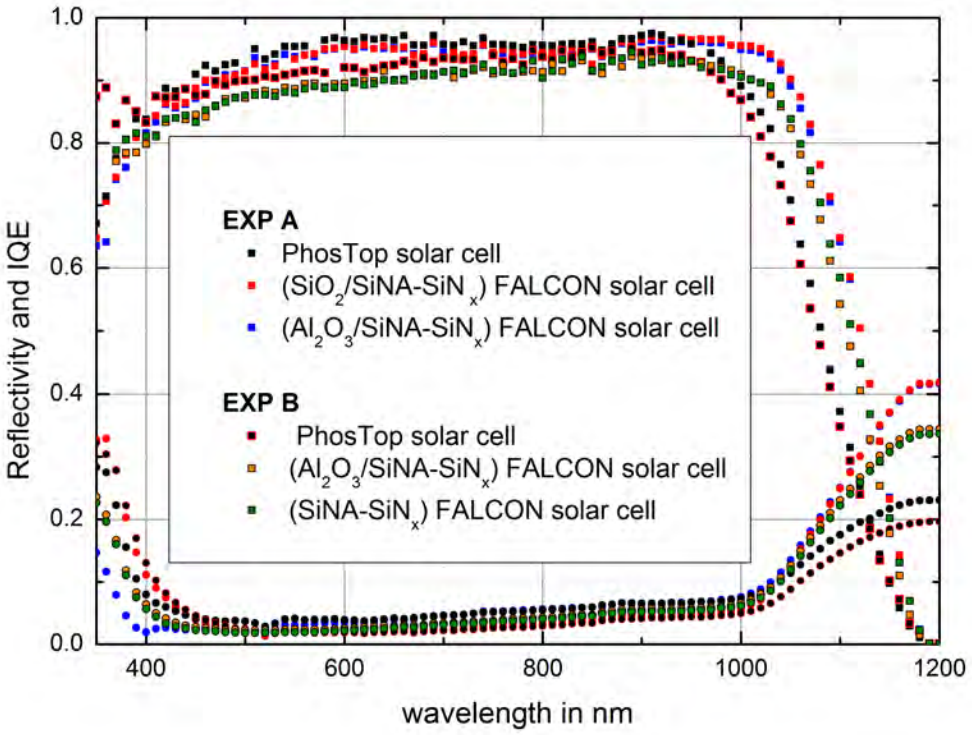

Figure 5.36.: Calculated IQE and measured reflectivity of selected FALCON solar cells and a reference PhosTop solar cell

5.4.3.5. Analysis of Additional Series Resistance

In this section, the influence on the general performance and the increase of the series resistance due to increased lateral series resistance in the emitter $R_{lat,\ emitter}$ and increased contact resistance $R_{contact}$ is analysed and discussed. For the PhosTop solar cell a R_s of approx. 0.6 Ωcm^2 was extracted from fits, which is slightly lower than the values obtained from the MLM measurements presented in section 5.3.5.4 for the PhosTop solar cell (same reference as for FALCON solar cells from experiement **B**). For the FALCON solar cells, increased values were extracted of up to 1 Ωcm^2, while using the MLM method (not presented) slightly higher values were obtained. This difference compared to the reference PhosTop solar cell is analysed.

The contact resistance was analysed using the transmission-line method (TLM) [76]. Besides an estimation of the specific contact resistivity ρ_c, it allows an accurate determination of the emitter sheet resistance in between the two contacted contacts.
In experiment **A**, FALCON solar cells were fabricated, that featured a locally opened passivation, on which a rear side grid with 1.16 mm pitch and 200 µm wide fingers was screen-printed and subsequently co-fired. Therefore, the rear was not fully covered with aluminium paste. This allows to measure the specific contact resistivity of the rear contacts on p^{++} aluminium doped silicon. The test structure was separated using a dicing saw, which led to a width of 1 cm with equally spaced contact fingers in a distance of 1.16 mm. The contact width was estimated to be 120 µm for a line opening width of 100 µm.
Several measurements were carried out, which resulted in an average specific contact resistivity of (3.8 ± 1.7) $m\Omega cm^2$and an underlying emitter sheet resistance of (35±8) Ω/sq. Some measured

data resulted in a negative specific contact resistivity and hence were excluded from the average. This was probably due to an unfilled contact in the contact structure to be measured.
By using equation 2.19, the series resistance contribution of the contact resistance is evaluated, if the unit area A_{unit} equals 1160 µm^2 and the contact area $A_{contact} \approx 120$ µm^2 (assuming equal lengths of 1 µm). The contact resistance was calculated to be $R_{contact} \approx 37$ mΩcm^2 and therefore only a minor contribution to the increased series resistance of FALCON solar cells. For a contact, which is only contacting the emitter with a tenth of the area (e.g. 12 µm), the contact resistance is tenfold and therefore has a strong influence to the total series resistance, if all contacts have a small contact area, which is definitely not the case. Assuming 10 % of the contacts not to have formed properly (contact width of 12 µm) would only result in an increase of 36.7 mΩcm^2. The percentage of narrowed contacts is difficult to estimate, but assuming 10 % has shown no strongly increased contact resistance.

The increased lateral series resistance in the emitter compared to the PhosTop solar cell is further analysed by using equation 2.20. A PhosTop solar cell has a negligible lateral emitter series resistance, since after reaching the emitter, charge carriers are directly able to reach the metallization. For FALCON solar cells this is not the case and charge carriers need to be conducted through the emitter, experiencing a series resistance.
This contribution is calculated for perfectly formed rear contacts, assuming a contact width w_F of 120 µm and finger pitch d_F of 1.16 mm. The resulting emitter lateral series resistance is 35.3 mΩcm^2, if a sheet resistance of 35 Ω/sq is used. This is a small contribution. In the case of a non-contacted line, the contact spacing is doubled and hence 2.32 mm. This leads almost to a tenfold increase to 0.35 Ωcm^2, which is severely contributing to the total series resistance, if only every second line would be properly contacted.
Assuming a 10 % failure in proper contacting, this again allows to reduce this contribution strongly to a tenth and hence, this contribution is small, as well.

For a perfect rear geometry, the additional series resistance contributions from the lateral emitter and contact resistance are only together resulting in approx. 72 mΩcm^2. But a difference of roughly 0.3-0.4 Ωcm^2 was found between the series resistance from Al-LARE and PhosTop solar cells, which leads to the suggestion, that contacting problems are probably responsible for the further increase (assuming the same front and bulk series resistances).

5.4.3.6. Discussion of the High Temperature Treatment Effect on the Emitter

Two different experiments were previously presented of which in one the full area aluminium alloyed emitter experienced a high temperature oxidation for 7 minutes (experiment **A**), whereas the other was not exposed to high temperature treatment (experiment **B**).

Schmidt et al. [64] demonstrated, that the minority charge carrier lifetime in highly-aluminium doped silicon layers is in the order of 130 ns for an aluminium doping concentration of approx. $2{\cdot}10^{18}$ cm^{-3}, which can be assumed to be even lower in the presented solar cell emitter, since the paste also consists of boron, which allows an higher doping concentration. Furthermore, due to the formation of aluminium-oxygen complexes during high temperature treatment above 900 °C, a degradation of the minority charge carrier lifetime can be assumed after high temperature treatment. Note, that the high temperature during co-firing is not leading to a degraded minority charge carrier lifetime, since the exposure time is only a couple of seconds. It was reported by Bock et al. [77], that the concentration of oxygen in the used material is detrimental. This is due to a dependence of the oxygen contents in the used materials on the degradation of the minority charge carrier lifetime after high temperature treatment. From this low minority

charge carrier lifetime, a efficiency limit of approx. 21 % and maximum V_{oc} of 670 mV was suggested [64].

Interestingly, the best performing FALCON solar cells were passivated by means of SiO_2/SiNA-SiN_x on the rear side and hence experienced a high temperature oxidation at 900 °C. The base material can be assumed to have relatively high oxygen contents, as well, since it was Czochralski-grown n-type material.
The profile of the emitter in experiment **A** might have been changed, as well. Since the diffusion constant (diffusivity) of aluminium is roughly one order of magnitude larger than it is for boron [30] at high temperatures in silicon. Even lower, the diffusion constant for phosphorus is roughly one to two magnitudes smaller than the one of aluminium. In phosphorus diffusion, a high temperature drive-in step is common and hence, high temperature can change the profile of the aluminium emitter as well. This has not been further investigated.

5.4.3.7. Discussion of FALCON Solar Cells

FALCON solar cells featuring different rear side passivation layers and stacks were presented. Two similar process sequences for the fabrication of FALCON solar cells were carried out, of which one involved a high temperature treatment after the emitter was alloyed (experiment A) and a second, where the emitter was not exposed to a high temperature treatment (experiment B). Although these experiments were carried out separately, the results are of similar nature.

Fill factor For the best FALCON solar cell featuring a SiO_2/SiNA-SiN_x rear side passivation, the FF was slightly reduced by approx. 2.2 % compared to the reference from experiment **A**. This reduction can be attributed to local contact formation problems, as the one presented for another cell in figure 5.35 and an increased j_{02}. The contact formation problems result in local variations in series resistance due to higher contact resistance. The series resistance influence was discussed in section 5.4.3.5 and should have only a moderate effect on the FF. The reduction due to the increased series resistance is approximated using the two-diode model and a R_s of 0.6 mΩcm^2 to be 1.5 %.

Short-circuit current density An increase of approx. 0.5 mA/cm^2 compared to the PhosTop solar cell was found for a FALCON solar cell featuring a SiO_2/SiNA-SiN_x passivated rear. The increased internal reflection led to an improved IQE in the long wavelength regime.

FALCON solar cells fabricated in experiment **B** showed a decrease in the short-circuit current density, while passivation quality was deteriorated, especially in the case of SiNA-SiN_x passivation on the rear side. This drop, which is also visible if Al_2O_3/SiNA-SiN_x passivated FALCON solar cells from experiment **A** and **B** are compared, is a result of decreased internal reflection, which can be seen in the respective reflection curves (assuming the same front escape). Another explanation for this reduced reflectivity on the rear is the blur effect of the mask during s-FSF formation leading to enlarged highly doped regions, which in turn results in increased free carrier absorption in this region.

In the simulation that is presented in section 4.3.1, a current density gain of 1 mA/cm^2 for a well passivated rear ($j_{01} \approx 150$ fA/cm^2) was found, which could not be realized in the fabricated solar cells. This is possibly due to a non improved rear side quality, which assumed a rear internal reflectivity of 95 %. Therefore, the difference in internal reflection between fullly metallized and locally metallized solar cells is assumed to be too big in the simulation, while experimental data suggests that it is smaller, since a maximum gain of 0.5 mA/cm^2 was found.

Open-circuit voltage Even for the best FALCON solar cells passivated on the rear by means of SiO_2/SiNA-SiN_x, a reduced V_{oc} value is found compared to the reference. About 3 - 4 mV are lost, assuming a similarly well performing front side as the PhosTop solar cell. This is also in good agreement with the slightly increased j_{01} value (extracted from the fit) compared to the reference and the results presented in 5.2.2.

If compared to the simulation presented in section 4.3.1, the simulated V_{oc} is higher than the measured V_{oc}. The reason for this is the assumed j_{01} in the simulation, which is at least doubled in the real solar cell.

For FALCON solar cells passivated on the rear by Al_2O_3/SiNA-SiN_x and SiNA-SiN_x, an improvement in V_{oc} is only found, if j_{02} and j_{01} together improve strongly to a slightly lower level compared to the reference. Assuming a similar j_{02} for both, the FALCON and PhosTop solar cell, still no improvement in j_{01} is found, since passivation of the p-type bulk is not improved if compared to the field-effect passivation provided by the highly doped emitter. Therefore, effective surface recombination velocities are on a lower level and have not been improved due to the etch back and passivation.

Efficiency The reduction in efficiency can be attributed to a not improved, even slightly reduced rear side passivation quality of the emitter. This allows a reduced efficiency compared to the reference of 0.5 % to 18.9 % for the best FALCON solar cell. Mainly, the increased series resistance reducing the FF, while further a slightly higher j_{01} and j_{02} are responsible for a reduction in V_{oc} and FF.

Furthermore, the high temperature treatment was not resulting in a degraded emitter quality, since j_{02} and the measured V_{oc} was not strongly reduced when comparing experiment **A** and **B**.

5.4.4. Conclusions on FALCON Solar Cells

The best performing FALCON solar cell reached an efficiency of 18.9 % and a short-circuit current density of 38.3 mA/cm^2. Compared to the reference PhosTop solar cell, this corresponds to an improvement of 0.5 mA/cm^2, which is a result of enhanced internal reflection and hence an increased IQE in the long-wavelength regime. This gain in j_{sc} could be further increased by optimizing the silicon nitride thickness and thereby increase the reflection for near infrared wavelengths.

For the best FALCON solar cells, the FF and V_{oc} were reduced compared to the reference, which was a combined result of an increased j_{01}, j_{02} and R_s. The first, an increased first diode's saturation current density is a result of a not improved emitter passivation compared to the non-etched back emitter of the PhosTop solar cell. That is in good agreement with the results of the emitter passivation presented in section 5.2.2, in which it was concluded that the field-effect passivation of the non-etched back emitter is leading to a lower effective SRV compared to the etched back and passivated emitter.
In principal, a large gain in V_{oc} could be possible as the simulation indicates in section 4.3.2, if the first and second diode's saturation current can be reduced. Especially, a reduced j_{01} would allow a lower rear SRV. But an increase in passivation quality and hence a reduction in j_{01} on a highly doped etched back emitter is probably not possible, as the experiment in section 5.2.2 suggests since the best available passivation layers and stacks were used there.
The FF reduction due to increased series resistance could be reduced to a value below 0.1 Ωcm^2 if the rear side would be perfectly contacted.

In comparison to the Al-LARE solar cells, no drop in the plateau compared to the reference is found for FALCON solar cells. This is a result of the full rear emitter, which reduces the loss compared to a higher effective SRV in the case of Al-LARE solar cells.

An industrial realization of this cell concept would require a reduction of the needed processing steps and a further increase in efficiency. Assuming a comparable performance to the PhosTop solar cell in FF and V_{oc}, but with a short-circuit current density gain of 1 mA/cm^2, a maximum efficiency of 19.9 % would probably be possible.

6. Summary

This diploma thesis was focused on enhancing the rear side performance of the improved PhosTop solar cell concept by means of dielectric rear side passivation and reduction of the highly doped emitter area. Stack systems and passivation layers were applied on lowly doped n-type silicon bulk and highly doped aluminium p-type emitters in order to reduce the effective rear surface recombination velocity and hence improve the open-circuit voltage. Furthermore, using a dielectric rear passivation leads to an improved internal reflection on the rear side, which results in a short-circuit current density gain. Three different solar cell concepts were realized. Besides the improved PhosTop solar cell, which is representing the reference, the Al-LARE solar cell featuring a passivated n-type bulk and locally alloyed emitter is presented. Furthermore, the FALCON solar cell is realized, which exhibits a full area alloyed and etched back emitter that is passivated and locally contacted.

n-type silicon substrates were passivated using different layers and stacks of which Al_2O_3/SiNA-SiN_x, SiNA-SiN_x and CT-SiN_x passivation performed best after a firing step and featured effective lifetimes of up to 9.5 ms. In the contrary to highly doped n-type silicon, the SiO_2/SiNA-SiN_x passivation on n-type substrates showed a severe firing instability for temperatures above 800 °C.

The characterization of the emitter formed by three different aluminium pastes revealed very low emitter saturation current densities in the range of 150 to 180 fA/cm^2, showing further no influence on the set firing peak temperature. The passivation of the etched back emitter was not found to be on a satisfactory level on samples that featured an etched back emitter, which is thicker than 1.5 µm, being below the passivation due to the field-effect of the non-etched back emitter. Compared to the fully alloyed and metallized rear side of the PhosTop solar cell, no improvement of the rear could be made by using different passivation layers and stacks.

Al-LARE solar cells were simulated using PC2D, a novel two-dimensional simulation. The simulation predicted a possible short-circuit current density gain of 0.5 mA/cm^2 for an emitter and contact width of 100 µm and emitter spacing of 200 to 300 µm. This is in good agreement with a followed emitter width and spacing variation that was carried out on 5×5 cm^2 Al-LARE solar cells. The emitter width and spacing resulted in the conclusion that the highest values are obtained for a minimum of 100 µm emitter width and an emitter spacing of 300 - 400 µm (depending on the emitter width).
Large-area Al-LARE solar cells featuring an emitter width of 100 µm and an emitter spacing of 300 µm were further fabricated and analysed. The best performing Al-LARE solar cell that was passivated by SiO_2/SiNA-SiN_x, reached an efficiency of 17 %. Furthermore, a maximum short-circuit current density gain of 0.45 mA/cm^2 compared to jointly fabricated PhosTop solar cells was found for a Al-LARE solar cell passivated by a Al_2O_3/SiNA-SiN_x on the rear side. This solar cell concept was found to be basically limited by extremely high values of j_{02} in combination with an in some cases slightly increased series resistance due to contact formation problems at the rear side. Furthermore, the passivation quality of the Al_2O_3/SiNA-SiN_x passivated rear was the only passivation able to compensate diffusion losses to the emitter and hence to sustain a comparable IQE plateau to the PhosTop solar cell.

Finally, FALCON solar cells were fabricated that feature an etched back 2 µm deep, screen-printed full area aluminium alloyed passivated emitter. Two different process sequences were carried out, allowing the rear side of one experiment to be passivated by a SiO_2/SiNA-SiN_x stack. An overall short-circuit current density gain, similar to the Al-LARE solar cells, of 0.5 mA/cm^2 was found for the best performing SiO_2/SiNA-SiN_x FALCON solar cell. This is only half of the short-circuit current density gain that was expected from the simulation. This is probably caused by a discrepancy of the assumed reflection difference between the unpassivated and passivated rear side for the simulation and the difference for real solar cells. Furthermore, a strong discrepancy of in some cases almost 20 mV was found between the simulated and actually measured V_{oc}. This discrepancy can be attributed to a lower passivation quality and hence the rear SRV in the fabricated experiments compared to the simulation and increased j_{02}.
The best performing FALCON solar cell was achieved by passivating the rear using a SiO_2/SiNA-SiN_x stack that resulted in an efficiency of 18.9 %. Especially for low performing FALCON solar cells, a high reduction in FF and hence in efficiency was found to be due to an increased series resistance reaching approx. 1 Ωcm^2 and in some cases, an extremely high j_{02}. j_{02} in combination with a not improved or even increased j_{01} compared to the non-passivated rear of the PhosTop solar cell, resulted in a moderate to strongly reduced V_{oc}, as well.

The main advantage of the FALCON compared to the Al-LARE solar cell is the full area etched back and passivated emitter that leads to a constant plateau in the IQE in the visible light range and hence allows a higher j_{sc} compared to the decreased plateau of the Al-LARE solar cell. Furthermore, this full area emitter can lead to a much lower j_{02} that is found for FALCON solar cells compared to the Al-LARE solar cells.

In conclusion, since Al-LARE solar cells are mainly limited due to an extremely high j_{02}, this diploma thesis suggests that unless improvements can be made, the increased fabrication effort is not justified, since a maximum obtained efficiency of 17 % is much lower than the 19.4 % of the improved PhosTop solar cell, while the latter is much easier to fabricate.

The FALCON solar cell concept has a higher potential, since it is mainly limited due to process parameters such as unfilled line contacts on the rear that result in an increased series resistance. Furthermore, the passivation on the etched-back emitter needs to be further increased. For an industrial implementation of this solar cell concept the needed processing steps for fabrication have to be reduced.

Bibliography

[1] R. Alley, T. Berntsen et al. IPCC - Klimaänderung 2007: Wissenschaftliche Grundlagen - Zusammenfassung für politische Entscheidungsträger, 2007.

[2] M. Berger, M. Fischer et al. International Technology Roadmap for Photovoltaics (ITRPV) Results 2011, 2012.

[3] REN21 Renewables Global Status Report 2012 pp. 172, 2012.

[4] H. Fischer and W. Pschunder. Investigation of Photon and Thermal Induced Changes in Silicon Solar Cells. *Proc. 10th Photovoltaic Specialists Conference*, pp. 404–411, 1973.

[5] K. Bothe, R. Sinton et al. Fundamental Boron-Oxygen-Related Carrier Lifetime Limit in Mono- and Multicrystalline Silicon. *Prog. Photovolt.: Res. Appl.*, 13(4):287–296, 2005.

[6] J. Schmidt and K. Bothe. Structure and Transformation of the Metastable Boron- and Oxygen-Related Defect Center in Crystalline Silicon. *Phys. Rev. B*, 69(2):1–8, 2004.

[7] D. Macdonald and L. J. Geerligs. Recombination Activity of Interstitial Iron and Other Transition Metal Point Defects in p- and n-Type Crystalline Silicon. *Appl. Phys. Lett.*, 85(18):4061, 2004.

[8] F. Book, T. Wiedenmann et al. Large Area n-Type Silicon Solar Cells with Selective Front Surface Field and Screen Printed Aluminium-Alloyed Rear Emitter. *Proc. 25th EU PVSEC*, pp. 1465–1468, 2010.

[9] F. Book, T. Wiedenmann et al. Influence of the Front Surface Passivation Quality on Large Area n-Type Silicon Solar Cells with Al-Alloyed Rear Emitter. *Energy Procedia*, 8:487–492, 2011.

[10] A. McEvoy, T. Markvart and L. Castaner. Practical Handbook of Photovoltaics: Fundamentals and Applications. Academic Press, 2011.

[11] M. Green. Silicon Solar Cells - Advanced Principles & Practice. Sydney, NSW, 1995.

[12] P. Würfel. Physics of Solar Cells - From Principles to New Concepts. Wiley-VCH, 2005.

[13] M. Green. Solar Cells - Operating Principles, Technology and System Applications. The University of New South Wales, 1998.

[14] H. Schlangenotto and H. Maeder. Temperature Dependence of the Radiative Recombination Coefficient in Silicon. *Physica Status Solidi (a)*, 21:357–367, 1974.

[15] A. Aberle. Crystalline Silicon Solar Cells - Advanced Surface Passivation and Analysis. University of New South Wales, 1999.

[16] M. J. Kerr and A. Cuevas. Very Low Bulk and Surface Recombination in Oxidized Silicon Wafers. *Semicond. Sci. Technol.*, 17(1):35–38, 2001.

[17] A. Aberle. Surface Passivation of Crystalline Silicon Solar Cells: A Review. *Prog. Photovolt: Res Appl.*, 8(8):473–487, 2000.

[18] M. Hofmann. Rear Surface Conditioning and Passivation for Locally Contacted Crystalline Silicon Solar Cells. PhD thesis, University of Konstanz, 2008.

[19] H. Haverkamp. Kristalline Silizium-Solarzellen mit selektiver Emitterstruktur: Entwicklung, Implementierung und Potential einer zukunftsweisenden Technologie. PhD thesis, University of Konstanz, 2009.

[20] F. Huster. Aluminium-Back Surface Field: Bow Investigation and Elimination. *Proc. 20th EU PVSEC*, pp. 635–638, 2005.

[21] J. Tool, A. R. Burgers et al. Effect of Wafer Thickness on the Performance of mc-Si Solar Cells. *Proc. 17th EU PVSEC*, number October, pp. 1551–1554, 2001.

[22] S. W. Glunz, D. Biro et al. Field-Effect Passivation of the SiO_2-Si Interface. *J. Appl. Phys.*, 86(1):683, 1999.

[23] J. Isenberg, A.v.d. Heide et al. Range of Loss Mechanisms Accessible by Illuminated Lock-In Theromgraphy (ILIT). *Proc. 20th EU PVSEC*, pp. 136–139, 2005.

[24] S. W. Glunz. High-Efficiency Crystalline Silicon Solar Cells. *Advances in OptoElectronics*, 2007:1–15, 2007.

[25] F. Huster. Investigation of the Alloying Process of Screen Printed Aluminium Pastes for the BSF Formation on Silicon Solar Cells. *Proc. 20th EU PVSEC*, number June, pp. 1466–1469, 2005.

[26] D. Kray and S. Glunz Theory and Experiments on the Back Side Reflectance of Silicon Wafer Solar Cells. *Prog. Photovolt: Res. Appl.*, 16(2007):1–15, 2008.

[27] R. Girisch. Determination of Si-SiO_2 Interface Recombination Parameters Using a Gate-Controlled Point-Junction Diode Under Illumination. *IEEE Transactions on Electron Devices*, 35, pp. 203–222, 1988.

[28] A. S. Grove. Surface Effects on P-N Junctions: Characteritics of Surface Space-Charge Regions Under Non-Equilibrium Conditions. *Solid-State Electronics*, 9:783–806, 1966.

[29] J. Fitzgerald and A. S. Grove. Surface Recombination in Semiconductors. *Surface Science*, 9:347–369, 1968.

[30] S. Mahajan. Principles of Growth and Processing of Semicoductors. WCB/McGraw-Hill, 1999.

[31] H. Nagel, A. Aberle et al. Optimised Antireflection Coatings for Planar Silicon Solar Cells using Remote PECVD Silicon Nitride and Porous Silicon Dioxide. *Prog. Photovolt: Res Appl.*, 7:245–260, 1999.

[32] A. Aberle. Overview on SiN_x Surface Passivation of Crystalline Silicon Solar Cells. *Solar Energy Materials & Solar Cells*, 65:239–248, 2001.

[33] B. Hoex, J. J. H. Gielis et al. On the c-Si Surface Passivation Mechanism by the Negative-Charge-Dielectric Al_2O_3. *J. Appl. Phys.*, 104(11):113703, 2008.

[34] J. L. van Hemmen, S. Heil et al. Plasma and Thermal ALD of Al_2O_3 in a Commercial 200 mm ALD Reactor. *Journal of The Electrochemical Society*, 154(7):165–169, 2007.

[35] R. F. Klie, N. D. Browning et al. Analysis of Ultrathin SiO_2 Interface Layers in Chemical Vapor Deposition of Al_2O_3 on Si by in Situ Scanning Transmission Electron Microscopy. *Appl. Phys. Lett.*, 83(6):1187, 2003.

[36] J. L. Murray and A. J. McAlister. The AI-Si (Aluminum-Silicon) System. *Bulletin Of Alloy Phase Diagrams*, 5(1):74–84, 1984.

[37] K. C. Fong, K. Mcintosh et al. Accurate Series Resistance Measurement of Solar Cells. *Prog. Photovolt: Res. Appl.*, 2011.

[38] M. Wolf and H. Rauschenbach. Series Resistance Effects on Solar Cell Measurements. *Advanced Energy Conversion*, 3:455–479, 1963.

[39] J. Schmidt and M. Kerr. Highest-Quality Surface Passivation of Low-Resistivity p-Type Silicon Using Stoichiometric PECVD Silicon Nitride. *Solar Energy Materials & Solar Cells*, 65:585–591, 2001.

[40] B. Fischer. Loss Analysis of Crystalline Silicon Solar Cells Using Photoconductance and Quantum Efficiency Measurements. PhD thesis, University of Konstanz, 2003.

[41] R. Sinton and A. Cuevas. Contactless Determination of Current–Voltage Characteristics and Minority-Carrier Lifetimes in Semiconductors from Quasi-Steady-State Photoconductance Data. *Appl. Phys. Lett.*, 69(17):2510, 1996.

[42] H. Nagel, C. Berge et al. Generalized Analysis of Quasi-Steady-State and Quasi-Transient Measurements of Carrier Lifetimes in Semiconductors. *J. Appl. Phys.*, 86(11):6218, 1999.

[43] A. Cuevas. The Effect of Emitter Recombination on the Effective Lifetime of Silicon Wafers. *Solar Energy Materials and Solar Cells*, 57:277–290, 1999.

[44] M. J. Kerr. Surface, Emitter and Bulk Recombination in Silicon and Development of Silicon Nitride Passivated Solar Cells. PhD thesis, Australian National University, 2002.

[45] D. Kane and R. Swanson. Measurement of the Emitter Saturation Current by a Contactless Photoconductivity Decay Method. *Proc. 18^{th} IEEE PVSC*, pp. 578–583. IEEE, New York, 1985.

[46] R. A. Sinton and A. Cuevas. Quasi-Steady-State Photoconductance, a New Method for Solar Cell Material and Device Characterization. *Proc. 25^{th} IEEE PVSC*, pp. 457–460, 1996.

[47] T. Fuyuki, H. Kondo et al. Photographic Surveying of Minority Carrier Diffusion Length in Polycrystalline Silicon Solar Cells by Electroluminescence. *Appl. Phys. Lett.*, 86(26):3, 2005.

[48] B. Steuer. Aufbau eines Photolumineszenz- Messplatzes zur Charakterisierung von Wafern und Solarzellen aus kristallinem Silizium. Diploma thesis, University of Konstanz, 2011.

[49] J. Giesecke. Messung von Minoritätsladungsträger-Diffusionslängen in Silicium-Solarzellen mit Lumineszenzmethoden. Diploma thesis, University of Konstanz, 2009.

[50] O. Breitenstein, A. Khanna et al. Quantitative Evaluation of Electroluminescence Images of Solar Cells. *Phys. Status Solidi (RRL)*, 4(1-2):7–9, 2010.

[51] WEP Ingenieurbüro. *ECV Manual CVP 21.* 2010.

[52] S. Gloger. Verbesserte Rückseitenpassivierung von siebgedruckten bifacialen Solarzellen. Diploma thesis, University of Konstanz, 2009.

[53] F. Huster and G. Schubert. ECV Doping Profile Measurements of Aluminium Alloyed Back Surface Fields. *Proc. 20th EU PVSEC*, pp. 1462–1465, 2005.

[54] D. L. Meier, H. P. Davis et al. Aluminum Alloy Back p-n Junction Dendritic Web Silicon Solar Cell. *Solar Energy Materials*, 65:621–627, 2001.

[55] X. Xi, W. Wu et al. 19.8 % Efficiency on Large Area N-type Czochralski Silicon Solar Cells with Aluminium Rear Emitter. *38th IEEE PVSC*, Preprint, 2012.

[56] T. Wiedenmann. Untersuchungen zur Vorderseiten-Passivierung und Bildung des rückseitigen Al-Emitters für kristalline n-Typ Si-Solarzellen. Diploma thesis, University of Konstanz, 2011.

[57] K. A. Reinhardt and W. Kern. Handbook of Silicon Wafer Cleaning Technology. William Andrew, 2007.

[58] T. Lauermann, A. Zuschlag et al. The Influence of Contact Geometry and Sub-Contact Passivation of the Performance of Screen-Printed Al_2O_3 Passivated Solar Cells. *Proc. 26th EU PVSEC*, pp. 1137–1143, 2011.

[59] E. Urrejola, K. Peter et al. Distribution of Silicon in the Aluminum Matrix for Rear Passivated Solar Cells. *Energy Procedia*, 8:331–336, 2011.

[60] K. R. Mcintosh. Lumps, Humps and Bumps: Three Detrimental Effects in the Current-Voltage Curve of Silicon Solar Cells. PhD thesis, University of New South Wales, 2001.

[61] D. A. Clugston and P. A. Basore. PC1D Version 5: 32-Bit Solar Cell Modeling on Personal Computers. *Proc. 26th IEEE Photovoltaic Specialists Conference*, pp. 4–7, 1997.

[62] P. A. Basore and K. Cabanas-Holmen. PC2D: A Circular-Reference Spreadsheet Solar Cell Device Simulator. *IEEE Journal of Photovoltaics*, 1:72–77, 2011.

[63] M. Rüdiger, M. Rauer et al. Accurate Modeling of Aluminum-Doped Silicon. *Energy Procedia*, 8:527–532, 2011.

[64] J. Schmidt, N. Thiemann et al. Recombination Lifetimes in Highly Aluminum-Doped Silicon. *J. Appl. Phys.*, 106(9):093707, 2009.

[65] K. Pollock, J. Junge et al. Detailed Investigation of Surface Passivation Methods for Lifetime Measurements on p-Type Silicon Wafers. *IEEE Journal of Photovoltaics*, 2(1), pp. 1–6, 2012.

[66] B. Chhabra, S. Bowden et al. High Effective Minority Carrier Lifetime on Silicon Substrates Using Quinhydrone-Methanol Passivation. *Appl. Phys. Lett.*, 96(6):063502, 2010.

[67] A. Cuevas and P. A. Basore. Surface Recombination Velocity of Highly Doped n-Type Silicon. *J. Appl. Phys.*, 80(6):33700 – 03375, 1996.

[68] W. Soppe, H. Rieffe et al. Bulk and Surface Passivation of Silicon Solar Cells Accomplished by Silicon Nitride Deposited on Industrial Scale by Microwave PECVD. *Prog. Photovolt: Res. Appl.*, 13(7):551–569, 2005.

[69] T. Lüder, T. Lauermann et al. Al_2O_3/SiN_x- Stacks at Increased Temperatures: Avoiding Blistering During Contact Firing. *2nd SiliconPV*, Preprint, 2012.

[70] B. Hoex, J. Schmidt et al. Excellent Passivation of Highly Doped p-Type Si Surfaces by the Negative-Charge-Dielectric Al_2O_3. *Appl. Phys. Lett.*, 91(11):112107, 2007.

[71] P. Altermatt, H. Plagwitz et al. The Surface Recombination Velocity at Boron-Doped Emitters: Comparison Between Various Passivation Techniques. pp. 647–650, 2006.

[72] R. Bock. Screen-Printed Aluminium-Doped p^+ Emitters for the Application to n-Type Silicon Solar Cells. PhD thesis, University of Hannover, 2011.

[73] S. Öner. Charakterisierung von kristallographischen Defekten in kontaminiertem multikristallinem Silizium. Diploma Thesis, University of Konstanz, 2012.

[74] O. Breitenstein and J. Rakotoniaina. Lock-In Thermography - A Universal Tool for Local Analysis of Solar Cells. *Proc. 20th EU PVSC*, pp.590–593, 2005.

[75] R. Bock, J. Schmidt et al. The ALU^+ Concept: n-Type Silicon Solar Cells with Surface-Passivated Screen-Printed Aluminum-Alloyed Rear Emitter. pp. 30–35, 2009.

[76] D. K. Schroder. Semiconductor Material And Device Characterization. Wiley Interscience, 3rd Edition, 2006.

[77] R. Bock, P. Altermatt et al. Formation of Aluminum–Oxygen Complexes in Highly Aluminum-Doped Silicon. *Semiconductor Science and Technology*, 25(10):105007, 2010.

Acknowledgement

Finally, I want to express my appreciation for the great support and friendly ambiance within the photovoltaic division. In person, I would like to thank

- Prof. Dr. Giso Hahn for the kind welcome in the photovoltaic divison, the extensive support and acceptance of the first correction.
- Prof. Dr. Thomas Dekorsy for the acceptance of the secondary correction and advice during my studies.
- Felix Book for the intensive and patient support, interesting and enriching discussions as well as the friendly cooperation. Furthermore, I want to give thanks for the attentive proofreading of this thesis.
- Thomas Wiedenmann for the assisting activities and his entertaining nature as well as for his preparatory thesis on PhosTop solar cells.
- Alexander Frey, Susanne Fritz, Leonard Kraus and Joachim Ranzmeyer for the nice atmosphere in our office and stimulating discussions.
- Greg Greenman and Pratik Kala for attentively proofreading this thesis.
- Axel Herguth, David Kiliani, Thomas Lüder and Lisa Mahlstaedt for intensive support and advice
- and finally by the rest of the photovoltaic division, who supported me and contributed to the nice atmosphere.

I want to conclude with giving my family and friends my deepest appreciation for their strong support and help during my studies.

Appendix

A. PC1D Simulation of the Base Doping Influence

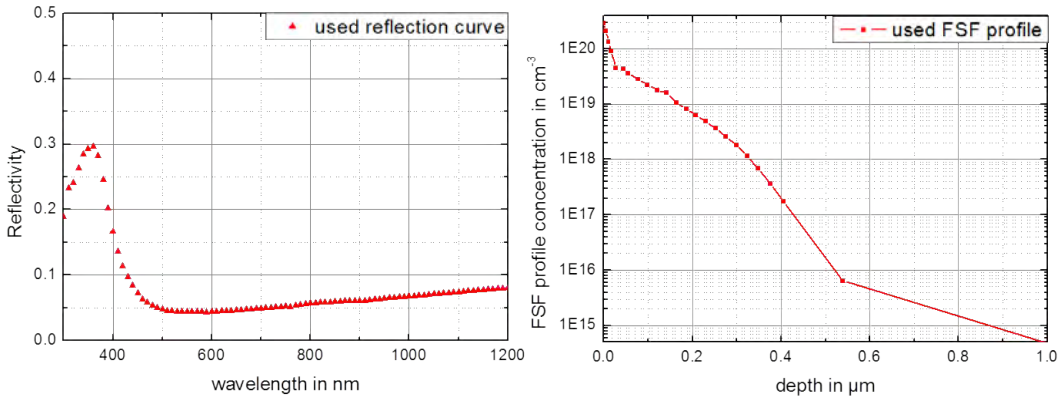

Figure 1.: Left: Imported front reflection profile measured for an earlier fabricated PhosTop solar cell; Right: Imported FSF profile

Table 1.: Used PC1D parameter for the simulation of the background doping influence on a PhosTop cell performance

Symbol	**Name**	**Value**
N_D	Background doping	4.5×10^{14} cm^{-3}
R_{bulk}	Bulk resistance	10 Ωcm
R_{FSF}	FSF profile	imported, see figure 1
$R_{emitter}$	Emitter sheet resistance	11 Ω/sq
	Emitter depth	5 µm
τ_{bulk}	Bulk lifetime	10 ms
D_p	Diffusivity constant for holes	12 cm^2/s
D_n	Diffusivity constant for electrons	35.6 cm^2/s
n_i	Intrinsic carrier concentration at 300 K	$10^{10}cm^{-3}$
	Surface textured - pyramid height	7 µm
A	Area	1 cm^2
W	Width	170 µm
	Internal diode	2×10^{-8} A
	Internal conductor	2×10^{-4} S
	Emitter contact	0.3 Ω
	Base contact	1×10^{-5} Ω
	Front reflectivity	imported profile, see figure 1
S_{front}	Front surface recombination velocity	19000 cm/s
S_{rear}	Rear surface recombination velocity	19000 cm/s

B. PC2D Simulation Parameters for Emitter Spacing in Section 4.2.2

Table 2.: Parameter used for the simulation of the emitter pitch in section 4.2.2

Symbol	Name	Value
N_D	Bulk doping	10^{15} cm^{-3}
$R_{sheet,Finger}$	s-FSF sheet resistance underneath the contact	35 Ω/sq
$R_{sheet,pass}$	s-FSF sheet resistance at the passivated region	100 Ω/sq
$R_{sheet,emitter}$	Emitter sheet resistance	11 Ω/sq
τ_{bulk}	Bulk lifetime	10 ms
	emitter depth	5 µm
D_p	Diffusivity constant for holes	12 cm^2/s
D_n	Diffusivity constant for electrons	35 cm^2/s
n_i	Intrinsic carrier concentration at 300 K	8.56×10^{9} cm^{-3}
A	Area	1 cm ^{2}
W	Width	170 µm
R_s	Additional R_s	0.4 Ωs
G_{sh}	Additional G_{sh}	0.0002 S
$T_{F,trans}$	Total front surface transmission	98 %
$T_{Haze,trans}$	Front surface haze transmission	80 %
$R_{Internal,spec\ ref}$	Front internal specular reflectance	10 %
$R_{Internal,diff\ ref}$	Front internal diffuse reflectance	92 %
$R_{rear,spec}$	Rear internal specular reflectance	100 %
$R_{rear,diffuse}$	Rear internal diffuse reflectance	100 %
	Bottom surface haze	50 %
	Rear internal specular reflectance finger	75 %
	Rear internal specular reflectance passivated	95 %
	Rear internal diffuse reflectance finger	70 %
	Rear internal diffuse reflectance passivated	95 %
$j_{01,front,finger}$	Front saturation current density at the front finger	600 fA/cm^2
$j_{01,front,\ aside\ finger}$	Front saturation current density besides of the front finger	200 fA/cm^2
$j_{01,front,pass}$	Front saturation current density at the front passivation	50 fA/cm^2
$j_{01,rear,finger}$	Rear saturation current density at the emitter finger	220 fA/cm^2
$j_{01,rear,pass}$	Rear saturation current density between the emitter finger	varied
$j_{02,front,finger}$	Front finger	0
$j_{02,front,pass}$	Front passivation	0
$j_{02,rear,finger}$	Rear finger	2.4×10^{-08} A/cm^2
$j_{02,rear,pass}$	Rear passivation	0

C. PC2D Simulation Parameters for Contact Spacing in Section 4.3.1

Table 3.: Parameter used for the simulation of the contact pitch in 4.3.1

Symbol	Name	Value
N_D	Background doping	10^{15} cm^{-3}
$R_{sheet,base}$	base resistance	4.5 Ω cm
$R_{sheet,Finger}$	s-FSF underneath the contact	35 Ω/sq
$R_{sheet,pass}$	s-FSF at the passivated region	100 Ω/sq
$R_{sheet,emitter}$	Emitter doping on the surface	50 Ω/sq
	emitter depth	2 µm
τ_{bulk}	Bulk lifetime	10 ms
D_p	Diffusivity constant for holes	12 cm^2/s
D_n	Diffusivity constant for electrons	35 cm^2/s
n_i	Intrinsic carrier concentration at 300 K	8.56×10^{9} cm^{-3}
A	Area	1 cm ^{2}
W	Width	170 µm
R_s	Additional R_s	0.4 Ωs
G_{sh}	Additional G_{sh}	0.0002 S
$T_{F,trans}$	Total front surface transmission	98 %
$T_{Haze,trans}$	Front surface haze transmission	80 %
$R_{Internal,specRef}$	Front internal specular reflectance	10 %
$R_{Internal,Diff\ Ref}$	Front internal diffuse reflectance	92 %
$R_{R,spec}$	Rear internal specular reflectance	100 %
$R_{R,diffuse}$	Rear internal diffuse reflectance	100 %
	Bottom surface haze	50 %
	Rear internal specular reflectance finger	75 %
	Rear internal specular reflectance passivated	95 %
	Rear internal diffuse reflectance finger	70 %
	Rear internal diffuse reflectance passivated	95 %
$j_{01,front,finger}$	Front saturation current density at the front finger	600 fA/cm^2
$j_{01,front,\ aside\ finger}$	Front saturation current density besides of the front finger	200 fA/cm^2
$j_{01,front,pass}$	Front saturation current density at the front passivation	50 fA/cm^2
$j_{01,rear,finger}$	Rear saturation current density at the emitter finger	220 fA/cm^2
$j_{01,rear,pass}$	Rear saturation current density between the emitter finger	varied
$j_{02,front,finger}$	Front finger	0
$j_{02,front,pass}$	Front passivation	0
$j_{02,rear,finger}$	Rear finger	2×10^{-08} A/cm^2
$j_{02,rear,pass}$	Rear passivation	0

D. PC1D Simulation of the Emitter Etch Back in Section 4.3.2

Table 4.: Parameter used for the simulated influence of the etch back as a function of the surface velocity

Symbol	Name	Value
N_D	Background doping	4.5×10^{14} cm^{-3}
R_{bulk}	base resistance	10 Ωcm
R_D	FSF profile	imported, see figure 1
$R_{emitter}$	Emitter sheet resistance on the surface	varies
	Emitter depth	varied
τ_{bulk}	Bulk lifetime	10 ms
D_p	Diffusivity constant for holes	12 cm^2/s
D_n	Diffusivity constant for electrons	35 cm^2/s
n_i	Intrinsic carrier concentration at 300 K	1×10^{10} cm^{-3}
A	Area	1 cm^2
W	Width	170 µm
	Surface textured - pyramid height	7 µm
	Internal diode	2×10^{-8} A
	Internal conductor	2×10^{-4} S
	Emitter contact	0.3 Ω
	Base contact	1×10^{-5} Ω
	Front reflectivity	imported profile, see figure 1
S_{front}	Front surface recombination velocity	19000 cm/s
S_{rear}	Rear surface recombination velocity	varied